Fabrication of Non-Spherical Biodegradable Particles for Drug Delivery Applications and Studying the Impact of Shape on the Efficacy of Particulate Carriers

by

Hanieh Safari

A dissertation submitted in partial fulfillment
of the requirements for the degree of
Doctor of Philosophy
(Chemical Engineering)
in the University of Michigan
2020

Doctoral Committee:

    Professor Omolola Eniola-Adefeso, Chair
    Professor Ronald Larson
    Associate Professor Sunitha Nagrath
    Associate Professor Anish Tuteja

Hanieh Safari

safariha@umich.edu

ORCID iD: 0000-0001-9760-561X

DEDICATION

To mom, dad, and my little sister for all their love and support in this journey and during my entire life; I will be forever grateful.

ACKNOWLEDGEMENTS

First, I want to thank my Adviser, Professor Omolola Eniola-Adefeso, for all her support and mentorship during these years of my graduate career. I am eternally thankful to Lola for giving me the opportunity to work in her lab and guiding me on this journey. Since joining Lola's lab, I learned how to do science and think independently. Lola gave me the chance to explore my ideas and work in different areas, which I will be forever grateful for. I will always be thankful to Lola and will be looking forward to seeing great research from her lab.

Second, I want to express my gratitude to Professor Ronald Larson, Professor Sunitha Nagrath, and Professor Anish Tuteja for serving on my defense committee and for their insights on my work.

Thank you to all the current and former members of Eniola Lab for their help and support. Special thanks to our former lab members Professor Catherine Fromen, Margaret Fish, Daniel Sobczynski, and Alex Thompson, for their guidance during my first few years as a graduate student. Thanks to all our current lab members, Billy Kelley, Genesis Lopez, Mario Gutierrez, Alison Banka, Violet Sheffey, Jonathan Lee, Emma Brannon, Nicholas Kaczorowski, Rue Felder, Valentina Guevara, and Logan Piegols for being amazing friends and coworkers. It was a pleasure to work with you all in the last five years.

I want to thank our collaborators Professor Michael Holinstat, Dr. Reheman Adili, Professor Lonnie Shea, and Dr. Eiji Saito for their help.

Thanks to all my great friends in Ann Arbor, who helped me create so many unforgettable memories in this city. It would have been impossible for me to spend these five years far from home and family without you all. I want to specially thank my incredible friends Elham Adib, Negin Akram, and Valentina Igenegbai, who have been like sisters to me during the last five years. I would not have been able to go through this journey without having you girls in my life.

And last and foremost, I want to thank my family for their love and support throughout my life. Thanks to my mom and dad for dedicating their life to my success since the day I was born. I will never be able to thank you enough for all you have done for me. Thanks to my sister, Faezeh, for being the joy of my life since the day she was born. You all mean the world to me.

TABLE OF CONTENTS

LIST OF FIGURES

ix

LIST OF TABLES

LIST OF ABBREVIATIONS

ACD   Acetate Citrate Dextrose

API   Active Pharmaceutical Ingredient

AR   Aspect Ratio

BSA   Bovine Serum Albumin

Ca   Capillary Number

DCM   Dichloromethane

DLS   Dynamic Light Scattering

EAE   Experimental Autoimmune Encephalomyelitis

EDAC   N-(3-Dimethylaminopropyl)-N`-ethylcarbodiimide Hydrochloride

EDS   Energy-dispersive Spectroscopy

ESE   Emulsion Solvent Evaporation

ESD   Equivalent Spherical Diameter

FITC   Fluorescein

GFM   Glomerular Filtration Membrane

GM-CSF   Granulocyte Colony-stimulating Factor

HPLC   High Performance Liquid Chromatography

HUVEC   Human Umbilical Vein Endothelial Cells

IgG   Immunoglobulin G

IgM   Immunoglobulin M

MNP	Mononuclear Phagocyte
MPS	Mononuclear Phagocyte System
NaMP	Sodium Metaphosphate
NaTP	Sodium Tripolyphosphate
NMR	Nuclear Magnetic Resonance
PBS	Phosphate Buffered Saline
PEG	Poly(ethylene glycol)
PLGA	Poly(lactic-co-glycolic) acid
PMN	Polymorphonuclear Leukocyte
PVA	Polyvinyl Alcohol
RBC	Red Blood Cell
RES	Reticuloendothelial System
RPM	Revolutions Per Minute
SEM	Scanning Electron Microscopy
WSR	Wall Shear Rate
XPS	X-ray Photoelectron Spectroscopy

ABSTRACT

Biodegradable particles are used to specifically deliver drugs to diseased sites to increase their efficacy and minimize their side effects. Until now, most of the drug delivery platforms have been spherical in their shape due to the ease of fabrication and their well-characterized performance. Recent studies have been shown that shape modifications can be utilized to modulate the performance of particulate carriers to increase their efficacy via changing their immune clearance rate, their circulation time, and their margination and binding to the vascular wall. However, there are still considerable knowledge gaps to understand the impact of the shape of the efficacy of micro/nanoparticles.

One of the reasons for the lack of a clear understanding of the impact of shape on the efficacy of biodegradable particles is the absence of a simple and scalable method to fabricate non-spherical particles in large scales. In this thesis, we have developed novel emulsion-based techniques to fabricate non-spherical biodegradable particles in large scales. We first developed a modified two-step emulsion solvent evaporation technique to fabricate ellipsoidal poly(lactic-co-glycolic acid), PLGA, rods. Emulsion droplets were elongated via the application of shear in a system with low interfacial tension. Via this method, we could successfully fabricate PLGA rods with a major axis size as small as 3 micrometers, which is the size range of interest in vascular targeting applications. Our results showed that separation of the droplet formation and stretching steps, and a careful choice of the oil phase solvent and surface-active molecule are the key factors to fabricate rods in the smaller size ranges. We also were able to show these rods were able to

successfully bind to an inflamed vasculature both *in vitro* and *in vivo*. When the phagocytosis of the particles of various shapes by different phagocyte sub-types was investigated, we showed that contrary to the mononuclear phagocytes, i.e., macrophages and monocytes, neutrophils would preferentially get associated with rod-shaped particles *in vitro* and *in vivo*. This opens up the opportunity to selectively target neutrophils in acute inflammation. We next we were able to innovate a metal-assisted gold templating emulsion-based method to fabricate bile salt particles. The composition of these particles and the presence of bile salts as the primary component in their structure were confirmed via different chemical characterization techniques. We also showed that these particles would degrade via surface erosion and release bile salts to the solution. This makes these composite particles suitable candidates as controlled release systems in disease models where the therapeutic benefit of the bile salts is proved to minimize side effects. We demonstrated that these particles could successfully lyse adipocytes and induce apoptosis in cancer cells.

Last, we explored the modification of emulsion-based methods via the utilization of a cosolvent to increase the loading efficiency of hydrophilic agents in polymeric nanoparticles. We showed that the utilization of a minimal amount of a polar cosolvent with minimum hydrophilicity, such as ethyl acetate, could be used to stabilize antibodies in the emulsion oil phase and increase their loading efficiency. The methods introduced in this study enable the fabrication of novel drug carriers on a large scale for clinical applications. Overall, the results of this study open up an opportunity for developing new methods for the fabrication of novel biodegradable drug delivery platforms that can be used in the treatment of various disorders.

CHAPTER 1: Introduction

1.1. Publication Information

The text of this chapter is in part from the publication: **Safari, H.**, Lee, J. K. H, Eniola-Adefeso, O. Effect of Shape, Rigidity, Size, and Flow on Targeting. *Nanoparticles for Biomedical Applications. Elsevier*. 2020: 55-66.[1] Prior permission from the Elsevier is obtained for using the borrowed text.

1.2. Background and Significance

Within the last few decades, biodegradable particles have gained attention for their utilization in various applications, including drug and vaccine delivery, tissue engineering, cosmetic industry, and environmental and agricultural applications.[2–11] Usage of biodegradable particles for drug delivery applications allows for specific, local delivery of an active pharmaceutical ingredient (API) to a diseased tissue with the primary goal of increasing drug efficacy while minimizing systemic side effects.[12] Biodegradable polymers break up to non-toxic byproducts via hydrolysis or regular metabolic pathways in the body, and this makes them suitable candidates for usage in clinical application.[13] These biodegradable systems have the potential to enhance treatment status of various disorders, including but not limited to cardiovascular diseases, cancer, and autoimmune diseases.[11,14–16]

Various biodegradable systems have been used as carriers in drug delivery applications, including lipid particles and liposomes, micelles, viral particles, antibody-drug conjugates,

dendrimers, and solid matrix particles.[17–20] Despite the advantages and drawbacks of each of these carriers systems, the interest in using solid-matrix particles has outpaced the others.[16] These particles benefit from the flexibility in tailoring their physical design properties, i.e., size, shape, hydrophobicity, drug loading, and release profile, and they can easily be decorated with various targeting ligands to enable their specific localization in disease sites.[11,21,22] Despite their promise, very few biodegradable solid matrix carrier formulations have made their way into clinics,[21] likely a result of the various interfering factors within the body that limits the efficacy of these carriers. Thus, the design of these carriers needs to be carefully optimized for each specific application in order to maximize their therapeutic efficacy and enable their clinical transformation.

1.3. Physiological Considerations for the Design of Drug Carriers

In general, most of the current carrier systems are spherical in geometry and tend to be in the nanometer size range. A quick search of the literature for "polymeric drug carrier" mostly shows works that describe particles in the 100-500 nm size range (11.2019). Numerous studies have demonstrated that the size and shape of drug carriers affect their efficacy due to the interaction of particles with various physiological factors *in vivo*, including clearance by mononuclear phagocyte system (MPS),[23,24] plasma protein interference,[25,26] and blood shear flow.[22,27–29] Thus, the physical properties of particles need to be optimized when designing them to maximize their functionality for drug delivery applications. In this section, we have discussed different physiological parameters that need to be considered when designing drug delivery systems.

1.3.1. In vivo clearance of the injected particles

Upon being introduced into circulation, drug carriers are subjected to clearance from the bloodstream via reticuloendothelial system (RES), kidneys, and circulating blood leukocytes. The rate of this clearance defines the *in vivo* circulation time of particles in the bloodstream. Depending on the application, an increase or decrease in carrier accumulation in a specific organ and uptake by white blood cells may be desirable, and tailoring particle design parameters can help achieve these goals. Thus, it is crucial to understand how these carrier physical characteristics will affect the performance of particles.

Resident macrophages within the RES organs are a significant contributor to the *in vivo* clearance of particles.[30] Particle design parameters such as size and hydrophobicity will determine both their entrapment within RES organs and their clearance rate by tissue-resident macrophages.[30]

The liver is one of the RES organs that significantly contribute to the *in vivo* clearance of particles. The primary clearance mechanism of particles in the liver is their uptake by the Kupffer cells, which are the liver's resident macrophages within the liver lumen and comprise about 80-90% of the tissue macrophages of the body.[31,32] The recognition and phagocytosis of particles by Kupffer cells are mediated by their cell-surface expressed receptors that identify plasma opsonin proteins adsorbed on the surface of particles.[33] Different studies have demonstrated that increasing the size of nanoparticles will increase their *in vivo* clearance by the liver.[34]

The spleen is another RES organ that plays a major role in the *in vivo* clearance of micro/nanoparticles. In the spleen, filtration is the primary contributor to particle clearance, which is enabled by the specialized structure of its venous system.[35] After being stuck in the red-pulp cords, particles will be removed via phagocytosis by macrophages.[31,35] Particles larger than 200 nm are presumed to be efficiently trapped by spleen filtration.[36] A log-log relationship has been

reported for the uptake of particles by the spleen, where increasing their size increases their splenic clearance.[31]

Kidneys are also one of the organs contributing to the elimination of waste from the body, and thus, the *in vivo* clearance of particulate carriers from the bloodstream.[37] Renal clearance of nanoparticles is carried out by the glomerular filtration membrane (GFM).[37] The kidney's filtration of particles is heavily dependent on their design parameters, including their size and charge.[37] The cut-off limit for glomerular filtration is ~6 nm, and particles larger than this size can easily bypass renal clearance.[37] Different studies have also demonstrated that the renal clearance of particles is profoundly charge and density-dependent, and cationic and lighter particles will be cleared by kidneys more efficiently.[37]

Recent studies have provided evidence that circulating blood leukocytes, i.e., neutrophils and monocytes, also play an essential role in the *in vivo* clearance of the intravenously-injected particles.[38,39] Though significantly understudied compared to the RES system, recent researches show that changing the particle design parameters can either improve or inhibit their clearance by neutrophils and monocytes as well.[40,41]

To summarize, different design parameters will change the phagocytosis rate of particles and their accumulation in various organs, and thus, their *in vivo* circulation time. For each study, particles need to be custom-designed to either escape *in vivo* clearance or have selective accumulation in a specific organ or association with a specific leukocyte sub-type.

1.3.2. *Opsonization and protein corona formation*

Particles rapidly adsorb plasma proteins onto their surface upon coming into contact with blood. This protein adsorption results in the formation of a protein corona around the

4

nano/microparticles, which will modify their physicochemical properties and bioavailability and, ultimately, determine the host immune response.[42,43] The adsorption of opsonin proteins onto the surface of particles will initiate their phagocytosis and clearance from the bloodstream.[44] Additionally, adsorption of the opsonin proteins on the surface of targeted carriers will shield targeting ligands and inhibit their binding to the target site.[45] As a result, the composition and quantity of the adsorbed proteins on the surface of biodegradable particles is a significant contributing factor to their efficacy, and different factors that alter the identity of the protein corona on particulate carriers should be carefully studied when designing them.

1.3.3. *Margination and binding to the vascular wall*

Blood is a multicomponent suspension composed of red blood cells, RBCs, leukocytes, and platelets.[46] In blood flow under physiological conditions, RBCs are depleted from the proximity of the vessel wall forming a cell-free layer near the wall.[46,47] Due to the heterogenous collisions between the RBCs and leukocytes, leukocytes and platelets typically segregate near the vessel wall in a phenomenon called margination.[41,47] Once injected into the bloodstream, the same as the leukocytes, the intravenously-injected particles need to exit the RBC core and localize and bind to the vascular wall in order to reach the target site and deliver their cargo efficiently.[11] As a result, efficient localization to the vascular wall out of the RBC core is another critical parameter that needs to be considered when designing IV-injected drug carriers. Physical design parameters of particles such as their size and shape significantly impact their margination and vascular binding. Different studies have shown that size is the most influential parameter on the binding of particles to the vascular wall.[22] Different *in vitro*, *in vivo*, and theoretical models of blood flow have demonstrated that microparticles have an enhanced margination and binding to the vascular

wall, and 2-5 µm particles are shown to be the optimum size for vascular targeting applications.[22,48–50]

1.3.4. Drug loading and release profile

For drug delivery applications, polymeric particles need to be successfully loaded with a drug and deliver their cargo to the diseased site to have a therapeutic benefit. Once within the target site, particles need to release their loaded cargo. The release of therapeutic loadings from particles is mediated via degradation and swelling of the particle matrix and diffusion of the loaded cargo.[51] In turn, the release kinetics of the loaded drug from particles is a critical factor that can affect their therapeutic efficacy and toxicity – controlled release kinetics typically increase the efficacy of the therapeutic formulation while minimizing their side effects.[51,52] The size and shape of particles and the method used for their fabrication will impact their release kinetics.[53–57] Thus, the design parameters of microparticles need to be optimized to achieve the desired drug release kinetics that delivers maximum therapeutic efficacy with minimal side effects.

1.4. Effect of the Shape on the Efficacy of Particulate Carriers

As mentioned in the previous section, particle design parameters such as their size, shape, surface charge, hydrophobicity, and density will impact their efficacy. Particle shape recently emerged as a critical design parameter that affect the efficacy of particulate drug carriers. In this section, the results of numerous studies on the impact of shape on the performance of particles, including their clearance by leukocytes and RES organs, margination and binding to the vascular wall, protein corona formation, and release profile are summarized.

1.4.1. In vivo clearance and circulation time

The shape of particles is a factor that strongly affects their phagocytosis. Generally, several studies have demonstrated that elongated particles will have reduced uptake by macrophages. Champion et al. reported for the first time that the uptake of particles by alveolar macrophages is dependent on their shape and surface curvature. Macrophages were shown not to internalize particles if contacting particles via their flat, low curvature side.[23] The same group reported that worm-like particles with aspect ratios >20 would escape phagocytosis by rat alveolar macrophages.[58] Another study also confirmed that prolate ellipsoids have lower internalization by macrophages despite having a higher attachment rate to these cells.[59] Computer simulations have also confirmed the trend of the reduced phagocytosis of elongated particles, predicting that elongated particles coming into contact with the lipid bilayer of the cells through their lower curvature side will require longer times for translocation.[60] Unfortunately, the bulk of studies looking into the effect of particle shape on phagocytosis have focused on experimental assays on macrophages in culture media. Thus, the impact of the size and shape of particles on their uptake by other phagocyte cells, including neutrophils, remains unclear.

Particle shape also influences the biodistribution of the carriers in different organs. For example, the use of high aspect ratio particles can help particulate carriers to avoid clearance by the spleen.[36] In this approach, elongated particles with major axis sizes as high as 18 μm can avoid the spleen filtration if their minor axis dimension is kept below the spleen pore size.[61] As discussed above, if the dimensions of particles are below the kidney filtration limit of 6 nm, they will go through renal clearance. Thus, utilizing non-spherical particles, which have one dimension of larger than the 6 nm cutoff limit, can help to avoid the renal clearance of the smaller carriers.[61] As a result of the lower uptake of the high aspect ratio particles by macrophages, increasing their

7

aspect ratio helps decrease their accumulation in the liver as well.[61] In general, we can conclude from different studies that increasing the aspect ratio of carriers can be a helpful strategy for lowering their uptake by different RES organs.

Due to the influence of the particle shape on their phagocytosis rate and accumulation in different organs, the circulation time of particulate carriers in the blood is also a function of shape. Different studies have reported longer circulation time of the high aspect ratio particles, including nanorods and filomicelles, which can be concluded that it is due to their lower entrapment in and uptake by RES organs and macrophages, respectively.[36,61,62]

In summary, particle shape significantly affects the circulation time and the tissue/organ accumulation of particulate carriers. Thus, the drug carriers should be custom-designed to either increase or decrease their circulation time or target them to a specific organ of interest.

1.4.2. Protein corona profile

The quantity and quality of the proteins adsorbed onto a particle surface is a function of their surface curvature and thus is dependent on their size and shape.[63,64] In this section, we focus on explaining the influence of the shape of particulate carriers on their protein profile. Particle shape has been reported to alter the plasma protein corona formation on nanoparticles. For titanium dioxide (TiO_2) nanoparticles, the composition of the corona is dependent on their shape. Immunoglobulin M (IgM) and immunoglobulin G (IgG) were among the major bound proteins on nanorods, whereas fibrinogen was the primary protein existing in the corona of the nanotubes.[65] Mesoporous silica nanorods and nanospheres have also been investigated to observe the effect of morphology on the adsorption of albumin, γ-globulin, and fibrinogen proteins on these nanoparticles.[66] This study reported that decreasing the surface curvature of particles will reduce

the initial adsorption rate of the proteins onto their surface. However, this trend is reversed for the proteins that have a rod shape conformation, such as fibrinogen.[66] When *in vivo* protein corona of gold nanorods and nanostars was studied after circulation in rodents, the total amount of the adsorbed proteins was more significant for nanostars because of their larger surface area.[67] The total number of proteins is a result of the interplay between both the size and the shape of the particles.[67]

In summary, the shape of particles is a major contributing factor to the protein corona formed around micro/nanoparticles. Generally, increasing the available surface area and surface curvature of particles increases the total amount of the adsorbed proteins on the particle surface. However, the composition of the adsorbed proteins, as well as the extent and rate of the protein adsorption is a result of the interplay between the size, shape, material composition, the surface charge, and the conformation of the protein of interest and should be studied for different carriers independently.

1.4.3. Drug release kinetics

The release profile of the loaded drug from particles is an important factor that can affect the drug carrier efficacy. Numerous studies have suggested that the release kinetics of particulate carriers is depended on their surface area to volume ratio. When we have a diffusion-controlled release, which is the dominant mechanism in the initial burst release phase, increasing the surface area to volume ratio of particles has been shown to increase the drug release rate in different studies.[53] This can be attributed to the resultant increased swelling rate of particles leading to a higher diffusion rate of the drug.[53–56] A few studies have looked at the effect of particle shape on the drug release from polymeric particles. For a fixed total drug loading and size, the elongated

shapes with a larger surface area to volume ratio will demonstrate the fastest release.[57] However, further investigations are required to fully understand how modifying the shape of particles will change their release profile.

1.4.4. *Margination and vascular binding*

Different theoretical and experimental studies have shown that vascular binding of the particles dependent on their shape. This dependence on the shape is discussed further in this section. Particle shape is a significant contributor to the adhesion trend of particulate carriers. Simulation studies modeling blood flow have shown that despite having similar or lower margination, ellipsoidal particles will have improved adhesion to the vascular wall due to their slower rotational dynamics near the wall,[49,68] which has also been confirmed in different experimental studies. *In vitro* experiments using a parallel plate flow chamber have demonstrated that increasing the aspect ratio of microparticles increases their adhesion to the human umbilical vein endothelial cells (HUVECs) in shear flow. This increase in adhesion with a higher particle aspect ratio is more pronounced for larger particles. However, for nanoparticles, no significant difference is observed between particles of different aspect ratios.[29] Follow-up confocal studies show that despite having increased binding, rod localization to the cell-free layer remains the same as that of spheres.[29] Thus, the observed increased adhesion of rods can be attributed to their increased contact area with the wall, having a higher total number of targeting ligands when the ligand density is fixed, and reduced drag forces acting to detach them from the wall.[29] These results were confirmed by *in vivo* experiments validating the increased adhesion of microrods compared with the spheres of the same volume in inflamed mouse aortae, whereas nanorods and nanospheres did not show any significant difference in their adhesion.[69] To summarize, different *in vitro* and *in*

vivo studies have verified the margination, and binding of microparticles suggest that changing the particle shape can be a useful strategy to improve the binding of particles, especially larger particles and higher aspect ratios.

1.5. Common Methods for the Fabrication of Polymeric Particles

In this section, we will discuss various methods for the fabrication of polymeric micro/nanoparticles, and the advantages and drawbacks of each of these techniques. Microfluidics and templating methods are two of the approaches used for the fabrication of biodegradable particles.[70–72] These techniques produce monodisperse particles with accurate control over their size, shape, and surface morphology and also provide the capability of fabricating multi-compartmental particles.[71,72] However, the required expensive and complex instrumentation, low throughput, and scale-up issues limit the utilization of these techniques.[72] Nanoprecipitation is another technique for the fabrication of polymeric particles. In this method, the injection of the polymer solution in a water-miscible organic solvent into a continuously stirred water phase enables the formation of the particles.[73] Despite being highly scalable, this method is limited by its incapability of loading hydrophilic entities within the polymer matrix.[73] Spray-drying is another commonly used method for the production of drug-loaded polymeric particles.[74] Despite producing stable powders as the final product, the high maintenance cost of the instrumentation, clogging at the nozzle entrance, and loss of the polymer and drug due to sticking to the chamber wall have limited the utilization of this method.[75]

Emulsion solvent evaporation (ESE) method is the most common technique for the fabrication of biodegradable particles due to its simple and scalable setup.[72] In this method, the biodegradable polymer will be dissolved in a volatile organic solvent to make the oil phase.[74,75]

The oil phase will then be emulsified in a water phase containing a surfactant as the stabilizer of the emulsion.[75] After the initial emulsification step and formation of the emulsion droplets, the mixture needs to be continuously agitated to allow complete evaporation of the oil-phase solvent and subsequent solidification of the emulsion droplets.[74] In this method, hydrophobic drugs can be easily loaded in particles via their addition to the oil phase.[76] However, an additional emulsification step is required to enable the loading of hydrophilic drugs, which include most of the biologics used in controlled release systems.[77] The resultant partitioning of the drug to the water phase limits the loading efficiency of hydrophilic cargos in this technique, which demonstrates the need to modify the ESE techniques to enable efficient loading of hydrophilic entities.[74,77]

1.6. Dissertation Outline

As mentioned in the previous section, the shape of particles can significantly improve their *in vivo* efficacy with non-spherical particles demonstrating the most promise in this regard. However, there is still a lot to be known about the impact of the shape on the interaction of particles with different cells of the body. Furthermore, there is a lack of a simple and scalable method for the large-scale fabrication of non-spherical particles from biodegradable and/or biocompatible polymers to enable their transformation in clinics. Thus, this thesis is focused on studying the impact of the shape on the efficacy of the drug carriers and developing new emulsion-based techniques for the fabrication of non-spherical biodegradable microparticles on large scales.

Chapter 1 provides a background about biodegradable drug carriers, factors that impact their efficacy, the existing information about the effect of the shape on the performance of these carrier systems, and existing methods for fabrication of biodegradable particles.

Chapter 2 is a description of the methods and experimental techniques used for the collection of the data discussed throughout the rest of the dissertation.

In Chapter 3, we have explored how shape will affect the phagocytosis of the polymeric particles and their interaction with different leukocyte sub-groups. Specifically, we have demonstrated how the shape modifications can be used to specifically target neutrophils in inflammatory conditions while keeping the phagocytosis of the particles by other leukocyte groups minimal.

In Chapter 4, we looked into developing a method that enables the fabrication of biodegradable rods on a large scale to enable their utilization in selective targeting applications discussed in Chapter 3. A novel emulsion-based method has been discussed to fabricate rod-shaped biodegradable polymeric particles in large scales. Next, these particles have been coated with targeting ligands, and their *in vitro* and *in vivo* binding efficacy to an inflamed vasculature has been studied.

In Chapter 5, we have developed a new metal-assisted emulsion-based templating technique to fabricate solid matrix hexagonal and rod-shaped particles composed of bile salts, i.e., cholate and deoxycholate. This chapter shows how the reduction of the metal ions can be used to guide the self-assembly of the salts at the oil-water interface to fabricate non-spherical biodegradable particles.

In Chapter 6, we have explored the potential of the composite bile salt microparticles fabricated in Chapter 5 to lyse the adipose tissue and induce apoptosis in cancer cells both *in vitro* and *in vivo*. This chapter shows how these novel particles can be used as controlled release therapeutic systems for the treatment of various conditions.

In Chapter 7, we have looked into how the shape modifications can affect the release profile of the loaded cargo from biodegradable particles. We have also looked into modification of the fabrication conditions within a double emulsion solvent evaporation technique to prolong the release profile of the hydrophilic drugs from the polymeric particles while increasing their loading efficiency during the fabrication.

Chapter 8 provides the conclusions for this dissertation and discusses the future directions and outlook for this work.

CHAPTER 2: Materials and Methods

2.1. Introduction

This chapter provides the detailed experimental protocols utilized to generate the experimental data in the next five chapters. A range of methods for fabrication of different biodegradable particle formulations are provided, and different *in vitro* and *in vivo* techniques used for testing the efficacy of the fabricated formulations in different disease models are detailed.

2.2. Materials

Poly(vinyl alcohol) (PVA) (MW = 30,000–70,000 m), chloroform (anhydrous >99.0%, containing 0.5–1.0% ethanol as stabilizer), dichloromethane (DCM), ethyl acetate, acetonitrile, methanol, ethanol, Trizma base, Nile Red, Bovine Serum Albumin (BSA), N-(3-Dimethylaminopropyl)-N'-ethylcarbodiimide hydrochloride (EDAC), hydrochloric acid (36.5–38.0%, bioreagent), 2-mercaptoethanol, gold (Ⅲ) chloride hydrate, sodium citrate, sodium cholate, sodium deoxycholate, rhodamine, and sodium hydroxide were purchased from Sigma-Aldrich (St Louis, MO). Sodium tripolyphosphate was purchased from Alfa Aesar (Ward Hill, MA). Sodium metaphosphate was obtained from Fisher Chemicals (Fair Lawn, NJ). Poly (lactic-co-glycolic acid), PLGA, polymer (DLG 4.5A) was purchased from Evonik Industries (Birmingham, Al) for rod fabrication studies. 50:50 PLGA polymer with carboxylic acid end groups used in the phagocytosis assays (IV = 0.66dL/g) was purchased from DURECT Corporation (Cupertino, CA). NeutrAvidin Protein and Dulbecco's phosphate-buffered saline (DPBS) were purchased from Invitrogen (Carlsbad, CA). Dextran was purchased from Spectrum Chemical Manufacturing

Corporation (New Brunswick, NJ). Fluorescein (FITC) Goat IgG and FITC Goat Anti-Mouse IgG were purchased from Jackson ImmunoReseach (West Grove, PA). The human ICAM-1/CD54 biotinylated antibody was obtained from R&D systems (Minneapolis, MN). Biotin Rat IgG1k isotype control and Biotin Rat Anti-Mouse CD62P were purchased from BD Bioscience (San Jose, CA). FITC anti-Rat IgG1 was purchased from Novus Biologicals (Littleton, CO). Human Interleukin 1-b (IL1-b) was purchased from Fitzgerald Industries International (North Acton, MA). Recombinant Human TNF-α was purchased from BioLegend (San Diego, CA). Proteolipid protein (HSLGKWLGHPDKF) (PLP139–151) was purchased from GenScript USA Inc. (Piscataway, NJ). Cyanine 5.5 amine dye was purchased from Lumiprobe (Florida, USA). N-hydroxysuccinimide (NHS) was purchased from Thermo Fisher Scientific (Waltham, MA). Fluoresbrite YG carboxylate microspheres of different sizes were purchased from Polysciences (Warrington, PA). 2-µm sky blue polystyrene carboxylate microspheres were purchased from Spherotech (Lake Forest, IL). Granulocyte-macrophage colony-stimulating factor, GM-CSF, was purchased from PeproTech (Rocky Hill, NJ). Human monocyte isolation kit was purchased from BioVision Incorporated (Milpitas, CA). Cell Dissociation Buffer Enzyme-Free Hanks'-Based was purchased from Life Technologies (Carlsbad, CA). Mycobacterium tuberculosis H37Ra was purchased from Difco (Detroit, MI). Fetal Bovine Serum (FBS) was purchased from Atlanta Biologicals (Flowery Branch, GA). Anti-human CD45, anti-mouse/human CD11b, anti-human CD47, anti-mouse CD45, anti-mouse Ly-6G, and anti-mouse Ly-6C antibodies were purchased from Biolegend (San Diego, CA). CellTiter 96® Aqueous One Solution Cell Proliferation Assay (MTS) was purchased from Promega Corporation (Madison, WI). Free fatty acid measurement kit was purchased from Cayman Chemicals (Ann Arbor, MI).

2.3. Human and Animal Study Approvals

Fresh human blood used in all in vitro assays was obtained via venipuncture. The blood draw protocol used was approved by the University of Michigan Internal Review Board (IRB-MED). All human subjects provided written consent before blood collection. Umbilical cords were obtained under a University of Michigan Medical School Internal Review Board (IRB-MED) approved human tissue transfer protocol, which is exempt from informed consent per federal exemption category #4 of the 45 CFR 46.101.(b).

Animal studies were conducted following the National Institutes of Health guidelines for the care and use of laboratory animals and approved by the Institutional Animal Care and Use Committee (IACUC) of the University of Michigan. C57BL/6 and BALB/c mice were obtained from Jackson Laboratories. All animals were maintained in pathogen-free facilities at the University of Michigan.

2.4. Particle Fabrication

2.4.1. One step PLGA rod fabrication

The one-step fabrication was completed as previously described by Heslinga et al. with minor changes.[78] Briefly, an aqueous phase was prepared by dissolving the desired concentration (1– 3%) of PVA and 2.0% sodium tripolyphosphate, a surface-active molecule in deionized water; then the pH was adjusted to 8.4. The oil phase was prepared by dissolving PLGA polymer at 1.8 mg/ml concentration in 12.5 ml chloroform. The oil phase solution was then injected into 100.0 ml of the aqueous phase, which was continuously stirred at the desired speed of 2500–5500rpm (Caframo overhead mixer, model: 6015, fitted with a 2.8 cm glass propeller; Beckman Coulter). The emulsification was continued for 2 h to allow the stretching of the droplets and complete

17

evaporation of the organic solvent. Spherical particles of the same size were fabricated by the same procedure except with no surface-active molecule in the aqueous phase solution. Particles were collected and washed two times by centrifugation at 3500 rpm and lyophilized. The powder was stored at 20 °C until usage.

2.4.2. Two-step PLGA rod fabrication

The first step aqueous solution was prepared by dissolving 1.0% PVA and the surface-active molecule of choice (Trizma base, sodium tripolyphosphate, or sodium metaphosphate) in DI water and adjusting the pH at 8.4. The oil phase was prepared by the same protocol as the one-step fabrication (unless otherwise specified) in 12.5 ml of chloroform or dichloromethane. The oil phase solution was injected into 50.0 ml of the aqueous phase continuously stirred (2500–5500 rpm) with the overhead mixer. The mixing was continued for 15 min to allow the complete formation of the emulsion droplets. The second step aqueous solution was prepared by dissolving the PVA (2.0–8.0%) and the desired surface-active molecule in DI water, setting the pH at 8.4. After 15 min of mixing, 50.0 ml of the second step solution was poured into the fabrication mixture to induce a sudden increase in the viscosity of the solution and to allow the stretching of the previously formed, spherical emulsion droplets. The emulsification was continued for 2 h to allow the stretching of the emulsion droplets and complete evaporation of the organic solvent. The fluorescently loaded particles were fabricated in the same manner as unloaded particles except for 1.0 mg of Nile Red was dissolved along with the PLGA polymer in the oil phase. The formed particles were collected and washed by two-times centrifugation at 3500 rpm and subsequently lyophilized and stored at 20 °C until usage.[79]

2.4.3. Polystyrene rod fabrication

Polystyrene carboxylated microspheres were stretched into rods using a previously described film stretching method. [23] Briefly, 100 µl of the original particle stock was added to 10 ml of 7% polyvinyl alcohol (PVA) and dried to a film via overnight incubation at 45 ºC in a single-well Omni Tray. After 24 h, the dried film was peeled off of the tray and cut into 3×1 cm pieces and stretched at 200 ºC using a syringe pump. The aspect ratio of the particles was adjusted by changing the total draw volume of the pump. The films were first washed by dissolving them in 70% isopropanol solution and then subsequently with water to remove the residual PVA.

2.4.4. Fabrication of bile salt-based composite microparticles

Microparticles were fabricated using the modified double emulsion solvent evaporation method combined with the *in-situ* reduction of the Au (Ⅲ) ions within the emulsion droplets. Briefly, sodium citrate (30 mg) and gold (Ⅲ) chloride hydrate (25 mg) were dissolved in water (50 µl) and emulsified in ethyl acetate (1.0 ml) via vortexing for 15 seconds. Afterward, 2 ml of concentrated sodium cholate/deoxycholate solution (0.75-3%) was added to the first emulsion, and the mixture was vortexed for another 15 seconds. The emulsion was then added to 0.3% sodium cholate/ deoxycholate solution (10 ml) and heated for 15 minutes at 45 °C in a closed glass vial using a water bath. The emulsion was then stirred on a stir-plate at 220 rpm at room temperature for 2 h for evaporation of the ethyl acetate. Rhodamine-loaded particles were fabricated with the same protocol by adding rhodamine (2 mg) to the inner water phase. Large gold precipitates and larger particles were filtered out using a mesh filter with a pore size of 20 µm. Composite particles were then collected and separated from gold nanoparticle via low-speed centrifugation at 600 rpm for 5 minutes and discarding the supernatant.

2.4.5. Anti-CD47-loaded PLGA fabrication

The antibody-loaded particles were fabricated with the emulsion solvent evaporation technique. Oil phase solvents were prepared by adding different cosolvents, i.e., ethyl acetate, acetonitrile, ethanol, and methanol, to chloroform in a 1:8 ratio (unless specified otherwise). For the trials without cosolvents, pure chloroform was used as the cosolvent. Acid-terminated PLGA polymer was dissolved in the oil phase (25 mg/ml unless specified), and then a known amount of BV421 tagged anti-human-CD47 was emulsified in 2 mL of the oil phase via vortexing. Afterward, the oil phase was emulsified in 4 mL of 5% PVA at a pH of 7.0 via sonication at 40% amplitude. The mixture was then diluted with 10 mL of 1% PVA at a pH of 7.0 and stirred on a stir plate at 300 rpm for 2 h to allow the complete evaporation of the oil phase solvents. Subsequently, the nanoparticles were collected via centrifugation at 15000 rpm for 5 minutes and three times washed in water. The particles were then dried using a Labcono Lyophilizer and stored in the freezer at 20 ºC until usage. The particles and the emulsions were covered with foil during all the fabrication steps to prevent the loss of the fluorescent signal.

2.5. Particle Characterization

2.5.1. Microscopy characterization

Brightfield and fluorescent imaging were performed with the Nikon E-800 Widefield Microscope, with 40X, 60X in DIC mode, and 100X objectives. The rod fabrication yield and spheroid ratio were quantified by counting the number of particles in each field of view and dividing the number of rods (AR>2) to the total number of the particles. Particles with an aspect ratio of two or higher were considered rods. The reported yield is the average of 3 batches ± standard error between different batches. The particle size, reported as the average ± standard deviation, was measured with NIS-Elements (AR 4.30.01) software for at least 100 particles per

batch and averaged over three batches. Statistical analysis of particle size was done via a two-way ANOVA test (PRISM software). SEM micrographs were obtained with JEOL-7800FLV FE-SEM. Samples for SEM were prepared by suspending particles in DI water and allowing these to be dried on a clean glass slide. Dried particle samples were sputter-coated with gold before SEM imaging. Confocal images were obtained with an Olympus FV 1200 Confocal Microscope.

2.5.2. *Bile salt microparticle characterization*

Zeta potential of the microparticles was measured via dynamic light scattering (DLS) using a Malvern Zetasizer. Energy-dispersive spectroscopy (EDS) and X-ray photoelectron spectroscopy (XPS) analyses were used to characterize the elemental composition of the hexagons. EDS analysis was performed on the microparticles by an Oxford XMaxN 80 mm^2 silicon-drift energy-dispersive X-ray spectrometer. For XPS analysis, the particles were mounted on indium foil, and the XPS analysis was done via a Kratos Axis Ultra XPS machine. HPLC and proton NMR analyses were used to confirm the presence of cholate as the primary component in the structure of the hexagons. For these analyses, dried particles were degraded in a 50:50 mixture of acetonitrile and water and centrifuged to separate the residual gold entrapped within their structure. The supernatant was collected and analyzed with HPLC alongside a 1% standard sodium cholate solution in 50:50 acetonitrile and water. The raw HPLC data of intensity for different retention times for both the samples were plotted using Graphpad prism software. For NMR analysis of the cholate-based particles, the degradation products were freeze-dried with a Labcono Lyophilizer and dissolved in deuterated water and analyzed with a Varian MR400 NMR machine alongside standard sodium cholate solution. For the deoxycholate-based particles, the spectra of the degradation products and a 1% standard solution were collected in a 50:50 mixture of deuterated acetonitrile and water.

2.6. Degradation and Release Assays

2.6.1. *In vitro release assays from Nile Red-loaded PLGA rods*

In vitro release studies of Nile-Red from the loaded particles were performed in DPBS at 37 ℃. Briefly, 5×10^8 particles were suspended in 1.0 ml of DPBS and rotated on a shaker at 37 ℃. At the desired time point, the particle suspension is centrifuged at 8000 rpm for 5 min, and the supernatant removed to measure the amount of dye released from the particles. The fluorescence intensity of the solution is then measured and quantified as described for the quantification of therapeutic loading. The pellet was resuspended in fresh DPBS buffer and rotated for subsequent time points. The release study was performed in triplicate for each particle type.[79]

2.6.2. *Bile salt microparticle degradation assays*

For the microparticle degradation assays, particles were first freeze-dried with a Labcono Lyophilizer. Dried particles were then resuspended in deionized water at the concentration of 10^6 particles/ml and rotated on an end-to-end rotator at 37 ℃. At different desired time points, a droplet of the particle suspension was taken and dried on a glass slide and imaged via SEM to visualize their surface morphology. The cholate release assays were performed via the same protocol. At the desired time points, the particle suspension was spun-down, and the supernatant was collected. The amount of the released cholate was measured using HPLC and via quantification of the area under the curve and comparing it to a calibration curve.

2.7. Quantification of Therapeutic Loading and Encapsulation Efficiency

Nile Red encapsulation efficiency was calculated by dissolving the particles in dichloromethane after fabrication. The encapsulated dye was dissolved in methanol after complete evaporation of dichloromethane and the fluorescent intensity measured with a Biotek microplate reader at an excitation and emission wavelength of 530 nm and 635 nm, respectively. The

fluorescence measurements were converted to concentration using a calibration curve generated with a known concentration of the dye. Therapeutic loading is calculated by dividing the mass of the entrapped Nile Red by the mass of dry PLGA particles. Encapsulation efficiency is calculated by the ratio of the mass fraction of the dye in dried particles to the mass fraction of dye in the oil phase used for particle fabrication.[78]

2.8. Microparticle Functionalization

Particles were covalently conjugated with NeutrAvidin protein using carbodiimide (EDAC) chemistry, as previously described with slight modifications.[22] Briefly, particles were incubated in 5.0 mg/ml NeutrAvidin in 50 mM MES buffer (pH = 4.5) for 20 min. Afterward, the same volume of 75 mg/ml EDAC in 50 mM MES buffer was added to the reaction mixture and incubated for 20 h. The reaction was stopped with 100 mM glycine. Avidin-conjugated particles were washed two times with DPBS buffer (1% BSA; pH = 7.4) and stored at 4 °C until use. For antibody conjugation, avidin-coated particles were incubated in biotinylated anti-ICAM-1 or biotinylated anti-P-selectin solution in DPBS buffer for 45 min. Antibody-conjugated particles were then washed 2 times with DPBS and stored at 4 °C until use. The antibody site density on the particles was characterized using flow cytometry with FITC-goat anti-mouse IgG and FITC- Goat IgG used for the stain and isotype control, respectively. FITC anti-Rat IgG_1 and biotin Rat IgG_{1k} isotype control were used to determine the site density of anti-P-selectin coated particles.

2.9. Interfacial Tension Measurement

The interfacial tension between the oil phase (1.8 mg/ml PLGA in 12.5 ml Chloroform) and the water phase containing one of the different surface-active molecules at their optimum

concentration was measured with the pendant drop method using needle SNS051/026 at 21 ºC by the DataPhysics company.

2.10.   Parallel Plate Flow Chamber Adhesion Assays

Human umbilical vein endothelial cells (HUVECs) were cultured on glass coverslips as previously described.[22] Blood from human donors was drawn with the anticoagulant acetate citrate dextrose (ACD) and stored at 37 ºC until use. Red Blood Cells (RBCs) were separated from collected whole blood by adding 6% dextran to the blood in an inverted syringe. RBCs were washed three times by suspending in DPBS and centrifugation at 2250g for 20 min. RBC sample was then reconstituted in DPBS with 1% BSA at 40% hematocrit (% v/v). HUVECs on gelatin-coated coverslips were activated as previously described with IL-1β.[22] Targeted particles at a fixed concentration of 1×10^6 particles/mL were mixed with RBCs in buffer mixture previously prepared and then perfused through the PPFC in a laminar flow profile for 5 min. The volumetric flow rate through the channel (Q) was controlled via a syringe pump. Wall Shear Rate (WSR, γ_w) can be calculated as shown in Equation (2.1), where h is the channel height (0.0127 cm), w the channel width (0.25 cm), and Q the volumetric flow rate (ml/s). Adherent particles were visually counted and normalized to the HUVEC surface area, resulting in reported #particles/mm^2 for all experiments. Data were averaged over ten images for each trial and repeated for three trials for each data point. Data are reported as the average ± standard error of the mean in all figures. A two-tailed t-test on GraphPad Prism (P < 0.05) was used to analyze any statistical difference between various conditions.

$$\gamma_w \; (S^{-1}) = \frac{6Q}{h^2 W} \text{ (Equation 2.1)}$$

2.11. Intravital Fluorescent Microscopy

Mesentery vessels were visualized as previously described.[80] Briefly, male mice (3–4 weeks) were anesthetized. A midline incision in the abdominal cavity was made for exteriorization of the mouse intestines and the mesentery connective tissue. Mice were placed on a custom-made microscope heated stage at 37 ºC, and the mesentery was positioned on a glass coverslip. A local injury was induced by topical application of TNF-α (10 μL of 200 μg/ml in PBS). At 2 min after TNF-α activation, particles suspended in 100 μL PBS (10^8 particles/mice) were injected using retro-orbital injection and continuously imaged for another 10 min via both brightfield and fluorescent microscopy. Targeted particle adhesion in mesenteric veins was visualized under a 25X oil objective using an inverted fluorescence microscope (Zeiss Axio Observer Z1 Marianas Microscope). Adhesion data were determined by the number of individually bound particles for n = 3 mice and reported as #of bound particles/mm^2 mice vessels.

2.12. Cell Culture

Rat alveolar macrophages (ATCC® CRL2192™) were bought from American Type Culture Collection, ATCC. Upon arrival, the frozen cell vial was thawed and resuspended in 9.0 mL of macrophage culture media (85% Ham's F12K medium with 2 mM L-glutamine adjusted to contain 1.5 g/L sodium bicarbonate, ATCC® 30-2004™) containing 15% heat-inactivated fetal FBS, and centrifuged at 125 g for 7 minutes. The supernatant was aspirated, and the cells were resuspended in 15 ml of warm fresh media and transferred to a T75 ml culture flask and incubated at 37 ºC and 5% CO_2. The concentration of the cells was counted each day, and when the concentration of the floating cells reached 5×10^5 cells/ml, the cells were collected via trypsinization and utilization of a cell-scraper. The cell suspension was then centrifuged at 125 g

for 7 minutes, reconstituted in fresh media to the concentration of 2×10^5 cells/ml, and transferred to a new flask. The cell media was changed 2-times per week.

Human THP-1 monocytes were purchased from ATCC (ATCC® TIB-202™). The frozen cells were thawed and added to 10 ml of warm THP-1 media (ATCC formulated RPMI-1640 media with 10% FBS and 0.05 mM mercaptoethanol). The cell suspension was then centrifuged at 200 g for 7 minutes to collect the cells. The media was aspirated, and the cells were resuspended in 10 ml of fresh media and transferred to a T75 flask and incubated at 37 ºC and 5% CO_2. When the concentration of the cells reached to 10^6 cells/ml, the cells were centrifuged, diluted to the concentration of 2×10^5 cells/ml, and transferred to new flasks. The media was refreshed 3-times per week.

2.13. Isolation of Bone Marrow-derived Macrophages and Dendritic Cells

Macrophages and dendritic cells were generated as previously described.[81] Bone marrow cells were collected by flushing femurs and tibias of mice. The cells were cultured in RPMI 1640 GultaMAX supplemented with 10% FBS and 1% penicillin/streptomycin. To obtain macrophages, culturing media were further supplemented with either 20% L929 conditioned media, and macrophages were removed using Cell Dissociation Buffer Enzyme-Free Hanks'-Based. To obtain dendritic cells, culture media were supplemented with 50 mM 2-mercaptoethanol and 20 ng/ml GM-CSF, and dendritic cells were obtained from suspension.

2.14. *In vitro* Uptake Studies

Uptake studies were performed with the general protocol previously described.[41] For polystyrene whole blood uptake studies, particles were added to 100 µL of human or mouse blood (at a concentration of 10^7 particles/ml unless specified),

and incubated at 37ºC and 5% CO_2 for 2 hr. Competitive uptake studies were performed by incubating the same concentration (5×10^6 particles/ml) of the 2 μm carboxylate polystyrene sky blue spheres and green rods of the same volume in whole blood for 2 hr. For PLGA particles, the particle concentration was set at 5×10^7 particles/mL, and the uptake time was reduced to 30 minutes. The samples were then stained with CD45 and CD11b antibodies (human blood) or CD45, CD11b, ly6G, and ly6C antibodies (mouse blood) for 30 minutes on ice. Afterward, 2 ml of 1X lyse-fix solution was added to each sample to lyse the red cells and fix the white blood cells and incubated with the samples for 1 h at room temperature. The samples were then centrifuged at 500xg for 5 minutes and washed with FACS buffer (1X PBS + 2% FBS) 3 times. The percentage of the particle positive cells in each sample was quantified via flow cytometry. For imaging, the competitive uptake assays, 2 μm spheres and AR6 rods of the same concentration (10^7 particles/ml) were added to the same sample, and the uptake assays were done as previously described. The cells were stained with PE anti-human CD45 antibody, and the particles within the cells were visualized via an inverted Nikon fluorescent microscope.

Human plasma was obtained by centrifuging whole blood at 2250g for 20 minutes. Human monocytes were isolated from whole blood using a human monocyte isolation kit and reconstituted in plasma to a concentration of 10^7 cells/ml and used for uptake studies with the protocol described below.

For macrophages, THP-1 monocytes, and dendritic cells, the cells were reconstituted in RPMI-1640 media at a concentration of 10^7 cells/ml for bone-marrow-derived macrophages and 5×10^6 cells/ml for THP-1 monocytes, rat alveolar

macrophages, and dendritic cells. 100 µl of the cell suspensions were added to each well of a 96-well plate and incubated with particles (10^7 particles/ml unless specified) for 2 hr. For macrophages, the cells were incubated in the plates for 30 min before adding the particles to allow their adherence to the plate. After 2 h, the macrophages and dendritic cells were detached respectively with trypsin or 1X versine solution. The cells were removed from the wells and transferred to 5 mL Falcon tubes. The samples were then fixed using 2 ml of 4% paraformaldehyde solution for 1 h. Afterward, the samples were washed 3 times using FACS buffer at 500xg for 5 minutes and run on a flow cytometer to check their association with particles.

2.15. Mouse Immunization

Female SJL/J mice were purchased from Envigo. Peptide-induced EAE was induced in SJL/J mice as previously reported.[82] 8–10 weeks old female mice were immunized subcutaneously at three spots on the flank with 100 µl of an emulsion of PLP peptide in CFA containing 200 µg Mycobacterium tuberculosis H37Ra. Peripheral blood was collected from EAE mice 9 days after immunization.

2.16. *In Vivo* Uptake Studies

For the *in vivo* uptake studies, 1.5×10^9 particles were resuspended in 100 µl of PBS and injected a using tail vein catheter. 30 minutes post-injection, the animals were euthanized, and their blood was drawn into heparin-containing syringes using cardiac punctures. The blood samples were then using anti-mouse CD45, anti-mouse/human CD11b, anti-mouse Ly-6G, and anti-mouse Ly-6C for 30 minutes on ice. Afterward, the samples were lyse-fixed and centrifuged

at 500g for 5 minutes. The pellet was collected and subsequently washed twice with FACS buffer and ran on a flow cytometer to quantify the uptake of the particles by neutrophils and monocytes. Each condition was repeated for five individual animals.

2.17. *In Vitro* Adipocyte Lysis Assays

The primary subcutaneous human adipocytes cultured in 96-well plates were purchased from Zen-Bio (Research Triangle, NC). Upon arrival, 150 µl of the media was removed from each well, and the cells were incubated at 37 ºC and 5% CO_2. For the lysis assays, 150 µl of the salt solution or particle suspension of the known concentration in FBS free RPMI-medium was added to each well and incubated with the cells for a known time-point. Afterward, the treatment solution was aspirated, the cells were washed with warm PBS, and 150 µl of the 1:25 dilution of MTS assay cell titer purchased from Promega Corporation (Madison, WI) in 1X PBS was added to each well and incubated at 37 ºC and 5% CO_2 for 3 h till the appearance of the orange color in the untreated control wells and the absorbance was measured at 490 nm. The percentage of the cell viability was quantified via subtracting the background cell titer absorbance from the absorbance of the desired point and dividing it by the average signal of the untreated cells after subtracting the background.

2.18. *Ex Vivo* Fat Lysis Assays

For the tissue lysis assays, a known mass of the beef adipose tissue was incubated with either of the PBS, salt solutions, or the particle suspensions at 37 ºC for known time-points. Thereafter, the turbidity of the solution was measured by measuring the absorbance at 660 nm, and the appearance of the tissue was visualized. The amount of the released fatty acids in the mixture

was quantified via a free fatty acid quantification kit purchased from Cayman Chemicals (Ann Arbor, MI).

2.19. *In vivo* Adipocyte Lysis Assays

8-10 weeks old male C57BL/6J diet-induced obese mice were used in the *in vivo* studies. Briefly, 2.5 mg of bile salts or composite particles in 100 µl PBS were subcutaneously injected into the right inguinal fat pads of the animals. 100 µl PBS was injected into the left fat pad as control. The weight of the individual animals was tracked over time. One week post- injection, the animals were euthanized, their blood was collected via cardiac puncture, and their fat pads were removed and fixed in 10% formalin. The experiments were replicated for four animals in each group.

2.20. Statistical Analysis

Statistical analysis of the data was performed using GraphPad Prism. Each data point was replicated for at least N=3. Depending on the sets of the data, unpaired t-test, One-way ANOVA with Tukey's post-test (95% confidence interval), or two-way ANOVA with Bonferroni post-tests were used to compare the significance of different points.

CHAPTER 3: Impact of Shape on the Phagocytosis of Particles by Different Leukocyte Sub-types

3.1. Publication Information

3.2. Abstracts

Polymeric particles have recently been used to modulate the behavior of immune cells in the treatment of various inflammatory conditions. However, there is little understanding of how physical particle parameters impact their specific interaction with different leukocyte subtypes. Importantly, while particle shape is known to be a crucial factor in their phagocytosis by macrophages, where elongated particles are reported to experience reduced uptake, it remains unclear how shape influences particle phagocytosis by blood circulating phagocytes, including neutrophils that are the most abundant leukocyte in human blood. In this study, we investigated the phagocytosis of rod-shaped polymeric particles by human neutrophils relative to other leukocytes. In contrast to macrophages and other mononuclear phagocytes, neutrophils were found to exhibit increased internalization of rods in *ex vivo* and *in vivo* experimentation. This result suggests that alteration of particle shape can be used to selectively target neutrophils in inflammatory pathologies where these cells play a significant role.

3.3. Introduction

Neutrophils and monocytes are the most prominent phagocytes in the bloodstream in humans, collectively comprising about 60 to 80% of blood leukocytes,[83,84] due to their essential role as our body's first defense against invading pathogens or responder in the case of injury.[15,85] Furthermore, recent studies have demonstrated that neutrophils are a significant contributor to the *in vivo* clearance of intravenously injected particles.[38,39] However, neutrophils and monocytes are increasingly negatively implicated in many human pathologies. For instance, neutrophils are vital contributors to the severity of autoimmune diseases, such as antiphospholipid syndrome and multiple sclerosis,[15,86] sepsis,[87] ischemic stroke,[88] and chronic inflammatory airway diseases.[89] Excessive infiltration of neutrophils and increased neutrophilic inflammation,[15,89] or their failure to be recruited to the infection site,[87] are among the main factors contributing to the severity of these disorders. Alongside the neutrophils, inflammatory monocytes also play a significant role in autoimmune disorders, viral infections, and ischemia-reperfusion injury.[90] Thus, depletion of neutrophils and inflammatory monocytes from the circulation has been investigated for reducing symptoms for the conditions mentioned above.[15,89] Steroids, anti-inflammatory agents, antibodies, and siRNA delivery systems are some of the approaches previously explored for this purpose.[90,91] However, most of these systems are either complex with cytotoxicity issues or have not been fully efficient in delivering a therapeutic benefit.[90,92,93]

The utilization of biodegradable particles for targeting blood leukocytes has been recently introduced as a strategy for the treatment or controlling the severity of many of the inflammatory conditions mentioned above. As an example, biodegradable particles have been used to modulate immune cells to reduce inflammation and disease symptoms in lupus, spinal cord injury, and sepsis

models.[14,15,94,95] However, there is little known about the specificity of these systems for targeting various leukocyte subpopulations. Despite their similarities, there have been several reports on structural differences between different leukocyte subgroups, i.e., neutrophilic polymorphonuclear leukocytes (PMNs) and mononuclear phagocytes (MNPs), which include monocytes, macrophages, and dendritic cells.[96] The differences in the monocyte chemotactic responses and metabolic burst activity during phagocytosis, their higher level of expression of toll-like receptors, and their capacity for cytokine production compared to neutrophils are amongst the known differences.[97] Some recent studies have also reported differences between the interaction of particles with neutrophils compared to other leukocytes. For example, Kelley et al. recently showed that the presence of poly(ethylene glycol) (PEG) chains on polymeric particle surface increase their phagocytosis by primary human neutrophils, which is the opposite of the observed trend for other phagocytic cells such as macrophages and monocytes.[41]

A compounding factor in our understanding of the interaction of particulate carriers with leukocytes is the fact that most studies have been either *in vivo* in mice or with immortalized mouse-derived cells in culture, which may not fully capture the behavior of human leukocytes. Furthermore, most of the available literature in this regard have focused on the impact of spherical particle size and surface chemistry on phagocytosis.[24,98–100] To date, there is a limited understanding of how particle shape prescribe their interactions, i.e., phagocytosis and blood clearance, with circulating leukocytes [36] despite a seminar paper by Mitragotri and co-workers demonstrating that macrophages do not successfully internalize microparticles from their low curvature side (major axis).[23] A few other validated this finding that sufficiently elongated particles can avoid phagocytosis by macrophages,[58,59,101] leading to an increase in their *in vivo* circulation time.[102] However, considering the differences between neutrophils and mononuclear phagocytes

discussed in the previous paragraph, it remains unclear how neutrophils and other phagocyte groups will internalize particles of varying shapes.

Here, we investigated the effect of particle aspect ratio on phagocytosis by various human immune cell populations, including neutrophils, monocytes, and macrophages. We demonstrate that the neutrophil response to alterations in the shape of particles is the opposite of the prior observation for mononuclear phagocytes. While rods exhibit reduced phagocytosis by macrophages, monocytes, and dendritic cells, the association of neutrophils with particles significantly increased for rod-shaped particles both *in vitro* and *in vivo*. When particles were incubated in whole blood samples, we found that rods were selectively internalized by neutrophils, with up to 7-fold increased association with neutrophils, compared to monocytes. The observed trend of increased phagocytosis of rods by neutrophils was independent of the material type. Our results demonstrate that altering the shape of micro/nanoparticles can be used to selectively target neutrophils for the treatment of the different inflammatory conditions where neutrophils are the key controllers of the disorder.

	Equivalent Spherical Diameter (ESD)					
	500 nm		1 µm		2 µm	
Aspect ratio	Major axis	Minor axis	Major axis	Minor axis	Major axis	Minor axis
2	820 ± 110 nm	450 ± 51 nm	1.9 ± 0.7 µm	830 ± 85 nm	5.0 ± 0.5 µm	1.4 ± 0.1 µm
4	1.15 ± 0.2 µm	340 ± 50 nm	3.0 ± 0.35 µm	740 ± 100 nm	6.1 ± 0.7 µm	1.3 ± 0.1 µm
6	2.0 ± 0.5 µm	300 ± 48 nm	3.9 ± 0.6 µm	650 ± 90 nm	9.2 ± 3 µm	1.5 ± 0.5 µm

Table 3.1. The dimensions of polystyrene particles of different aspect ratios and sizes measured from SEM images.

3.4. Results

3.4.1. *Shape dependence of ex vivo uptake of polymeric particles by circulating blood leukocytes*

Commercial polystyrene particles of varying diameters (500 nm, 1 µm, and 2 µm) were stretched in a poly(vinyl alcohol), PVA, film in an oven using a syringe pump as previously described.[29] The total draw volume of the syringe pump was used to adjust the aspect ratio of the particles, and ellipsoidal rods with aspect ratios of 2, 4, and 6 were fabricated, as shown in Fig. 3.1. Table 3.1 shows the major and minor axis size of particles measured from SEM images, which is in close agreement with the theoretical dimensions of particles in Table 3.2, i.e., if they were perfect spheroids.

	Equivalent Spherical Diameter (ESD)					
	500 nm		1 µm		2 µm	
Aspect ratio	Major axis	Minor axis	Major axis	Minor axis	Major axis	Minor axis
2	800 nm	400 nm	1.6 µm	800 nm	3.2 µm	1.6 µm
4	1.25 µm	300 nm	2.5 µm	630 nm	5 µm	1.25 µm
6	1.65 µm	280 nm	3.3 µm	550 nm	6.6 µm	1.1 µm

Table 3.2. The theoretical dimensions of polystyrene particles of different aspect ratios if they were perfect spheroids.

Next, the uptake by primary human neutrophils of polystyrene particles of various aspect ratios was evaluated by incubating particles in whole blood for a 2-hr period. After gating for singlets via flow cytometry, CD45 and CD11b positive cells were identified, and the neutrophil population was isolated using the forward-scatter and side-scatter panels (Figure 3.2). The population of the particle-positive cells in the system was quantified by identifying the population of FITC-positive cells.
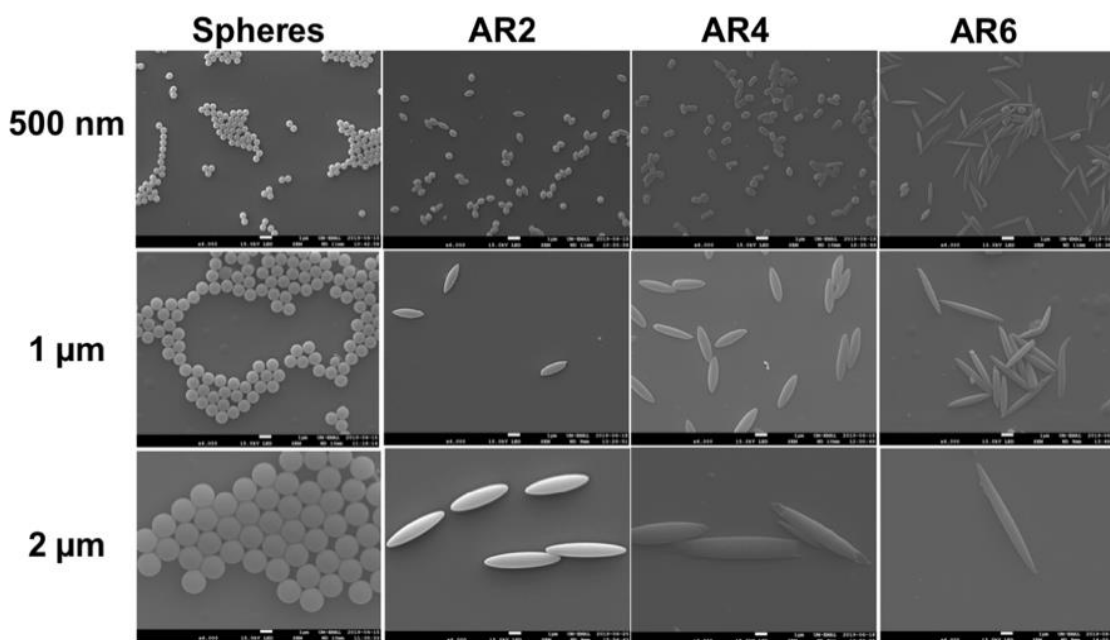
Figure 3.1. SEM image of polystyrene particles of different sizes and aspect ratios fabricated via the heat stretching technique in a PVA film.
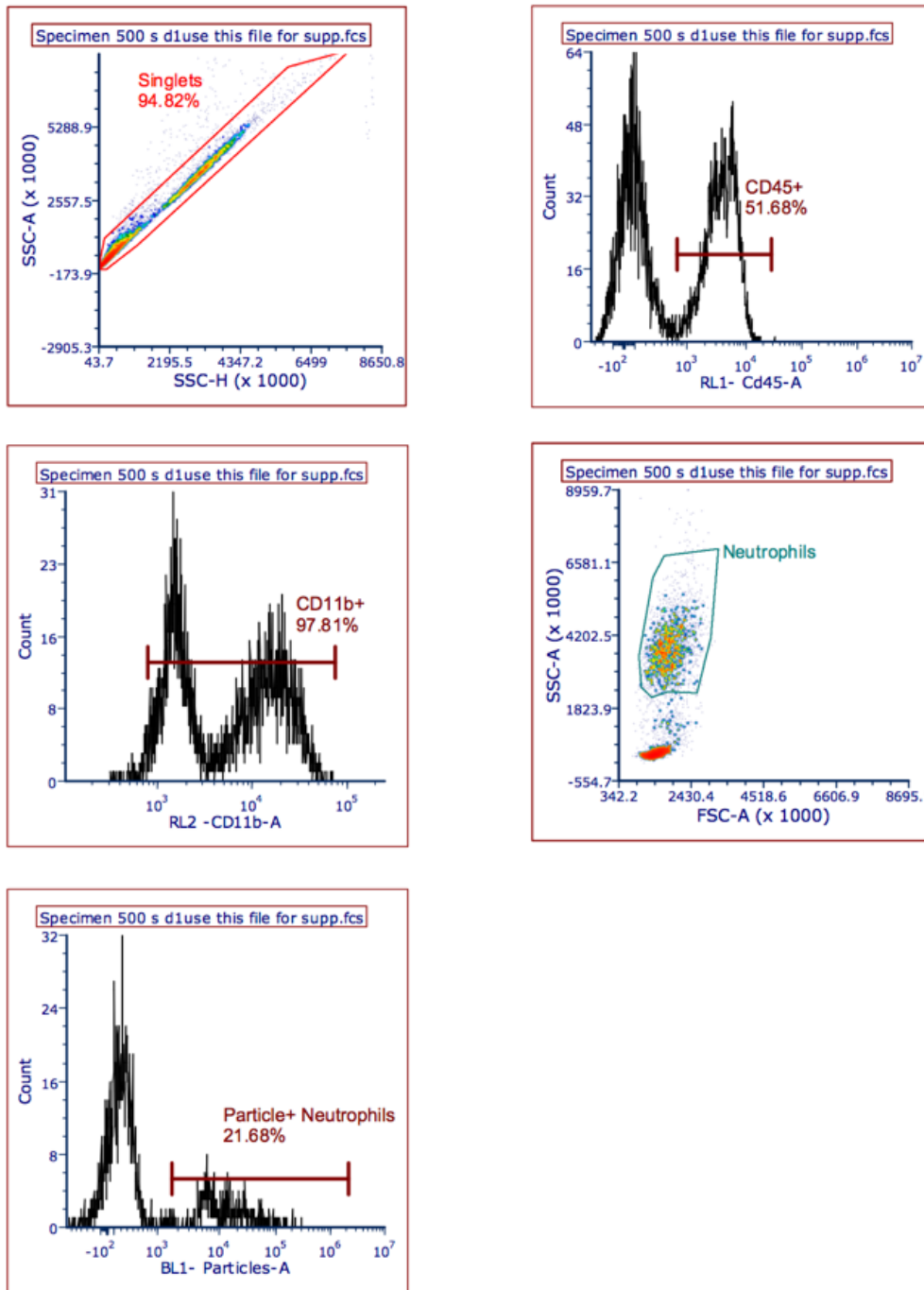
Figure 3.2. Representative gating of particle positive human neutrophils via flow cytometry.
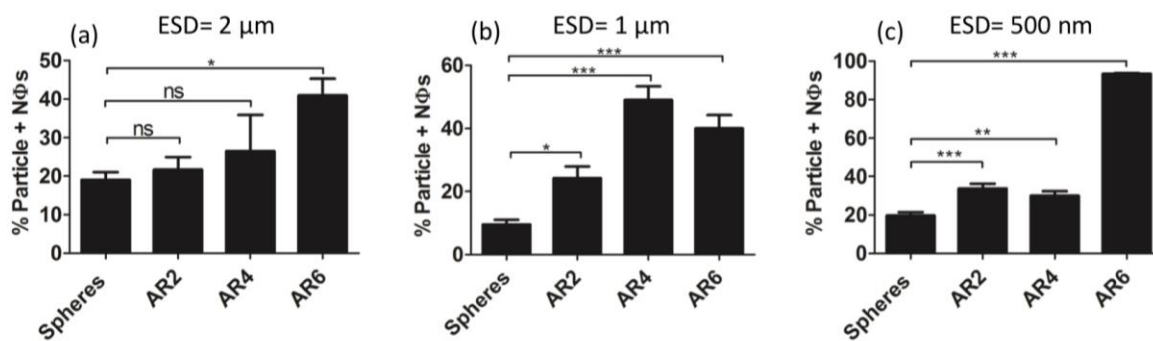
Figure 3.3. The effect of aspect ratio on the *ex vivo* uptake of particles with equivalent spherical diameter of (a) 2 μm, (b) 1 μm, and (c) 500 nm by primary human neutrophils in whole blood. The particle concentration in blood is set at 10^7 particles/ml for figures (a) and (b) and at 10^8 particles/ml for figure (c). One-way ANOVA with Tukey's post-test and confidence interval of 95% was used to analyze the figures (ns: $P>0.05$, *: $P<0.05$, **: $P<0.01$, ***: $P<0.001$).

Figure 3.3a shows the uptake by primary human neutrophils of 2 μm polystyrene spheres and rods of different aspect ratios (ARs) that were derived from the 2 μm spheres, i.e., having an equivalent spherical diameter (ESD) of 2 μm. Surprisingly, increasing the aspect ratio of these particles increased their association with human neutrophils. However, the difference was only significant for AR6 rods, which had a 2-fold higher uptake compared to spheres of the same volume. Similar to 2 μm particles, human neutrophils internalized 1 μm and 500 nm ESD rods more than spheres of the same volume. Moreover, the difference between the internalization of rods and spheres was significant for all the aspect ratios in the 1 μm and 500 nm size range. In particular, 1 μm AR2 particles exhibited a significant 2-fold increase in uptake by neutrophils compared to 1 μm spheres (Figure 3.3b). The difference between rods and spheres increased further for AR4 and AR6 rods having 1 μm ESD, where they respectively had 5- and 4-fold higher uptake than their spherical counterparts. For 500 nm particles, the concentration of the particles in blood was increased ten times compared to microparticles to 10^8 particles/ml due to their minimal uptake in the lower concentration range. However, the folds increase in uptake relative to spheres of the

38

500 nm ESD rods were smaller compared to the 1 μm for the short rods, with AR2 and AR4 displaying only a 1.5-fold increase in their uptake compared to spheres. At the largest aspect ratio of AR6, the 500 nm rods had a significant 5-fold increased uptake relative to their spherical counterparts (Figure 3.3c).

We also quantified the changes in the expression of CD11b, the protein subunit that mediates leukocytes adhesion and migration, on the surface of neutrophils after being incubated with different particles relative to untreated cells.[103] Previous results have demonstrated that an increase in particle internalization will increase CD11b expression by human neutrophils.[104] Our results demonstrated that the increase in the level of CD11b expression by human neutrophils after being incubated with the AR6 rods was significantly higher than spheres (Figure 3.4). For 500 nm particles, incubation with the rods resulted in 3-folds increase in the CD11b expression relative
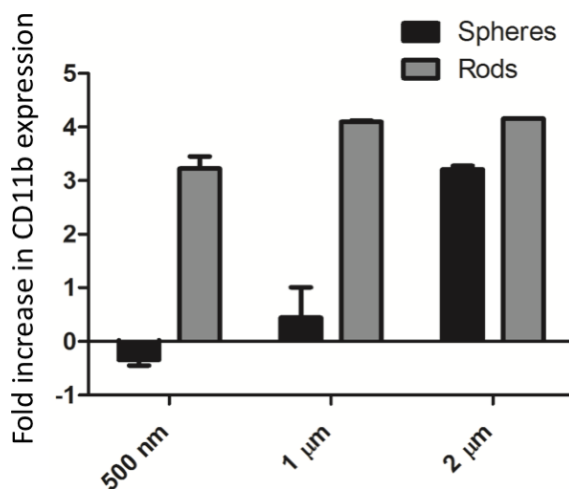
Figure 3.4. The fold-change in the level of CD11b expression by human neutrophils relative to untreated cells after being incubated with spheres and AR6 of different sizes in whole blood for 2 h. The particle concertation in blood was set at 10^7 particle/ml for microparticles and at 10^8 particles/ml for 500 nm particles.
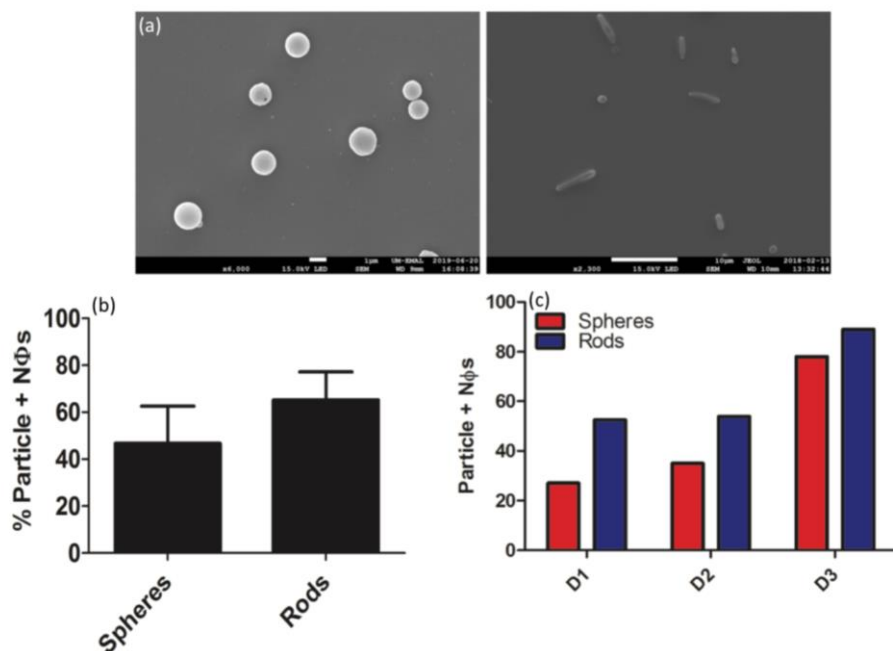
Figure 3.5. (a) SEM image of Cy5.5-loaded PLGA spheres and AR6 rods with the equivalent spherical diameter of 1.5-μm fabricated via the two-step emulsion solvent evaporation technique. (b) Effect of shape on the uptake of PLGA microparticles by primary human neutrophils. The concentration of particles in blood was set at 5×10^6 particles/ml. Unpaired t-test was used to analyze figure 3.5b. (c) Uptake of the PLGA rods and spheres by primary human neutrophils separated for individual donors.

to untreated cells while the change was minimal for spheres. For 1 μm and 2 μm particles, this number was increased to 4-folds for rods while respectively being at only 0.5 and 3 folds for spheres (Figure 3.4). These results confirm the data presented in Figure 3.3, and the preferential phagocytosis of elongated particles compared to spheres of the same volume.
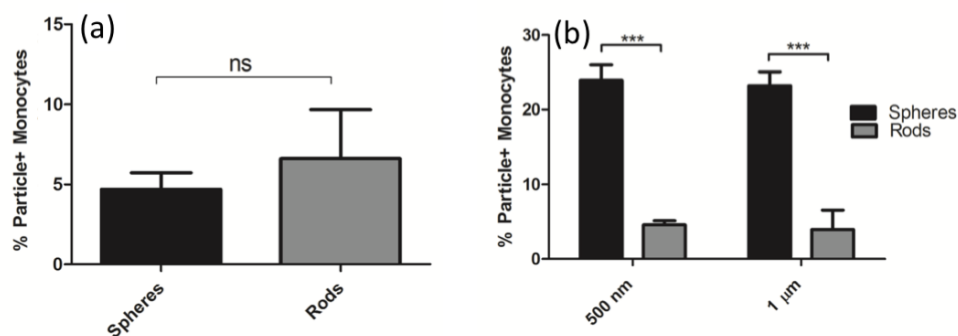
Figure 3.6. *Ex vivo* uptake of polystyrene spheres and AR6 rods by (a) isolated human monocytes in plasma, and (b) THP-1 monocytes. The concentration of cells and particles were respectively set at 10^6 and 10^7 particles/ml. Unpaired t-test was used to analyze Fig. 3.5.a and Two-way ANOVA with Bonferroni post-tests was used for analyzing Fig. 3.5b (ns: P>0.05, *: P<0.05, **: P< 0.01, ***: P<0.001).
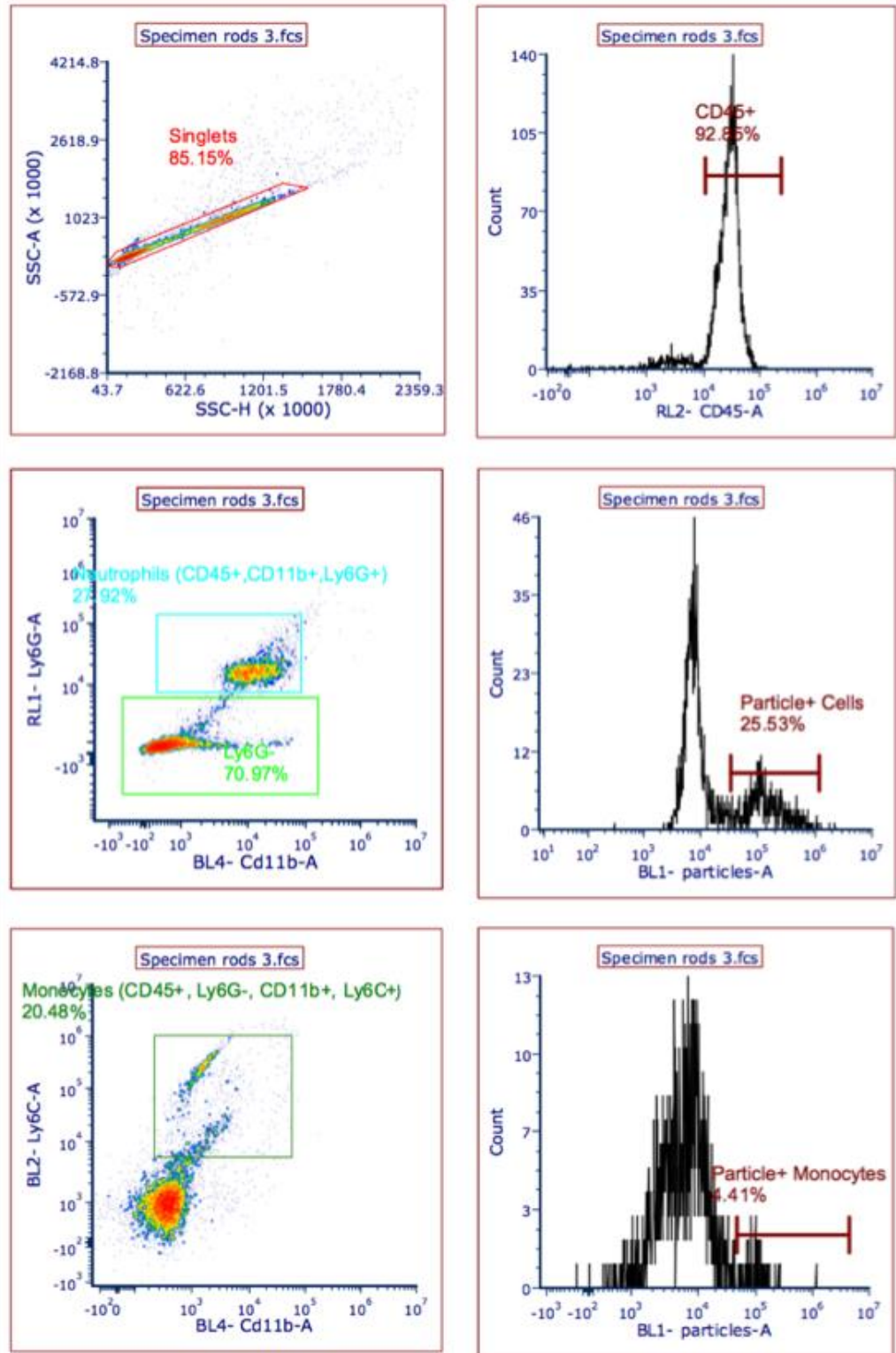
Figure 3.7. Representative flow-cytometry panels for gating mouse neutrophils and monocytes. After gating the singlets, neutrophils can be identified as CD45+, CD11b+, and Ly6G+ cells and monocytes can be identified as CD45+, Ly6G-, CD11b+, and Ly6C+ cells. Particle+ cells are identified as the population of the cells which are positive for the FITC signal.

To see if the observed increased uptake of rods by neutrophils is valid for other materials, we investigated the uptake of PLGA rods and spheres by primary human neutrophils. Fluorescent (Cy5.5-loaded) spherical and rod-shaped PLGA particles of 1.5 μm ESD were fabricated via a two-step emulsion solvent evaporation technique (Figure 3.5a), as described in detail in the next chapter.[79] As with polystyrene particles, PLGA rods were taken up by primary human neutrophils at a ~20% higher rate than that of equivalent PLGA spheres (Figure 3.5b). However, the differences between rods and spheres were not significant for PLGA particles due to variation in the uptake levels for individual donors and, likely, the heterogeneity in the PLGA particle size within a given sample. Nevertheless, rods were consistently internalized more than spheres for each individual donor, and on average, PLGA rods have a $54 \pm 23\%$ higher uptake than spheres (Figure 3.5c). Next, we examined the uptake of particles of different shapes by monocytes and monocyte-derived cell lines. First, we evaluated isolated primary human monocytes in plasma. Isolated monocytes were used in this study due to the low population of human monocytes in whole blood compared to neutrophils and lack of a specific monocyte marker. As represented in Figure. 4.6a, the isolated human monocytes' uptake of rods was not significantly different from that of spheres. Conversely, for assays with cultured THP-1 monocytes, we find rods exhibited 5 and 6-fold <u>lower</u> uptake than spherical particles of the same volume for the ESD of 500 nm and 1 μm, respectively, which is opposite of the trend observed for neutrophils (Figure 3.6b).

To determine if the observed trend for human neutrophils is species-dependent, we investigated the uptake of AR6 rods and spheres of different sizes by normal and inflamed mouse blood. AR6 rods were used in these experiments due to their consistently higher uptake by primary human neutrophils compared to the spheres across all the size ranges (Figure 3.3a-c). Neutrophils in mouse blood were identified by gating out CD45, CD11b, and Ly6G positive cells. Particle positive cells were quantified by gating the population of the FITC positive cells (Figure 3.7).
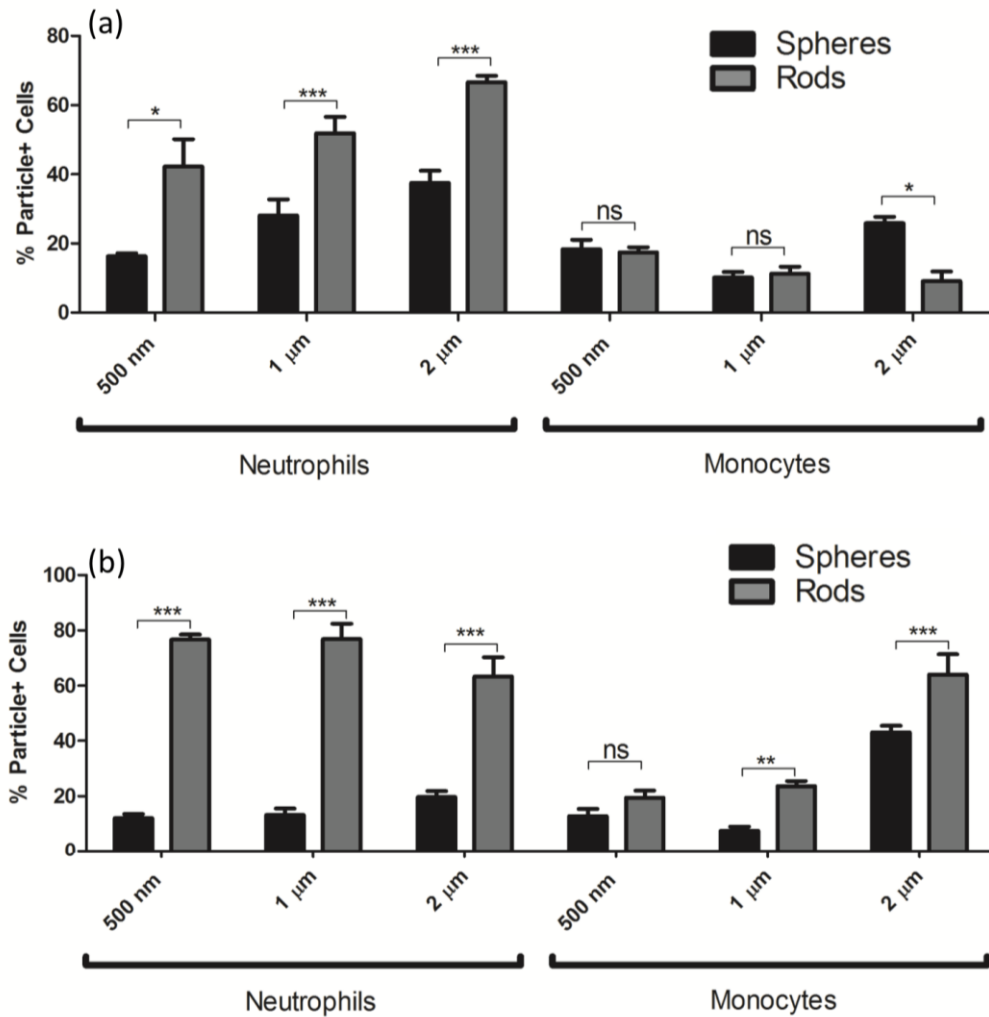
Figure 3.8. *Ex vivo u*ptake of polystyrene spheres and AR6 rods of different sizes by (a) BALB/c, (b) EAE model of SJL/J mouse neutrophils and monocytes in whole blood. The concentration of particles in blood was set at 10^7 particles/ml. Two-way ANOVA with Bonferroni post-test was used for analyzing the data (ns: $P>0.05$, *: $P<0.05$, **: $P< 0.01$, ***: $P<0.001$).

Figure 3.8 shows that independent of the mouse strains evaluated, rods of all different sizes had a significantly higher uptake by neutrophils compared to spheres. In the BALB/c mouse blood, 500 nm, 1 μm, and 2 μm AR 6 rods had an approximately 1.5-fold higher uptake than spheres (Figure 3.8a). The same trend was observed for the experimental autoimmune encephalomyelitis, EAE, model of the SJL/J mouse strain. Due to the saturation of the EAE mice neutrophils by 2-micron particles at the two-hour uptake point, the 30-min uptake time point was investigated. At the 30-min time point, EAE neutrophils in blood internalized rods with ESD of 500 nm, 1 μm, and 2 μm at 7, 7.5, 4-fold higher than spheres of the same volume, respectively, which is consistent with the trend observed for the BALB/c mice and human neutrophils (Figure 3.8b). Again, in contrast to neutrophils, BALB/c mouse monocytes phagocytosed rods at the same or lower level than spheres of the same volume (Figure 3.8a). When we compare the uptake of particles by neutrophils and monocytes for BALB/c mice, we find that rods had 2.5, 4.5, and 7-fold higher association with neutrophils compared to monocytes for 500 nm, 1 μm, and 2 μm particles, respectively. In the EAE model, monocytes were found to internalize rods higher than spheres, similar to neutrophils (Figure 3.8b). However, a head-to-head comparison between EAE mouse neutrophils and monocytes show that neutrophils internalized rods by ~3.5-fold more than monocytes for the 500 nm and 1 μm particles. For 2 μm particles in EAE mouse blood, however, rods were internalized at the same level by both monocytes and neutrophils. These results demonstrate that the rod shape, coupled with size, can be used to target neutrophils in circulation selectively while keeping the respective uptake by monocytes minimum.

3.4.2. Shape dependence of uptake of polymeric particles by blood leukocytes in vivo

To confirm the observed *in vitro* trends described above exist *in vivo*, we investigated the uptake of particles by leukocytes in BALB/c mice injected with either a 500 nm polystyrene spheres or AR6 rods *in vivo*. The 500 nm particles and AR6 rods were chosen for the *in vivo* assays due to the maximum difference between the association of rods and spheres with neutrophils that was observed for this size in *in vitro* assays, as represented in Figure 3.3c. Additionally, there is more interest in the utilization of smaller sized particles in clinical trials due to the lower risk of inducing occlusion in smaller capillaries. After particle injections, blood was drawn from the animals via cardiac puncture 30 minutes post-injection and the association of particles with monocytes and neutrophils evaluated via flow cytometry. The *in vivo* results confirmed the observed *ex vivo* trend. While there was not a significant difference between the uptake of rods and spheres by monocytes, neutrophils preferentially phagocytosed rods compared to spheres. Specifically, rods had 3-fold higher uptake than spheres of the same volume by mouse neutrophils *in vivo* (Figure 3.9).
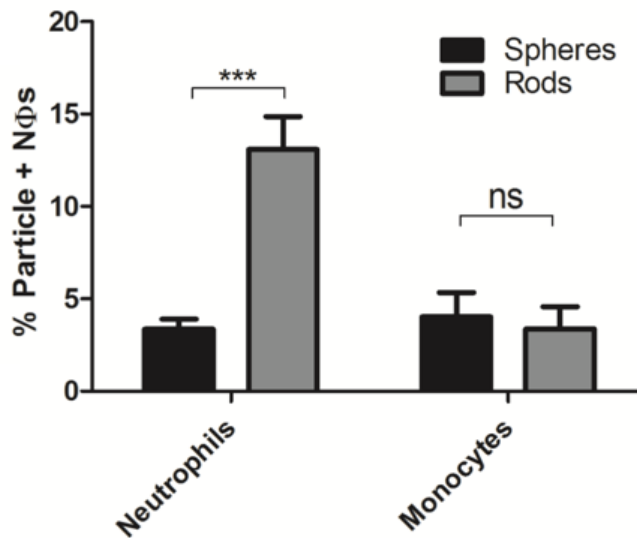
Figure 3.9. *In vivo* uptake of the 500 nm polystyrene spheres and AR6 rods of the same volume by mouse neutrophils and monocytes. 1.5×10^9 particles (either rods or spheres) were injected into each animal and the blood was drawn from the animals 30 minutes post-injection. Two-way ANOVA with Bonferroni post-test was used for analyzing the data (ns: P>0.05, ***: P<0.001).

3.4.3. *Competitive uptake of rods and spheres by neutrophils*

Competitive uptake assays conducted with 2 μm rods and spheres also confirmed the preferential uptake of rods by human and mouse neutrophils, i.e., spheres and rods were simultaneously present in the sample at the same concentration. The AR6 rods were associated with human neutrophils about 3-fold higher than spheres of the same volume despite both particle shapes being simultaneously available for cell eating (Figure 3.10a). Further analysis revealed that less than 10% of human neutrophils internalize only spheres, while approximately 35% of them were associated with rods only. About 15% of human neutrophils internalized both rods and spheres simultaneously (Figure 3.10b). The same trend was observed for mouse neutrophils, where there were around 3.5-fold higher number of the neutrophils associated with rods compared with spheres (Figure 3.10c). Additionally, only about 5% of mouse neutrophils internalized only spheres, while ~55% of cells only phagocytosed rods. About 15% of mouse neutrophils internalized both rods and spheres (Figure 3.10d). The increased association of neutrophils with rods in the competitive uptake assays was also confirmed via microscopy. As shown in Figure 3.9e, a higher number of rods were colocalized with human neutrophils compared to spheres. Quantification of the number of particles associated with cells in multiple images showed that about 85% of spheres were free in the mixture without being internalized by any cells. This number decreased to 60% for the rods, which confirms the preferential association of the rods with neutrophils. To summarize, results here demonstrate that the preference of neutrophils for internalizing rods remains valid even with both the rods and the spheres present in the same sample.

Figure 3.10. Competitive uptake of 2 μm spheres and AR6 rods by primary human and mouse neutrophils. The total population of human neutrophils which were (a) rod-positive or sphere-positive and (b) internalized only rods, spheres, or both rods and spheres. (c) The total population of mouse neutrophils which were rod-positive or sphere-positive or (d) internalized only rods, spheres, or both the rods and the spheres. (e) The fluorescent image representing the competitive uptake of rods and spheres by human neutrophils. The cells are red and the particles are green. One-way ANOVA with Tukey's post-test was used to analyze figures 3.10b and 3.10d, and unpaired t-test was used to analyze figures 3.10a and 3.10c (ns: $P > 0.05$, *: $P < 0.05$, **: $P < 0.01$, ***: $P < 0.001$).

3.4.4. Preferential uptake of rods is unique to neutrophils

The results presented in previous sections demonstrating the preferential uptake of rods by blood neutrophils, is unexpected and counter to the general understanding to date of the impact of shape on particle phagocytosis and blood circulation *in vivo*. Several published studies have demonstrated that rods are phagocytosed by macrophages significantly less than their spherical counterparts,[23] which this observations were often projected to all leukocytes. To confirm the unique observation of neutrophil's preference for rods is not an artifact of our system, we investigated the uptake of particles of different shapes by cells evaluated in prior publications, i.e., mouse and rat macrophages and dendritic cells.

Similar to prior publications, bone marrow-derived macrophages evaluated in our system preferentially phagocytosed spheres. Spheres were taken up 6 and 5-fold higher than AR6 rods of the same volume respectively for particles with ESD of 500 nm and 1 µm (Figure 3.11a). Similarly, rat alveolar macrophages also exhibited 3 and 5-fold higher uptake of spheres than AR6 rods for particles with ESD of 500 nm and 1 µm (Figure 3.11b), respectively. Due to the minimal uptake of 500 nm particles by the rat alveolar macrophages when their concentration was matched to microparticles, the uptake was not significantly different between rods and spheres for this size. When the concentration of 500 nm particles was increased to 10^8 particles/mL and the concentration of cells lowered to 10^6 cells/mL, the difference between rods and spheres became significant for 500 nm particles as well. Spheres of this nanometer size had 16-fold higher uptake by alveolar macrophages than the rods of the same volume (Figure 3.11c). Our results demonstrated that macrophages followed the same general observed trend of the preferential uptake of spheres reported in previous works, showing that phagocytosis of microparticles by macrophages can be inhibited by using elongated particles.

The same trend of inhibited phagocytosis of rods was also observed for dendritic cells. When the concentration of particles was fixed at 10^7 particles/mL, which is two times higher than the cell concentration, 500 nm and 1 μm spheres had 2.5 and 4-fold higher uptake than the rods of the same volume, respectively (Figure 3.11d), but the difference was not significant for the 500 nm ESD. At the higher concentration of 10^8 particles/ml, the difference between the uptake of 500 nm rods and spheres was shown to be significant, with spheres exhibiting 7-fold higher uptake than the rods of the same volume (Figure 3.11e). To summarize, our results in this section show that both macrophages and dendritic cells favorably phagocytosed spheres compared to the high aspect ratio particles, following the same trend as monocytes.
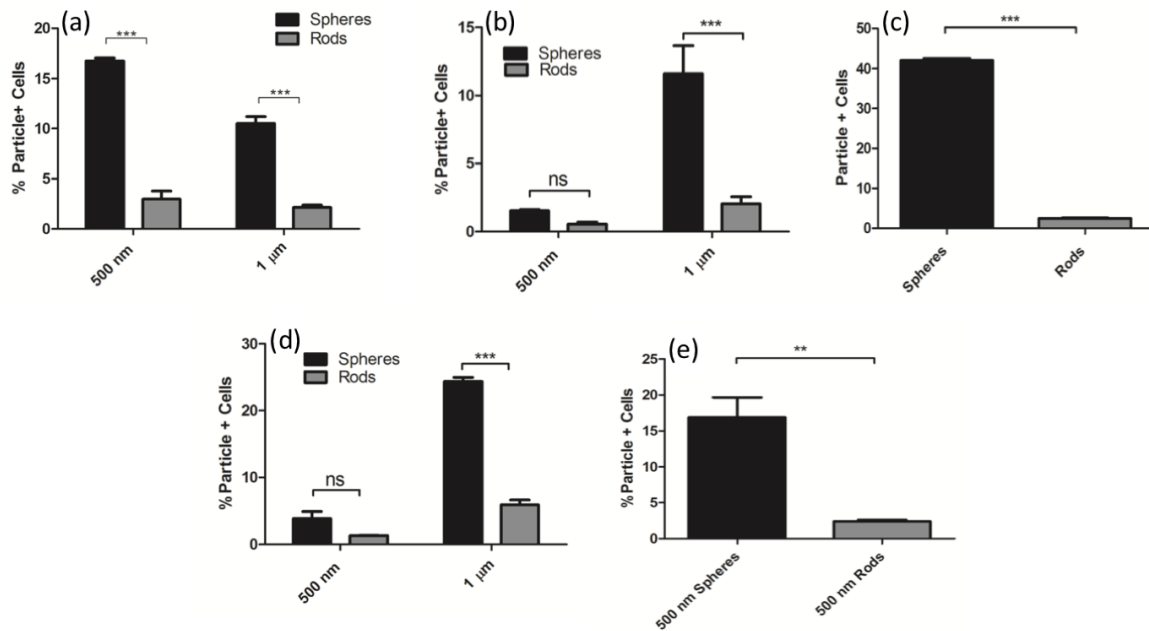
Figure 3.11. The shape-dependence of the phagocytosis of polymeric particles by macrophages and dendritic cells. Uptake of the spherical and AR6 rod-shaped polystyrene particles of different sizes by (a) mouse bone marrow-derived macrophages and (b) rat alveolar macrophages in RPMI media. The concentration of particles was fixed at 10^7 particles/ml, and the concentration of cells was set at 5×10^6 and 10^7 cells/ml respectively for mouse bone marrow-derived and rat alveolar macrophages. (c) Uptake of 500 nm spherical and AR6 rod-shaped polystyrene particles by rat alveolar macrophages when the concentration of cells and particles was respectively set at 10^6 cells/ml and 10^8 particles/ml. Uptake of rods and spheres of different sizes by mouse bone marrow-derived dendritic cells with the fixed particle concentration of (d) 10^7 particles/ml and (e) 10^8 particles/ml. The concentration of cells was fixed at 5×10^6 cells/ml. Two-way ANOVA with Bonferroni post-test was used for analyzing figures a, b, and d and unpaired t-test was used for analyzing figure c and e (ns: P>0.05, *: P<0.05, **: P< 0.01, ***: P<0.001).

3.5. Discussion

Our results in this paper have demonstrated that, contrary to the trend observed for mononuclear phagocytes, neutrophils preferentially phagocytose rod-shaped particles. Increasing the aspect ratio of particles increases their association with and uptake by human and mouse neutrophils. The observed trend remains valid when the competitive uptake of rods and spheres were investigated as well, where neutrophils were favorably associated with the rods compared to the spheres. In whole blood samples, when both neutrophils and monocytes were present, the neutrophils significantly favored the rods compared to monocytes.

The previously reported reduced internalization of ellipsoidal particles by macrophages was attributed to the energy requirement for actin-remodeling necessary for engulfment of the high aspect ratio particles.[59] Rods have been reported to have increased attachment to macrophages, but the energy required for the actin remodeling limits their internalization and phagocytosis rate.[59] The observed differences between the response of the neutrophils and MNP phagocyte groups might be attributed to the differences in their phagocytic mechanisms. Neutrophils generally have higher mobility than the other phagocytes, including both monocytes and macrophages.[96] It has also been shown that when engulfing untargeted microparticles, the cellular pedestal of the neutrophils goes through protrusion in the direction of the target in the initial phases of phagocytosis, which shows their capability for remodeling their actin network during phagocytosis.[105,106] The amount of cortical tension and viscosity is reported to be an order of magnitude higher for macrophages compared to neutrophils. All these mentioned studies imply higher stiffness and lower surface motility for macrophages compared to neutrophils.[107] Furthermore, it is reported that in contrast to macrophages, phosphorylation of the FcγR receptors is not essential for the phagocytic activity of neutrophils.[108] Thus, the increased motility of the

neutrophils compared to MNP phagocytes and the unnecessity of phosphorylation during phagocytosis likely translate to their lower energy barrier for actin remodeling and engulfment of the elongated particles compared to other phagocyte groups.

Furthermore, phagocytosis is a two-step process consisting of the attachment and internalization of the particles.[24] The lower energy barrier for the actin remodeling can change the rate-limiting step in the phagocytosis process for neutrophils. Once this energy barrier for the actin remodeling is overcome, the extent of the phagocytosis can be a consequence of the interplay between the attachment rate, particle volume, and major axis size. As our results show, for the size range studied in our work, increasing the size of particles increases their uptake by neutrophils for the matched concentration of the particles in the blood, which is in-line with the results of the previous studies that have investigated the impact of size on phagocytosis of particles by primary human neutrophils.[41,100] The previously reported higher attachment of rods to the phagocytes,[59] and the increase in the major axis length by increasing the aspect ratio of the particles may then explain the observed higher internalization of particles by neutrophils. However, it should be noted that the major axis length is not the sole determining factor of the phagocytosis by neutrophils. The AR6 500 nm rods and AR2 1 μm rods both have the same major axis length, but the uptake of the 500 nm rods is significantly lower than the 1 μm rods for the matched concentration, possibly due to their smaller volume.

As discussed previously, targeting the neutrophils in different inflammatory conditions is a potential strategy for controlling the disease and its progression.[15,94,95] The results of this study show the specificity of rods to neutrophils, even in inflammatory conditions like EAE, for particle sizes of 1 μm or smaller. Previous works have also demonstrated that optimization of the particle design parameters, like hydrophobicity, to maximize their association with neutrophils will

51

increase their therapeutic benefit as inflammation modulators.[15,95] We posit that this observed desirability of rods to get associated by neutrophils can be used to specifically target neutrophils in disease models where neutrophils are the key player while benefiting from their reported prolonged circulation times and minimum uptake by other phagocytes to increase their therapeutic efficacy.

3.6. Conclusions

In conclusion, our work has, for the first time, investigated the response of neutrophils to variations particle shape. This feature can be used to target neutrophils to reduce their trafficking to inflammation sites, or to deliver a specific drug to these cells. In future work, we will use our rod-shaped particles in various disease models where neutrophils are the key targets to see if the utilization of the elongated particles, which benefit from increased association with neutrophils, can help to improve the treatment status of these conditions. We will also work to further our understanding of the underlying mechanism for the different responses of different phagocyte groups to shape.

CHAPTER 4: Modified Two-step Emulsion Solvent Evaporation Technique for Fabricating Biodegradable Rod-shaped Particles in the Submicron Range

4.1. Publication Information

4.2. Abstract

Though the emulsion solvent evaporation (ESE) technique has been previously modified to produce rod-shaped particles, it cannot generate small-sized rods for drug delivery applications due to the inherent coupling and contradicting requirements for the formation versus stretching of droplets. The separation of the droplet formation from the stretching step should enable the creation of submicron droplets that are then stretched in the second stage by manipulation of the system viscosity along with the surface-active molecule and oil-phase solvent. A two-step ESE protocol is evaluated where oil droplets are formed at low viscosity, followed by a step increase in the aqueous phase viscosity to stretch droplets. Different surface-active molecules and oil phase solvents were evaluated to optimize the yield of biodegradable PLGA rods. Rods were assessed for vascular-targeted delivery applications via blood flow adhesion assays. The two-step ESE method generated PLGA rods with major and minor axis down to 3.2 μm and 700 nm, respectively.

Chloroform and sodium metaphosphate were the optimal solvent and surface-active molecule, respectively, for submicron rod fabrication. Rods successfully targeted an inflamed endothelium under shear flow in vitro and in vivo.

4.3. Introduction

The current methods for the fabrication of non-spherical drug carriers include heat-stretching of spheres, template-based molding, and microfluidic techniques.[109–114] However, non-spherical particles formed via the heat-stretching of drug-loaded spherical particles would likely suffer from drug degradation and leaching.[109,110] Similarly, template-based methods that give accurate control over particle geometry often require expensive and complicated setup, leading to scale-up issues.[111] Microfluidic techniques that precisely shape liquid droplets to make particles of different geometries with high control over particle size also need complicated setups that cannot easily convert to large-scale production.[112,113] An electrohydrodynamic jetting method has also been described where polymeric rods are achieved via co-spinning liquid jets into bundles followed by the cutting of the microfiber bundles into the desired size.[114] Despite having the capability of making multicompartmental particles, this approach requires complex and specialized instrumentation, and the extensive sonication used in washing steps can leach out the therapeutic loading. Thus, a need remains for a simple, inexpensive, and highly scalable technique for fabricating rod-shaped biodegradable particles.

As stated in the introduction chapter, the emulsion solvent evaporation (ESE) technique is a simple and scalable technique widely used for the fabrication of spherical drug carriers.[114] Our lab has previously demonstrated that this method could be modified to fabricate rod-shaped particles with high throughput, where rods are achieved by stretching the emulsion droplets

through the application of shear stress in a system with low interfacial tension.[78] However, previous studies with the ESE method have been limited to rods with major axes above 10 μm or minor axes in the micrometer range.[78,115–117] A long major axis for rods may impose the risk of occlusion in small human capillaries when used in clinical application. Thus, there remains an interest in the development of methods that can produce smaller, biodegradable rods in a high-throughput manner for use in clinical drug delivery applications. Previous attempts to obtain smaller rod sizes with the standard ESE method have not been successful; the droplets are either not capable of being stretched or have resulted in other shapes, e.g., rhombus shape with unsmooth surface morphologies.[78,115] Two dimensionless numbers control droplet deformation during the oil-water emulsification in the ESE. First, the capillary number described in Equation 4.1, where γ is the shear rate, η_S is the water phase viscosity, a is the droplet radius, and Γ is the interfacial tension between the oil phase and the water phase,[118] and second, the viscosity ratio of the water phase to oil phase.[78] Lowering viscosity ratio and increasing Ca results in better droplet deformation. Thus, the smaller droplet size needed to achieve smaller rods would decrease Ca, making droplet stretching impossible even for high viscosity values.

$$Ca = \frac{\gamma \eta_s a}{\Gamma} \text{ (Equation 4.1)}$$

In this chapter, we developed a two-step fabrication method to reduce the size of the ellipsoidal particles fabricated by the ESE while maintaining the scalability and high yield characteristics of the technique. Small-sized droplets are formed in the first step, followed by a step-change in the viscosity of the fabrication system to enable the stretching of small droplets into rod particles in the second stage. With the optimization of the two-step process, we were able to fabricate biodegradable, PLGA, rods with major and minor axes size as small as 3.2 μm and 700

nm, respectively. Furthermore, the particles were successfully loaded with Nile Red fluorescent dye, confirming the capability for loading therapeutics into submicron rods fabricated via the modified, two-step ESE technique. Importantly, this simple, bottom-up fabrication technique produces polymeric rods in size range viable for *in vivo* targeted drug delivery applications, which we demonstrated rods fitted with antibodies on their surfaces were able to bind to inflamed vascular in a microfluidic model of human blood flows and *in vivo* in mice.

4.4. Results

4.4.1. Effect of droplet size on the yield of ESE technique

The ESE method typically consists of the polymer of choice, PLGA, dissolved in an organic solvent, which is emulsified into an aqueous phase that consists of surfactant and, in some cases, a surface-active molecule. In this work, the baseline ESE process composed of an oil phase having 1.8 mg/ml PLGA polymer dissolved in chloroform and an aqueous phase containing PVA (1%) as the surfactant and sodium tripolyphosphate (2.0%) as the surface-active molecule. The dimension of the rods obtained from the ESE method is set by the size of the initial oil droplet formed at the start of the oil-water emulsification. As such, the desired goal of achieving smaller rod dimensions requires altering the ESE process to produce smaller sized droplets. Previous reports have shown that increasing the surfactant concentration, lowering polymer concentration in the oil phase, and increasing the shear rate/ mixing speed all yield smaller droplet size in the ESE method.[78] Indeed, increasing the shear rate for the emulsion in our system from 2500 to 5500 at fixed oil and water phase conditions resulted in smaller-sized particles, as shown in Figure 4.1a. However, as anticipated, the increase in stirring speed resulted in a decrease in the yield of rods, defined by the ratio of the particles with an aspect ratio of two or higher to the total number of the particles, from 66% to 8% (Figure 4.1b).
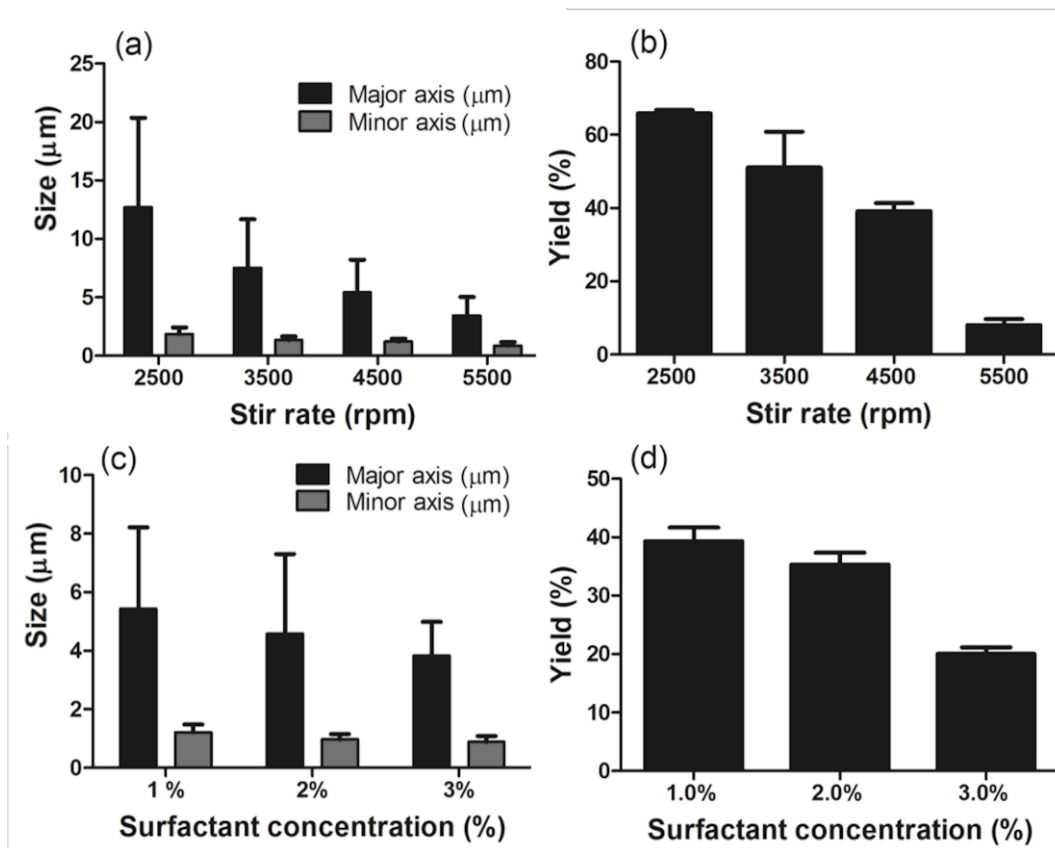
Figure 4.1. Rod fabrication (a) size and (b) yield as a function of stir rate in ESE technique (PVA concentration is fixed at 1.0%). Rod fabrication (c) size and (d) yield as a function of surfactant (PVA) concentration in the water phase (stir rate is fixed at 4500 rpm). For all trials, the oil phase consisted of 1.8 mg/ml of PLGA in chloroform and the water phase includes 2.0% sodium tripolyphosphate.

Another way to generate small droplet size is by increasing the viscosity of the system, which can be achieved by increasing the surfactant, PVA, concentration in the oil phase. Figures 4.1c and 4.1d demonstrate the size and yield of rods fabricated with increasing concentration of PVA in the water phase at a fixed stir rate of 4500 rpm. All other process conditions are as for the data presented in Figure 4.1a and b. As expected, an increase in the surfactant concentration from 1.0 to 3.0% decreased the major axis size from 5.5 to 4.0 μm, but the rod fabrication yield dropped from 40% to 20%. Thus, our results show that the conventional emulsion solvent evaporation technique needs to be modified to allow the fabrication of rod particles in the submicron size range required for drug delivery.

4.4.2. Modified two-step solvent evaporation fabrication technique

Due to the difficulty of stretching smaller sized emulsion droplets by the simple, one-step ESE technique, we sought to modify this method to fabricate smaller-sized rods. Thus, we developed a two-step fabrication method, where the droplet formation and elongation step are temporally separated from each other. In the first step, the droplets are formed, and the size fixed with a low surfactant concentration corresponding to lower aqueous phase viscosity. Next, a solution with a higher surfactant concentration is added to the aqueous phase to create a step increase in the viscosity of the water phase. We compared the fabrication yield between the one- and two-step method for different concentrations of PVA (surfactant) used in the second step at a fixed stir rate of 5500 rpm and with the baseline condition used for the oil phase and surface-active
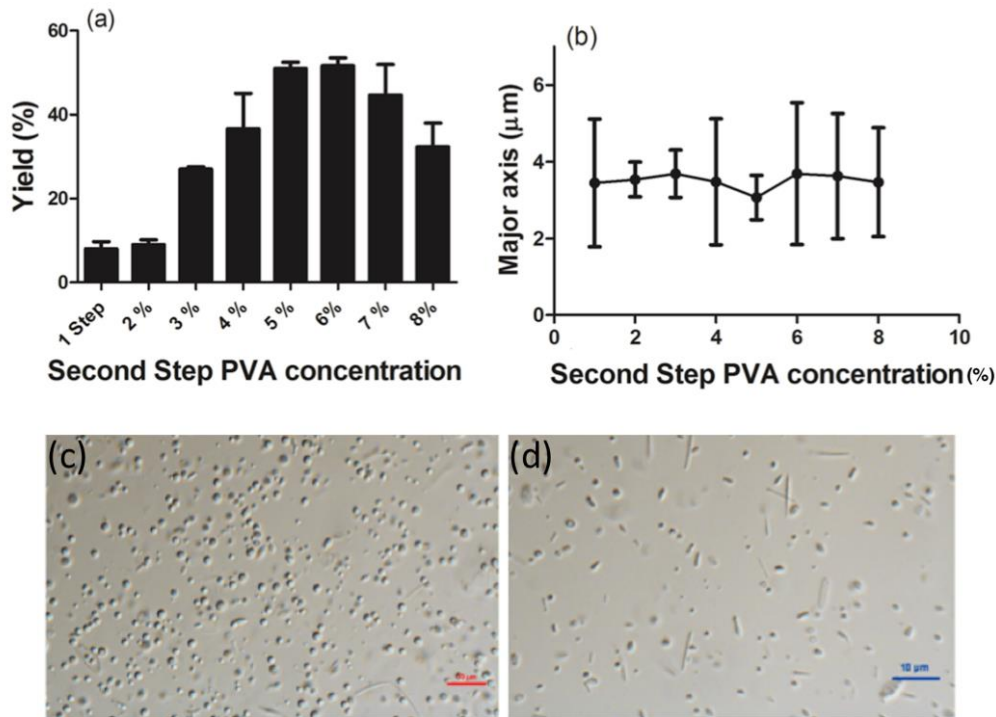
Figure 4.2. Comparison of the (a) yield and (b) size for one- and two-step fabrications with different second step surfactant concentrations. The first step PVA concentration and stir rate are fixed at 1.0% and 5500 rpm. 1.8 mg/ml PLGA in chloroform and 2.0% sodium tripolyphosphate are used as the oil phase and surface-active molecule. The bright field images demonstrating the yield difference for (c) one step and (d) two-step fabrications with 6.0% PVA as the second step surfactant concertation. Scale bars are 10 μm, the first step PVA concentration and stir rate are fixed at 1.0% and 5500 rpm while 1.8 mg/ml PLGA in chloroform and 2.0% sodium tripolyphosphate are used as the oil phase and surface-active molecule.

58

molecule. Figure 4.2a shows the percent rod formed as the PVA concentration in the water phase of the second step is set at 2% or higher for a fixed first step PVA concentration of 1.0%. Our results demonstrated a significant increase in the rod yield for the two-step fabrication system when the PVA concentration of the second step water phase is set at 3% or higher (Figure 4.2a). The maximum rod yield of 55% was observed at the second-step PVA concentration of 6.0%, which represents a 5-fold increase in the yield compared to the one-step process (Figure 4.2a-d). Figure 4.2b shows that the size and the aspect ratio of the rods produced did not change with the change in the second step PVA concentration, verifying the hypothesis that the droplet size is fixed in the first step of the two-step process. Indeed, other works have characterized droplet formation in the ESE and reported that the droplet size stabilizes after a specific time point, and no further change in the size of the particles is observed with continued shear.[119,120] Our results demonstrated that the maximum stretching yield is obtained when the second step PVA concentration is introduced 15-30 minutes after starting the emulsification. This shows that we need to induce the viscosity shock when enough solvent has evaporated for the droplets to be stabilized but before they are solidified.
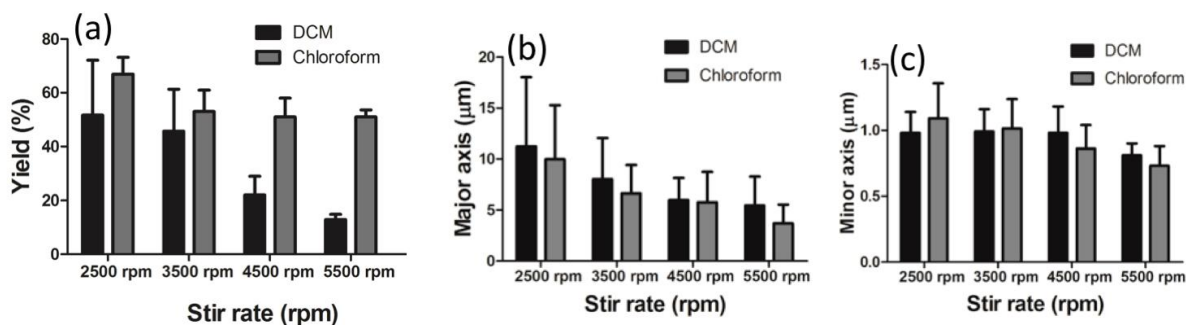
Figure 4.3. (a) Fabrication yield, (b) Major axis, and (c) minor axis size as a function of the choice of oil phase solvent choice (2.0% sodium tripolyphosphate is used as the surface-active molecule, first and second step PVA concentrations are fixed at 1.0% and 6.0%, and PLGA concentration in the oil phase is fixed at 1.8 mg/ml).

59

4.4.3. Effect of the oil phase solvent

Next, we sort to improve the ellipsoid yield for the two-step fabrication process by optimization of the material choice and fabrication system. The oil phase evaporation rate and the ratio of the oil to water phase viscosity are two parameters that contribute to the degree of stretching possible for emulsion droplets.[78] Thus, the choice of the oil phase solvent is critical to the fabrication yield. In the results presented thus far, chloroform was the solvent of choice for the oil phase. However, Dichloromethane (DCM) is another solvent used with the ESE method in a majority of previously published studies. Thus, we explored using DCM as the oil phase solvent in our two-step method. The second step PVA concentration of 6.0% that produced the maximum rod yield with chloroform was used for this comparison (with surface-active molecule = 2.0% Sodium tripolyphosphate and first step PVA concentration = 1.0%). Across all the stirring speeds explored, the use of DCM as the oil phase solvent resulted in a lower particle yield compared to the yield obtained with chloroform (Figure 4.3a), with the difference being more significant for higher stir rates, i.e., smaller droplets. Specifically, having DCM as the oil phase solvent resulted in between 7 and 38% decrease in the average fabrication yield relative to chloroform. Interestingly, the size of rods, i.e., droplet size, remained the same between DCM and chloroform
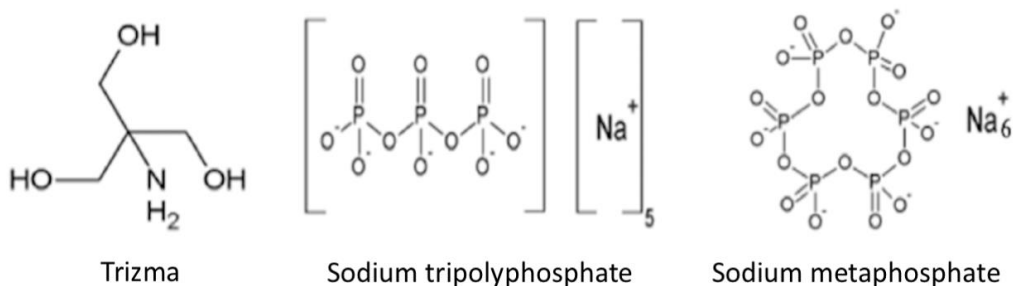
Figure 4.4. Chemical structure of different surface-active molecules used in the two-step fabrication method.

for all the shear rates used (Figures 4.3b and 4.3c). As a result, chloroform was picked as the solvent for the rod fabrication.

4.4.4. *Effect of the surface-active molecule on rod production*

The presence of a surface-active molecule enables droplet deformation via the interaction of the hydrophilic groups between the surface-active molecule and the polymer, which will lead to lower interfacial tension and hence increase in Ca. The surface-active molecule making the strongest interaction with PLGA polymer is predicted to lead to the lowest interfacial tension and,
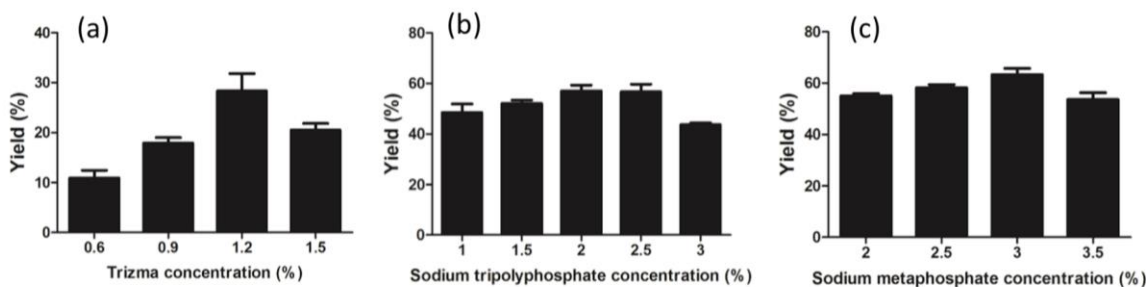
Figure 4.5. The fabrication yield as a function of concentration of surface-active molecule of (a) Trizma (b) sodium tripolyphosphate and (c) sodium metaphosphate in the water phase. (1.8 mg/ml PLGA in chloroform is used as the oil phase solvent and the first step and second step PVA concentration is fixed at 1.0% and 6.0).

thus, the highest rod fabrication yield. Trizma base and sodium tripolyphosphate have been previously used in individual studies for PLGA rod fabrication.[78,117] However, different surface-active molecules have yet to be compared head-to-head in the same system to determine the properties that make the surface-active molecule favorable for use with a specific polymer choice. Here, we compared three different surface-active molecules: Trizma base, sodium tripolyphosphate (NaTP), and sodium metaphosphate (NaMP) (Figure 4.4). Sodium metaphosphate was chosen as the third molecule for its similar structure to NaTP and its higher number of negatively charged oxygens per molecule, which we hypothesize would result in a stronger interaction with PLGA. To start, we determined the optimum concentration for each

61

surface-active molecule that results in the highest fabrication yield in the two-step ESE fabrication technique.

The optimum concentrations were found to be 1.2% for Trizma base (Figure 4.5a), 2.0% for NaTP (Figure 4.5b) and 3.0% for NaMP (Figure 4.5c). The performance of the three surface-active molecules was then compared in the two-step fabrication at their optimum concentration. The results displayed in Figure 4.6a demonstrates that the spheroid yield increased with the change in the surface-active molecule from Trizma to NaTP to NaMP for most stir rates evaluated and with all other process conditions fixed at baseline. Again, the size of the particles did not significantly change with the different surface-active molecules (Figure 4.6b-c). Changing from NaTP to NaMP resulted in between 10 and 32% increase in the fabrication yield for the different shear rates, while the use of the Trizma base resulted in a 5–28% decrease in the rod yield relative to NaTP. The difference in the yields across different surface-active molecules is more pronounced at the higher shear rates, which again is likely due to the smaller size of the droplets at high shear rates that make the stretching process harder for the droplets – hence a more favorable interfacial interaction is needed. At low shear rates, the droplets are large enough to be readily stretched regardless of the surface-active molecule used.

To summarize, NaMP was found to be the best performing surface-active molecule among the three choices to lower the interfacial tension of the fabrication system to achieve the highest possible yield of rods.
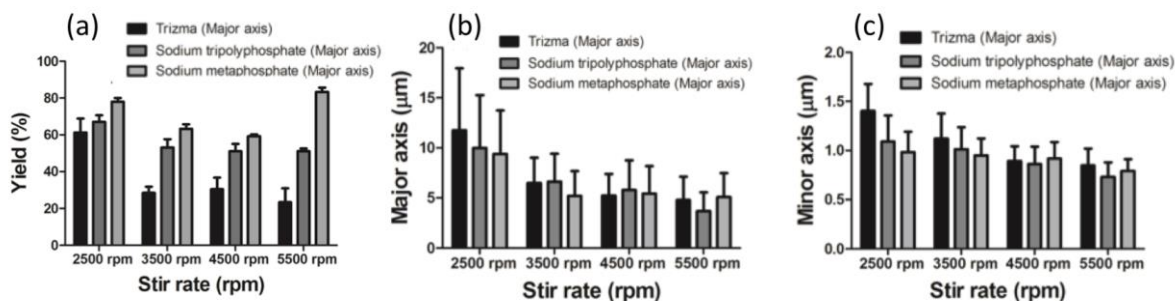
Figure 4.6. (a) The fabrication yield, (b) major axis, and (c) minor axis size as a function of the choice of the surface-active molecule at optimum concentration. (1.8 mg/ml PLGA in chloroform is used as the oil phase solvent and the first step and second step PVA concentration is fixed at 1.0% and 6.0).

4.4.5. Fabrication of ellipsoids with controlled size and high yield

After systematically optimizing the solvent and surface-active molecule for the two-step fabrication, we fabricated rods of different sizes by varying the polymer concentration in the oil phase. Rods were fabricated in the presence of chloroform as the oil phase solvent and 3.0% NaMP
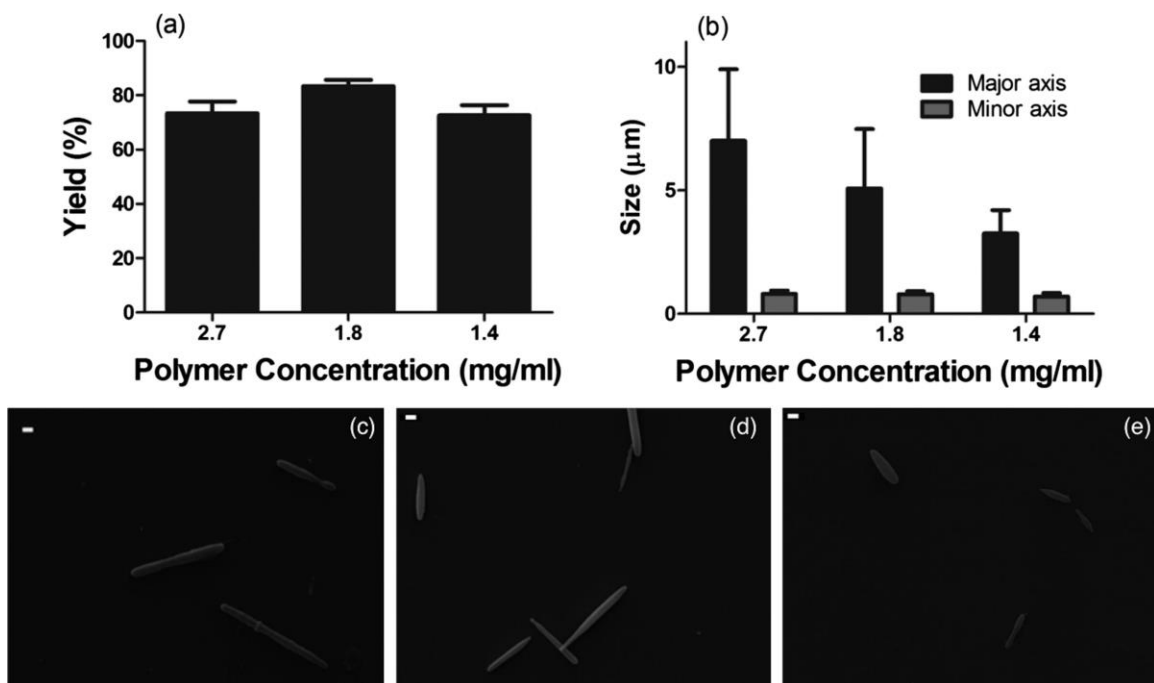
Figure 4.7. (a) Yield and (b) size as a function of polymer concentration in the oil phase. Chloroform is used as the oil phase solvent and sodium metaphosphate is used as the surface-active molecule (the first and second step PVA concentration are fixed at 1.0% and 6.0%). SEM image of rods with (c) 7.0 mm, (d) 5.0 mm and (e) 3.2 mm average major axis size fabricated by two-step fabrication. (Scale bars are 1.0 µm).

as the surface-active molecule, at 5500 rpm and first and second step PVA concentrations of 1.0 and 6.0%, respectively. Three PLGA concentrations of 2.4, 1.8, and 1.4 mg/mL, resulted in rods with major axes ranging from 7.0 mm to 3.2 mm and minor axes ranging from 800 to 700 nm (Figure 4.7). The equivalent spherical diameter (ESD) for these rods is in the range of 1.0 – 1.7 mm, which is the smallest rod size to be achieved with the ESE technique to date. The fabrication yields for different sizes and polymer concentrations are summarized in Table 3.1, maintaining above 70% for all conditions tested (Figure 4.7a). Figures 4.7c–e shows the SEM micrographs of the rods with different sizes fabricated for the different oil phase polymer concentrations.

Polymer concentration	Average major axis size (µm)	Spheroid ratio (%)
2.4	7.0	74± 3.5
1.8	5.0	84±2
1.4	3.2	73±5

Table 4.1. Summary of the Fabrication yield and sizes of spheroids fabricated with two-step fabrication.

4.4.6. Particle loading with imaging agents

To show the capability of our fabrication method for encapsulation of therapeutics, we loaded the rods with Nile Red by adding the dye to the oil phase. Figures 4.8a and 4.8b show the fluorescent and confocal image of the loaded particles. The fabrication size and yield did not show any significant difference from the non- loaded particles fabricated in the similar conditions. The encapsulation efficiency and drug loading were measured for Nile Red loaded rods with ESD = 1.5 µm and were respectively equal to $25.2 \pm 1.3\%$ and 1.07 ± 0.06 wt/wt%. The release profile of Nile Red from rods of two different sizes with major axis sizes of 5.0 and 7.0 mm (ESD = 1.5 and

1.7 μm) were investigated. All particles demonstrated an initial burst release continued with a slower linear release phase which is consistent with the reported release from PLGA particles.[57] As shown in the Figure 4.8c, rods showed a faster release than spheres. For both sizes of rods, more than 90% of the dye content is released in three days. However, it took six days for the spheres to release 90% of their cargo. These results are consistent with existing literature and can be explained by the increased surface area of the rods compared to spheres of the same volume.[57] Smaller particles show slightly faster release which is consistent with the theories of diffusion modeling which predict that the cumulative release percentage is proportional to the radius of the particles. [57]
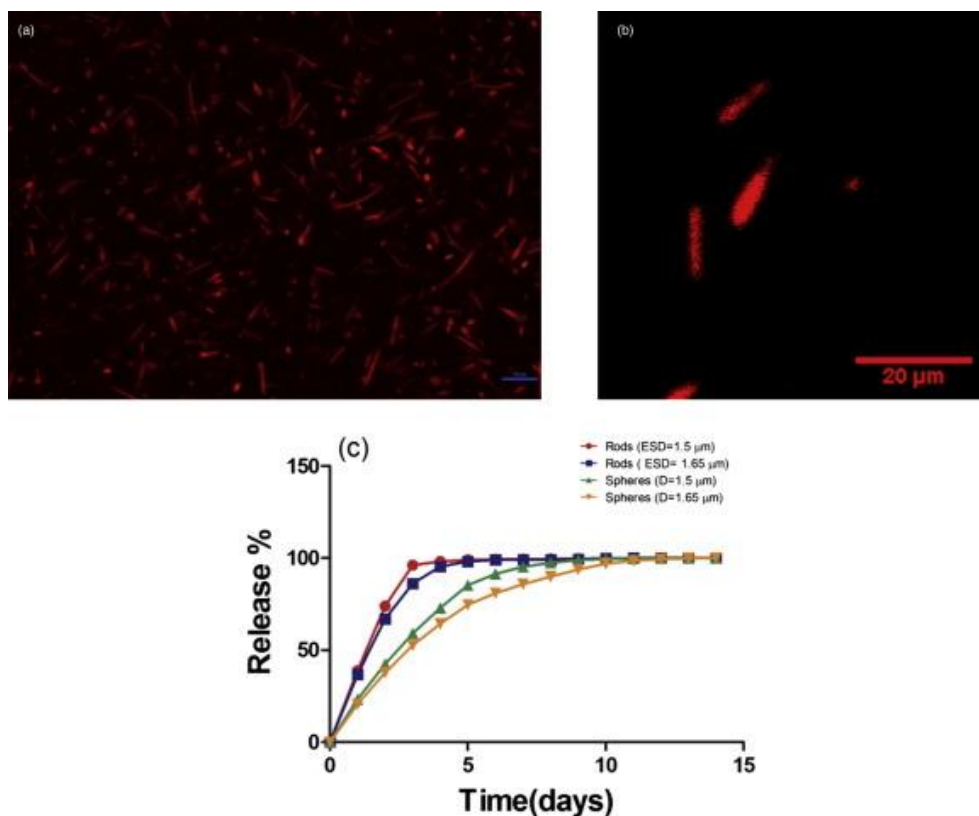
Figure 4.8. (a) Fluorescent (scale bar is 10 μm) and (b) Confocal image of the rods with 5.0 μm average major axis size loaded with Nile Red. (c) The release profile of Nile Red from loaded rods and spheres of two different sizes (error bars are smaller than 1% for all points).

4.4.7. *In vitro and in vivo adhesion of targeted rods to activated HUVEC monolayer*

To preliminarily test the utility of the submicron rods generated for targeted drug delivery, we conjugated the particle surface with an anti-ICAM-1 antibody ($\sim$25,000 sites/μm^2) and evaluated their adhesion to an activated HUVEC monolayer. A <u>laminar flow</u> of human RBCs reconstituted in flow buffer (DPBS with 1% BSA) at the WSR of $500\,s^{-1}$ was employed. Two different sizes of rods were used- major axes of 3.5 and 5 μm and minor axes of 700 and 800 nm, corresponding to the aspect ratios of 5 and 6, respectively. Spheres with the equivalent spherical diameter as rods were also tested. Targeted rods were capable of binding to the inflamed endothelium with similar or better adhesion level compared to spheres of equal volume (Figure 4.9a and b). Specifically, we found that the flow adhesion of rods increased by 18–25% compared which is in line with the previously reported data with <u>polystyrene</u> rods.[29] Also, larger rods had higher adhesion level compared to smaller rods, which again is consistent with the previously reported data showing particles with 2–6 μm equivalent spherical diameter have enhanced adhesion compared to the 1 μm particles for both rods and spheres.[22,121] This increase in the binding is due to the enhanced margination of rods to the cell-free layer, demonstrating their increased efficiency in targeting vascular wall.

To preliminarily assess the ability of the two-step generated PLGA rods to target a diseased vasculature in the complex *in vivo* environment, we conjugated particles with an anti-P-selectin antibody at ~100,000 sites/μm^2 and injected them into mice with inflammation in their mesentery tissue. Our intravital microscopy experiments demonstrated targeted PLGA rods can successfully bind to the wall in mesentery blood vessels in live mice with no observable adverse effect (Figure 4.9c), which had not been possible with the micron-sized rods previously fabricated with the ESE technique. The number of adherent particles per area of the vessel was quantified and was 1347 ± 274 particles/mm^2.
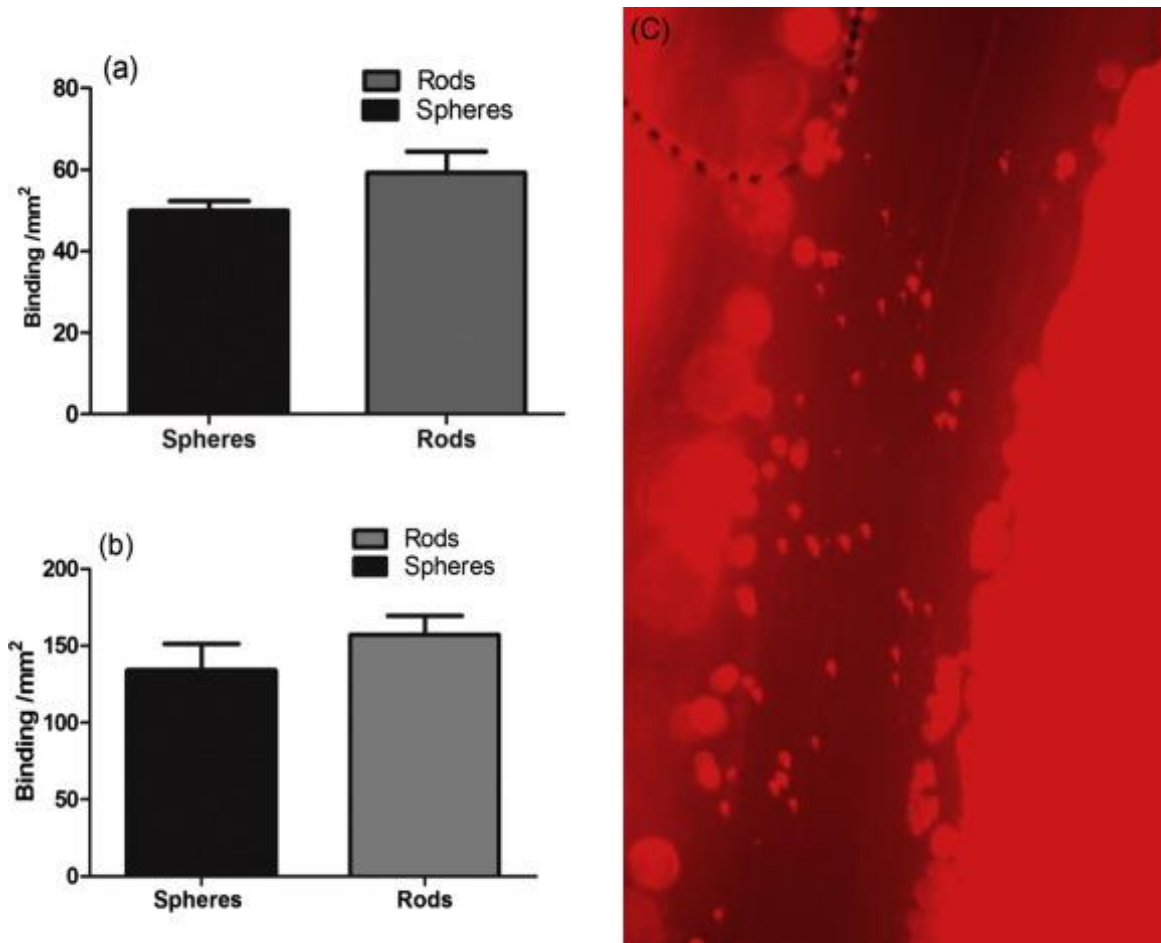
Figure 4.9. *In vitro* binding of (a) 1.3 μm and (b) 1.6 μm diameter spheres and rods with the equivalent volume in 40% RBCs in buffer. The experiments were performed at the 127 μm height channel and the wall shear rate (WSR) was set at 500 s−1. (c) *In vivo* binding of the anti-P-selectin coated rods with major axis and minor axis size of 3.5 *μm* and 700 nm in mice vessels stimulated with TNF-*α*.

4.5. Discussion

In this work, we have modified emulsion solvent evaporation into a two-step technique where rods with the submicron size range applicable in drug delivery applications are fabricated. In this method, shear-stretching of the emulsion droplets in a high viscosity and low interfacial tension medium enables the fabrication of the elongated particles. The previously developed conventional solvent evaporation technique has been unable to fabricate rods in the smaller size range that can be applicable in clinical applications without inducing blockage within the smaller capillaries. When the water phase viscosity of the emulsion and the shear rate were increased in the conventional one-step method in an effort to fabricate smaller rods, the stretching yield was constantly decreased, and a very small proportion of the recovered particles were rods. This limitation to produce smaller rods results from the stretching of oil droplets being a product of the competition between the shear forces and the capillary forces in the ESE method as defined by droplet dynamics.[122] As stated in the introduction, droplet deformation during the oil-water emulsification in the ESE technique is controlled by the capillary number, and the decrease in the capillary number as a result of a decrease in the droplet size make it impossible to fabricate smaller size rods with the conventional ESE technique. These results demonstrated that the interdependency of the various parameters that contribute to droplet dynamics and that the ESE technique would need to be significantly modified to allow fabrication of rod particles in the submicron size range required for drug delivery applications.

We modified the conventional one-step method to a two-step protocol where the droplet formation and stretching steps are separated. After the formation of the emulsion droplets, a high-viscosity solution is introduced to the system in order to induce a step increase in the viscosity of the system. This sudden increase in viscosity translates to a rise in the system Ca and a decrease

in the viscosity ratio, both of which favor droplet deformation and, hence, increases in the rod fabrication yield. Also, a higher viscosity will result in slower solvent removal and droplet solidification rate, allowing more time for the droplets to be stretched. With switching to the two-step protocol, the stretching yield was nearly 6-folds increased compared to the one-step protocol when all the other fabrication parameters were matched.

Our results also demonstrated that the choice of the oil phase solvent and the surface-active molecule is also a significant contributing factor to the stretching yield. When the performance of chloroform and dichloromethane were compared to each other, the results demonstrated that chloroform results in a higher stretching yield for all the shears and droplets sizes. This observation can be rationalized by chloroform having a significantly slower evaporation rate compared to DCM (the vapor pressure of chloroform and dichloromethane at 25 °C is 197 and 435 mmHg, respectively[123]) while having only a 29% higher viscosity (0.437 cP for DCM[124] and 0.563 cP for chloroform[125] at 20 °C). Thus, the utilization of chloroform as the oil phase solvent produces an increase in the evaporation time, translating to an increased time available for droplet stretching before droplet solidification. The near-equal performance of DCM relative to chloroform at the lower stirring speeds is likely due to the droplets at lower stir speeds being large enough, enabling them to be readily stretched even in the presence of DCM.[78,122] Amongst the three surface-active molecules explored, using NaMP led to the highest spheroid formation yield for all the stirring speeds used. The observed trend in the fabrication yield for different surface-active molecules can be explained by the chemical structure of the three molecules used (Figure 4.4). The negative charge on the oxygen molecules of the phosphate groups in NaTP and NaMP will lead to a stronger interaction with the hydrophilic groups of the PLGA polymer and lower interfacial tension, favoring droplet deformation compared to the hydroxyl groups of Trizma base.[78] The slightly

69

increased efficiency of NaMP at yielding more rods as compared to NaTP can be attributed to its increased ratio of the oxygen molecules to the sodium ions per molecular formula leading to the increased interaction with PLGA, hence better droplet deformation. To directly relate the observed trend in rod yield to the interfacial condition during stretching, we made measurements of the interfacial tension produced by the various surface-active molecules using a pendant drop method (needle SNS051/026 at 21 °C). The values of 2.46 ± 0.014, 2.86 ± 0.04 and 2.99 ± 0.01 mN/m were obtained for NaMP, Trizma and NaTP, respectively. As anticipated, the interfacial value obtained for NaMP was significantly lower than the values obtained for the Trizma and NaTP, confirming that the superior performance of this surface-active molecule to achieve high rod yield is due to a more favorable interfacial condition. Somewhat surprising, only a small difference was observed in the measured values between Trizma and NaTP despite the better performance of the later. It is possible that the interfacial tension obtained from the pendant drop method, which is conducted in static, does not adequately capture the condition that exists in the high shear and complex environment of particle fabrication. Indeed, we see that the trend with the measured interfacial forces better captures the trend in the rod yield when at the lowest stir rate of 2500 rpm than the trend at the higher stir rates.

After switching to the two-step method and finding the optimum choice of the oil phase solvent and surface-active molecule, we were able to fabricate rods with the major axis size as small as 3 μm with the stretching yield of 80% or higher. We also showed that our particles could be conjugated with the targeting ligands and be used for targeting inflamed vascular walls both *in vitro* and *in vivo* without causing any blockage in the smaller capillaries.

4.6. Conclusions

In this chapter, we used the knowledge of interface and droplet dynamics to introduce a new two-step emulsion solvent evaporation (ESE) fabrication technique for generating rod-shaped, biodegradable particles in submicron size ranges. We hypothesize that the separation of the droplet formation in the traditional ESE method from the droplet stretching should enable the creation of submicron droplets in the first step that are then stretched in the second step by manipulation of the system viscosity. With the optimized two-step process, we managed to fabricate rods in the optimal size range for vascular targeting applications, which had not been previously achievable with the traditional one-step ESE technique.[78,115,117] The choice of the oil phase solvent and the surface-active molecule is shown to be critical to the fabrication yield. Chloroform as the solvent resulted in a significantly higher yield than the conventionally used dichloromethane. Sodium metaphosphate, which is proposed to have stronger interactions with PLGA hydrophilic groups, produced the lowest interfacial tension and hence the highest fabrication yield. The ellipsoidal particles could be successfully conjugated with targeting molecules, e.g., anti-P-selectin and anti-ICAM-1. We demonstrated that targeted rods successfully bound to inflamed endothelium under shear flow in the presence of red blood cells both *in vitro* and *in vivo*. The level of adhesion observed for PLGA rods in human red blood cell flows was similar to the values previously reported for polystyrene model particles in the same size range.[29] The rods could successfully be injected into mice without blocking their vessels and were able to bind to the vascular wall when inflamed. No adverse effect of particle injection was observed for any animal. In future works, we aim to fully evaluate the capability of fabricated rods to function as a drug carrier for the delivery of therapeutics in atherosclerosis.

CHAPTER 5: Fabrication of Biodegradable Hexagonal and Rod-shaped Bile Salt-based Composite Microparticles

5.1. Publication Information

5.2. Abstract

Bile acids and their salts have been proposed as therapeutic agents for various diseases, including bile synthesis disorders, liver diseases, and obesity. Oral or subcutaneous administration of these drugs can limit their efficacy and impose unwanted side effects. In this chapter, we describe a gold templating method for fabricating solid microparticles that are primarily composed of bile salts – cholate or deoxycholate. The reduction of gold at the oil-water interface while having the bile salt in the water phase enables a gold-cholate/deoxycholate interaction at the oil-water interface, leading to the formation of bile salt particles. We demonstrated that composite microparticles release cholate/deoxycholate in solution through their degradation via surface erosion. The size and the shape of particles are controlled by changing the bile salt concentration in the water phase. We show that bile salt-based particles can be loaded with drugs using rhodamine as a model, allowing for co-administration of the released bile salt with other

therapeutic agents. Particle-based cholate/deoxycholate can open opportunities for targeted and localized delivery, which can improve efficacy while minimizing side effects associated with oral and subcutaneous use of these salts.

5.3. Introduction

Bile salts are naturally occurring surfactants that help to solubilize lipids in the small intestine and regulate several hepatic, biliary, and intestinal functions.[126,127] Bile acids and their salts have been proposed as therapeutic agents for the treatment of different conditions, including bile synthesis and peroxisomal disorders,[128] primary biliary cirrhosis,[129,130] gallstones and bile duct stones,[126,131] non-alcoholic fatty liver disease,[132,133] type-2 diabetes,[132] and for local removal of the undesired fat.[134] Two formulations of these salts are FDA approved for human use – orally-administered capsules of cholic acid for the treatment of bile synthesis disorders and liver dysfunctions[135] and subcutaneous injection of deoxycholic acid, Kybella, for the reduction of submental fat.[136] However, oral administration of these drugs limits their bioavailability, and subcutaneous injection of the salt solution can impose damage to the surrounding tissues through their membrane disruptive properties.[126,127] Controlled or targeted drug delivery has long been used as an alternative approach for the administration of the drugs to increase their specificity while lowering their side effects.[17] Thus, the fabrication of controlled release systems composed of bile salts can be a helpful strategy to address the identified limitations to the use of bile acids and their salts as therapeutics. Furthermore, bile salts can promote the absorption of some drugs when co-administered with or conjugated to the drug molecule, including cephalosporine, insulin, sotalol, flecainide, and calcitonin.[130] Thus, the potential for encapsulation of these drugs within particles composed of bile salts can help to improve their bioavailability.

In this chapter, we describe a novel method for the fabrication of gold-cholate composite microparticles for the controlled delivery of bile salts. We used an *in-situ* reduction of Au (Ⅲ) ion at the oil-water interface method to enable the formation of cholate/deoxycholate-based composite microparticles of various sizes and morphologies. Finally, cholate particles were successfully loaded with rhodamine dye as a model drug, highlighting the potential for the delivery of additional agents alongside bile salts to enhance their therapeutic effect.

5.4. Results

5.4.1. *Fabrication of bile salt composite microparticles*

In-situ reduction of the gold ions within emulsion droplets has been used previously for the fabrication of gold-loaded PLGA, poly (lactic-co-glycolic acid), nanoparticles.[137] In this work, we utilized the *in-situ* reduction of gold ions at an oil-water interface to enable the fabrication of gold-cholate composite microparticles via the well-established double emulsion solvent evaporation (ESE) technique. Scheme 5.1 demonstrates the step-by-step illustration of the process. The inner water phase of the system was doped with Au (Ⅲ) ions and sodium citrate as precursors for gold nanoparticle formation. The well-known Turkevich method to reduce the gold precursor encapsulated within the emulsion droplets to form nanoparticles.[138] The presence of an oil-water
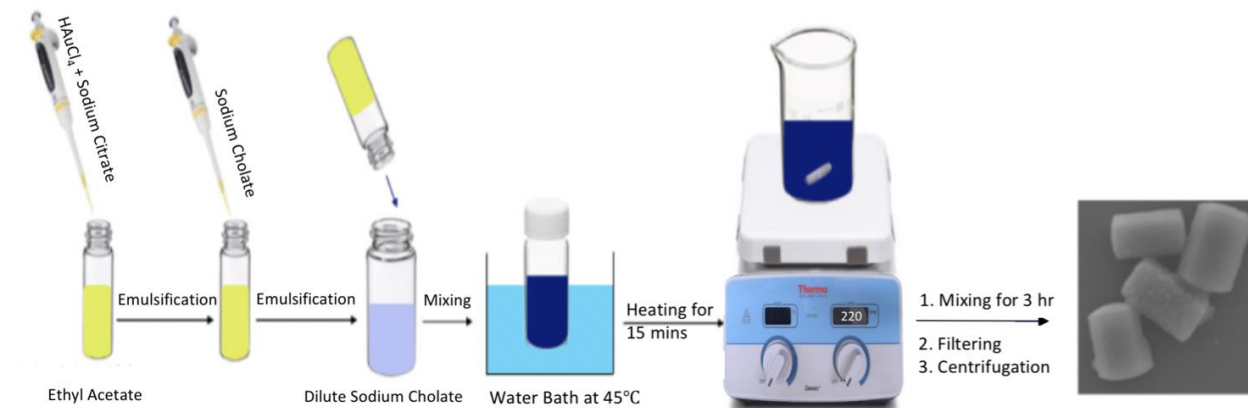
Scheme 5.1. Schematic illustration of the cholate-based microparticle fabrication process.
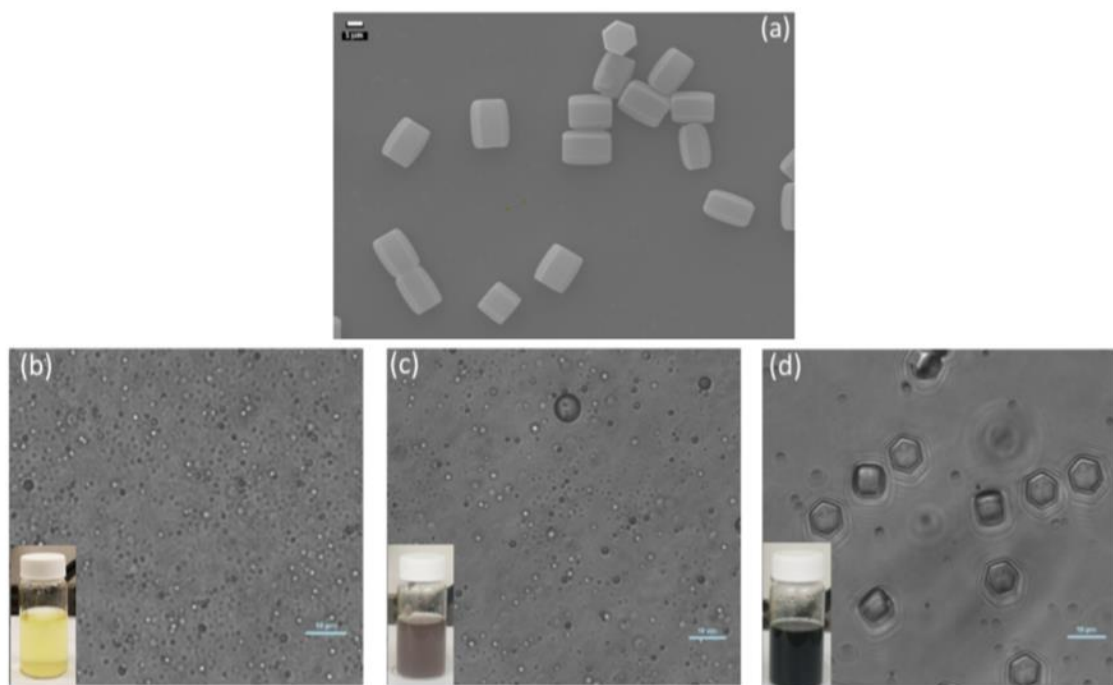
Figure 5.1. (a) SEM image of cholate-based hexagons fabricated with the modified emulsion solvent evaporation technique. The emulsion color and the shape of emulsion droplets as the heating and the reduction reaction proceeds after (b) 0 (c) 10 and (d) 15 minutes of heating (the scale bars of the bright field images are all 10 μm). The bright field images are zoomed in to make the features more visible.

interface and the reduction of gold ions facilitated the assembly of cholate to yield hexagonal microparticles composed of 90 wt% or more cholate in their structure. Upon completion of the self-assembly of cholate particles, the system was stirred to facilitate the evaporation of the organic solvent. The process yielded hexagonal-shaped cholate particles that can be separated from the free gold nanoparticles via low-speed centrifugation.

Figure 5.1a shows a scanning electron microscope (SEM) image of cholate particles fabricated via this technique. The reduction of the gold ions during the heating stage was signaled via a change in color of the reaction solution from yellow to dark blue-grey (Figure 5.1b- d). The self-assembly process and
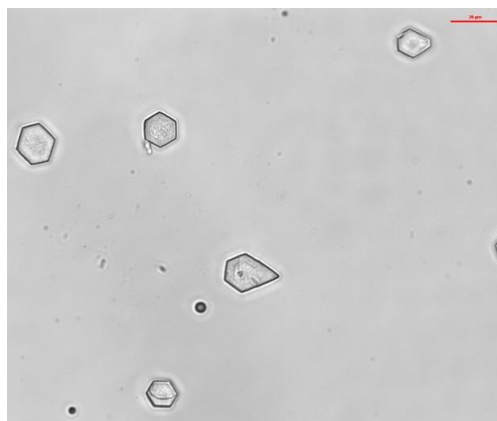
Figure 5.2. The shape of the particles fabricated when dichloromethane was used as the solvent in the system (the scale bar is 20 μm).

formation of the particles only occurred after completion of the heating step, i.e., Au (Ⅲ) reduction, but before the stirring step, as shown in Figure 5.1d. The presence of both the gold ion and sodium cholate were crucial factors for the formation of microparticles. When gold was eliminated from the system, no particles were formed in the process. A minimum $HAuCl_4$ to sodium cholate mass ratio of 0.2 was required for the formation of the microparticles. Below this limit, no cholate-based particles were formed, i.e., only gold nanoparticles recovered from the sample. These observations demonstrate that particle formation is a direct consequence of the *in-situ* reduction of the Au (Ⅲ) ion and its interaction with cholate, i.e., the gold-cholate interaction is essential for the self-assembly process. The presence of an oil-water interface in the system was also vital to the creation of the cholate-based particles. When the organic solvent was eliminated from the system, and $HAuCl_4$ was directly added to the sodium cholate solution, a white precipitate was immediately formed. Considering that cholic acid is a water-insoluble white powder and $HAuCl_4$ is an acidic compound, the direct addition of these two compounds likely led to a significant drop in the pH of the system, resulting in the formation of insoluble cholic acid particles. The existence of an organic solvent in the fabrication system prevented a pH drop, enabling the interaction of gold and cholate at the oil-water interface. This interfacial interaction of gold and cholate then facilitated the fabrication of cholate-based solid microparticles. The choice of the solvent did not affect the self-assembly of the droplets since hexagons were still formed with the use of dichloromethane as the solvent in the system instead of ethyl acetate (Figure 5.2). Finally, we demonstrated, using rhodamine dye, that the template-based method allows for the loading of hydrophilic agents within cholate microparticles (Figure 5.3).
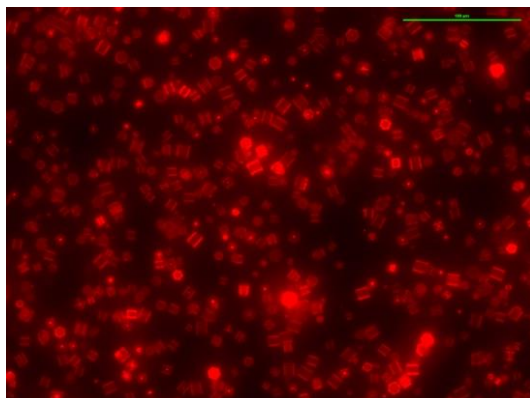
Figure 5.3. Rhodamine loaded cholate-based hexagons fabricated by the modified emulsion solvent evaporation technique (the scale bar is 100 μm).

5.4.2. Characterization of the composite microparticles.

We used different techniques to characterize and confirm the presence of cholate in the microparticle structure. First, we measured the zeta potential of the particles, which was found to be -66.0 ± 3.0 mV. Others have previously shown that adsorption of bile salts on the surface of nanoparticles significantly increases the absolute negative value of their zeta potential.[139] The observed highly negative zeta potential of our particles is thus consistent with cholate being the main component of the surface of the microparticles. Energy-dispersive spectroscopy (EDS) was then used to identify the elements incorporated within the structure of the hexagons. We performed elemental analysis on the fabricated hexagons, as demonstrated in Figure 5.4a-b. Carbon and gold were the main elements present on the surface of the hexagons. X-ray photoelectron spectroscopy (XPS) was used as a secondary method to confirm the elemental composition of the hexagonal microparticles. After separating gold nanoparticles from the hexagons via centrifugation, the pellet containing the hexagons are dried and mounted on indium (In) foil for XPS analysis. As shown in Figure 5.4c, the sample is primarily composed of carbon, oxygen, and gold. Carbon and oxygen make up about 90 wt% of the particle surface composition, with the other 10% being gold. Finally,

77
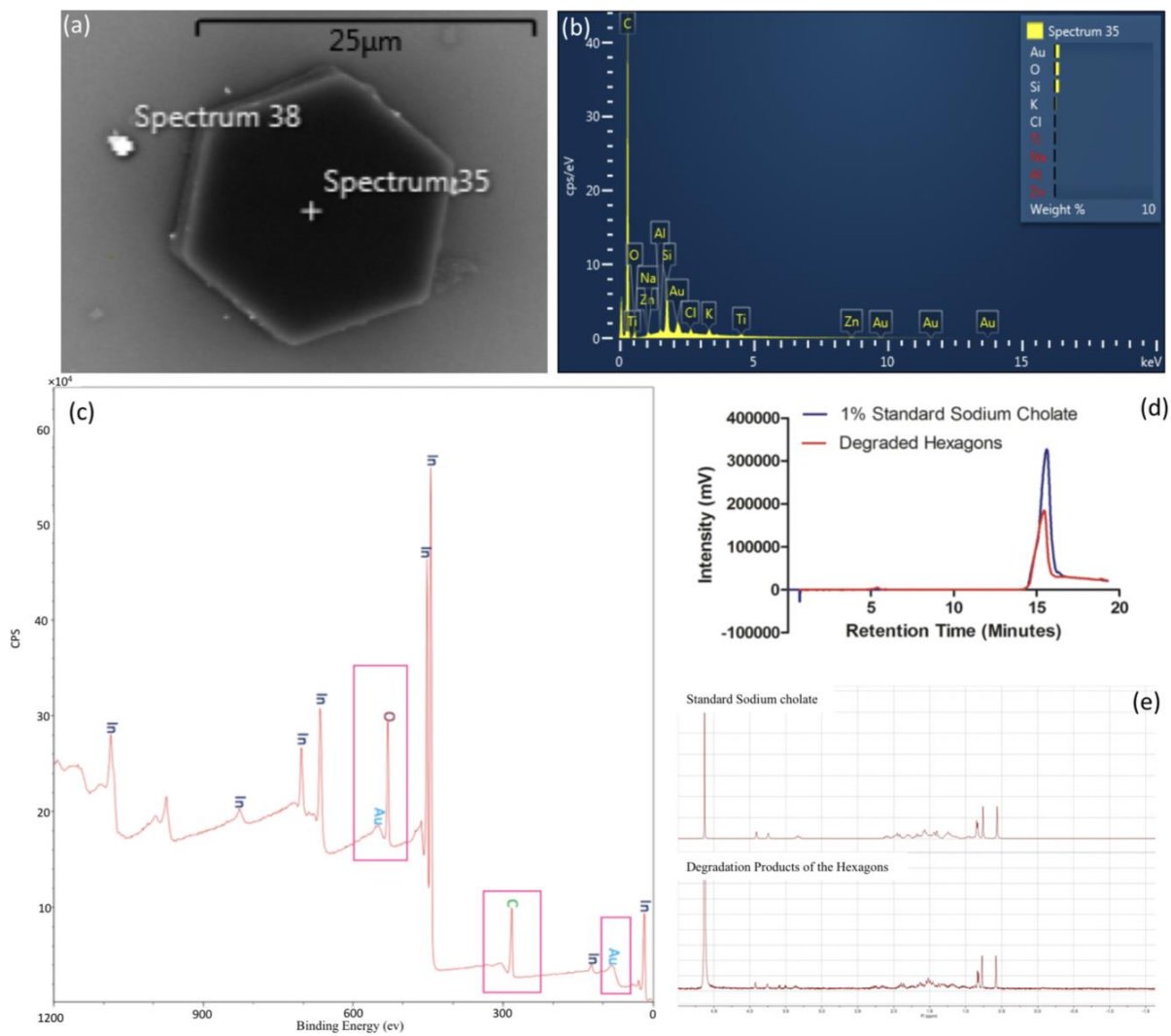
Figure 5.4. (a) SEM image of the product of the fabrication process. (b) EDS analysis of cholate-based hexagons. The presence of silicon and other elements in the spectrum is the result of drying the sample on a glass slide. (c) XPS analysis on the dried cholate hexagons mounted on Indium foil. Colored elemental labeling are added to the data and pink boxes are drawn around the carbon, oxygen, and gold peaks to make the data more comprehensible. (d) HPLC analysis on the degradation products of hexagons (red peak) and standard sodium cholate solution (purple peak) in a 50:50 mixture of acetonitrile and water. (e) Proton NMR spectrum of 3% standard sodium cholate (top) and the degradation products of cholate-based hexagons (bottom) in deuterated water. The high-intensity peak showing up at 4.6 ppm is the solvent peak. The intensity of the peaks for degraded hexagons are increased by MestReNova software to make the comparison between the two spectrums easier.

high-performance liquid chromatography (HPLC), and nuclear magnetic resonance spectroscopy (NMR) were used to confirm the presence of cholate in the structure of the microparticles. For HPLC analysis, the degradation product of the hexagons was run through an HPLC column alongside a standard 1.0% sodium cholate solution. As shown in Figure 5.4d, the HPLC peak for the degraded hexagons (red peak) showed up at the same retention time as the standard sodium

78

cholate (purple peak) solution. Figure 5.4e shows proton NMR spectrums of the standard 3% sodium cholate solution and the degradation products of hexagons in deuterated water. Again, the peaks for both the standard and the particle degradation products were at the same chemical shift values, with the same splitting pattern and relative intensities, confirming the presence of sodium cholate as the main compound in the structure of the hexagons.

Sodium Cholate Concentration in the Outer Water Phase	Hexagon Diameter (μm)	Hexagon Height (μm)
0.75%	8.7 ± 2.3 μm	5.3 ± 0.8 μm
2%	5.4 ± 1.1 μm	4.3 ± 0.7 μm
3%	2.9 ± 0.3 μm	3.6 ± 0.7 μm

Table 5.1. The size of the cholate-based hexagons formed in the presence of different sodium cholate concentrations in the outer water phase.

5.4.3. Fabricating microparticles of different sizes and morphologies.

The size and shape of particulate delivery systems have proven to be a controlling factor in their *in vivo* tissue distribution,[36,140,141] rate and extent of phagocytosis,[24,58,60] circulation time,[102,140] and degradation kinetics.[57,142] Thus, we sort to modify our protocol to enable fabrication of particles with different sizes and shapes.
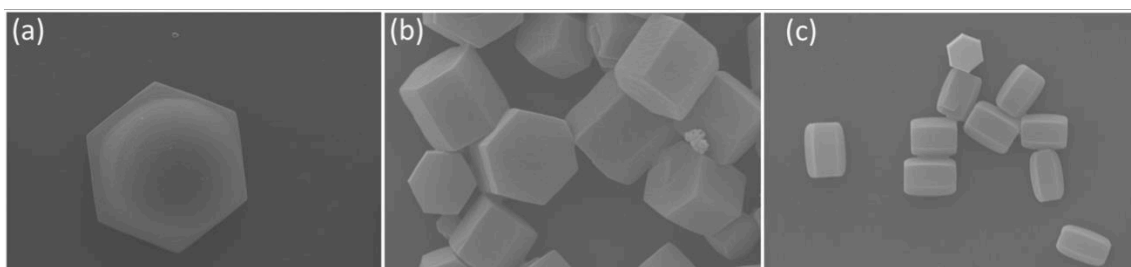
Figure 5.5. SEM image of the cholate-based hexagons with different sizes fabricated in the presence of (a) 0.75% (b) 2% and (c) 3% sodium cholate in the outer water phase. The scale bars are all 1 μm in size.

Prior publications have demonstrated that changing the surfactant concentration in the water phase changes the size of the emulsion droplets,[79] we first varied the sodium cholate concentration in the outer water phase in our system to fabricate hexagons of different sizes. Table 1 shows how the size of the hexagons varies as a function of changing surfactant concentration from 0.75 to 3%. In line with previous studies,[79] higher surfactant concentrations resulted in smaller particles, ranging from a diagonal of 9 down to 3 µm as shown with the SEM images in Figure 5.5. Sodium Cholate concentrations lower than 0.75% did not stabilize the emulsion and resulted in particles with unsmooth surface morphologies (Figure 5.6a). When sodium cholate concentrations of higher than 3% were used in an attempt to achieve smaller hexagons, particles with fibrous morphology were formed instead. Further increases in the surfactant concentrations increased the percentage of the fibers in the product (Figure 5.6b). Concentrations of sodium cholate 10% or more resulted in 100% rod-shaped particles.
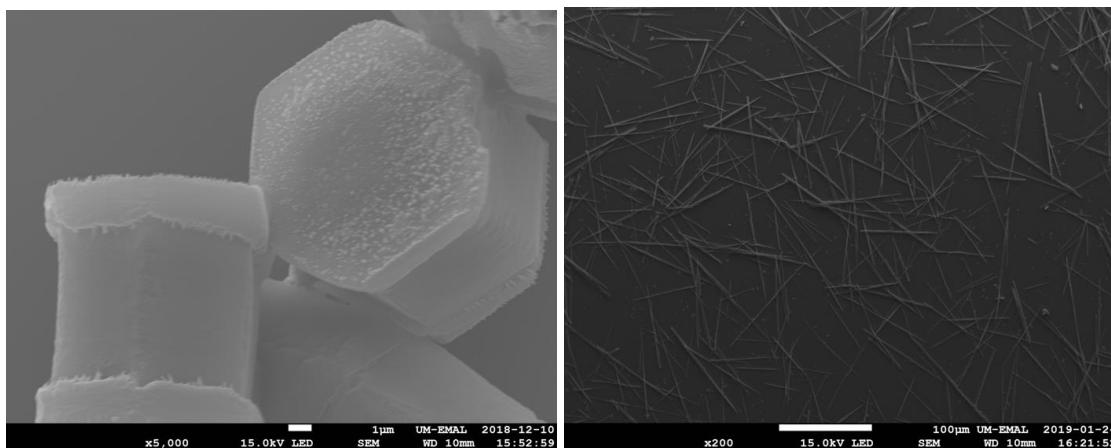
Figure 5.6. (a) SEM Image of the cholate-based hexagons with unsmooth surface fabricated in the presence of 0.5% sodium cholate in the outer water phase. (b) The image of the fibrous particles fabricated in the presence of 10% sodium cholate in the outer water phase.

A dimensionless ratio called the capillary number – a ratio of the viscous forces to the capillary forces – controls the formation of droplets and their eventual stretching or break up for emulsion-based particle fabrication systems. As shown in Equation 5.1, the capillary number is defined by the system shear rate (γ), water phase viscosity (η_s), the radius of the initial oil droplet

(a), and the interfacial tension(Γ) between the oil and the water phase.[78] Higher capillary numbers favor droplet deformation.

$$Ca = \frac{\gamma.\eta_s.a}{\Gamma} \text{ (Equation 5.1)}$$

Prior publications have demonstrated that the addition of surface-active molecules, such as the presence of certain fluorescent dyes, can lower the interfacial tension at the oil-water interface.[143] Considering that lower interfacial tension values will favor the droplet deformation as discussed in the previous paragraph, we added 6-carboxyfluorescein to the gold precursor in an attempt to change the shape of the composite microparticles. Microstructures of regular hexagon shape were present immediately after the heating step as before (Figure 5.7a), indicating that the presence of the 6-carboxyfluorescein dye does not interfere with the self-assembly during the heating stage. However, once the reaction mixture is stirred to evaporate the residual solvent, the hexagons were stretched into hexagonal bipyramids (Figure 5.7b) due to the 6-carboxyfluorescein lowering the interfacial tension of the system (Equation 5.1). This observation is likely the first report of the coupling of a self-assembly particle formation process and droplet dynamics.
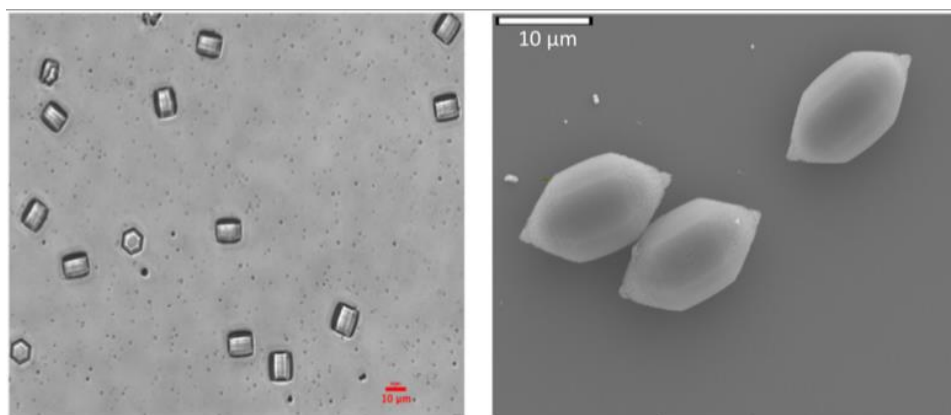
Figure 5.7. (a) The shape of the microstructures after the heating step when 6-carboxyfluorescein was added into the inner water phase. (b) SEM image of the elongated bipyramidal hexagons fabricated in the presence of the 6-carboxyfluorescein. The scale bars are both 10 μm in size.

5.4.4. Characterizing the degradation kinetics of microparticles.

The degradation kinetics of the cholate-based particles were tested by incubating them at 37 ℃ for different time intervals and imaging them via SEM. As shown in Figure 5.8, the particles maintained their shape after being freeze-dried. Incubation of the particles in deionized water at 37 °C for 24 h resulted in the erosion of salt from the surface of the particles, which led to a decrease in their overall size at longer incubation times. After two weeks of incubation in water, cracks were formed on the surface of the particles, and surface erosion appears to be the dominant mechanism for the degradation of the particles. Quantification of the cholate released from degrading particles over time demonstrated a near-linear release profile, confirming that particle degradation is primarily by surface erosion (Figure 5.9).[144]
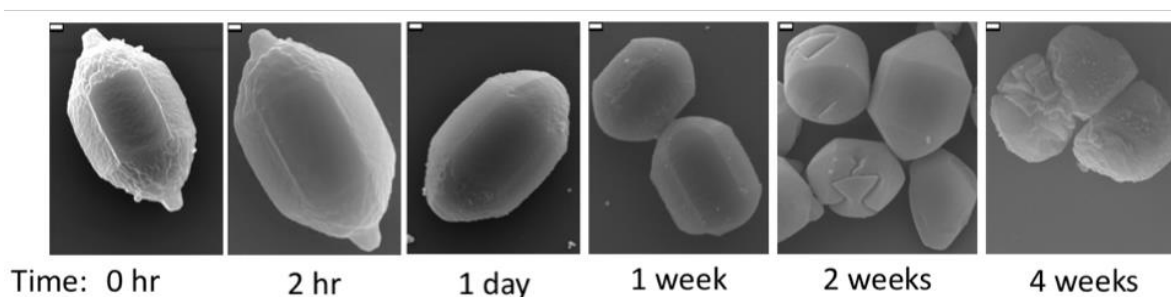
Figure 5.8. Degradation profile of the elongated bipyramidal particles after being incubated at 37 °C for different time points. The scale bars are all 1 μm in size.
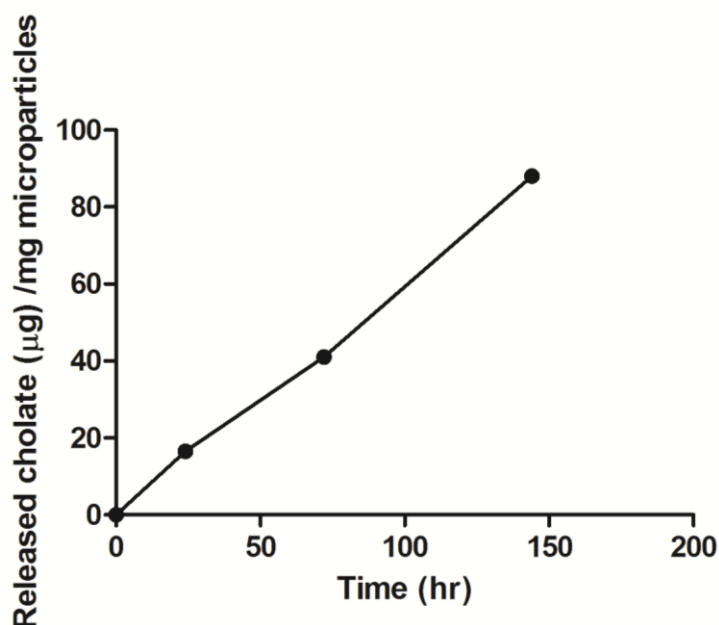
Figure 5.9. The amount of released cholate per mg of the dried composite microparticles after incubating them at 37 °C for different time points.

5.4.5. *Fabrication of deoxycholate-based composite microparticles.*

Next, we explored whether our templating method can be modified to fabricate particles composed of other bile salts by attempting to fabricate deoxycholic acid particles. Deoxycholic acid is a secondary bile acid formed by intestinal bacteria via the metabolism of cholic acid.[145] Deoxycholic acid has been used for local digestion of the fat tissue, and its FDA approved commercial formulation, Kybella, is used for the reduction of submental fat.[133,146] However, the associated inflammation and damage to the surrounding tissues upon subcutaneous injections of the soluble formulation has limited its clinical usage.[132,147] Fabrication of deoxycholate-based controlled release systems may present a solution to the mentioned issues.

Deoxycholate-based composite particles were fabricated using the same protocol as described for above, replacing sodium cholate with sodium deoxycholate in the outer water phase.

Deoxycholate-based microparticles exhibit a rod-shaped morphology (Figure. 5.10a). At the central fabrication condition, where 1% sodium deoxycholate is used in the outer water phase, an average length of 8.4 ± 3.2 μm and width of 870 ± 300 nm was achieved. The presence of the deoxycholate in the structure of the particles was confirmed via H^1-NMR spectroscopy. The spectrum of the particle degradation products was then compared with the spectrum of a standard deoxycholate solution. As demonstrated in Figure. 5.10b, all the peaks of the standard deoxycholate solution were present in the spectrum of the degraded particles, confirming deoxycholate as the main component in the structure of the particles.
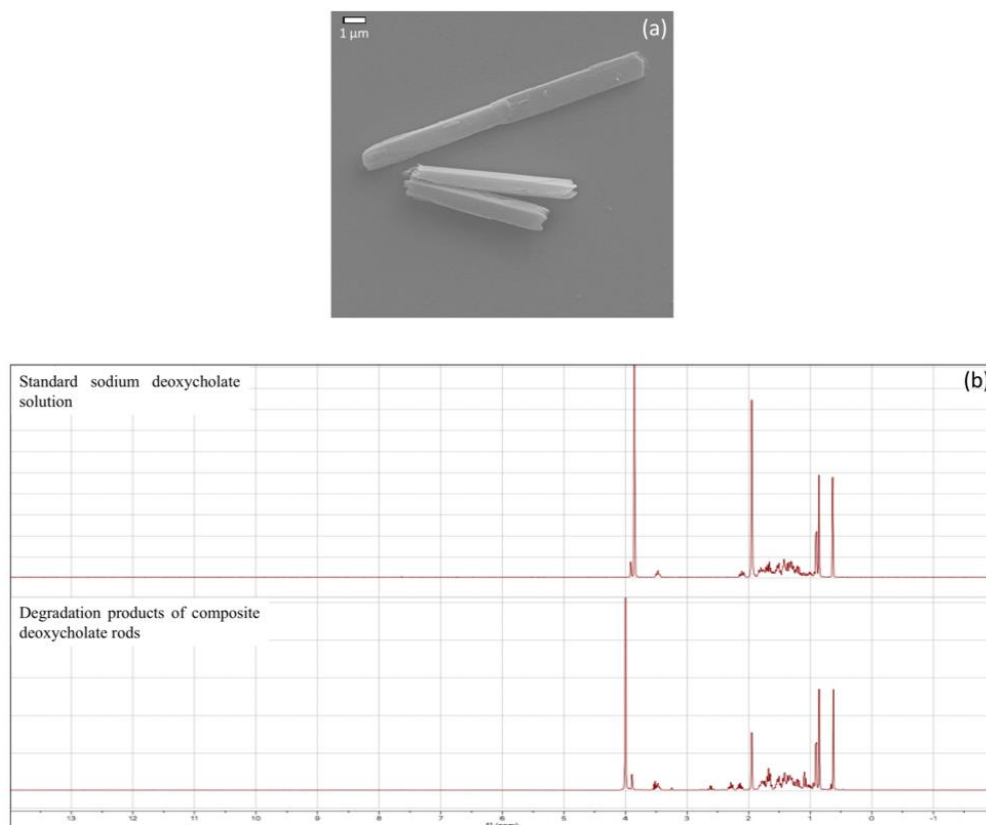
Figure 5.10. (a) SEM image of the deoxycholate-based composite microparticles. (b) Stacked NMR spectra of a standard 1% sodium deoxycholate solution and degradation products of the deoxycholate-based composite rods in a 50:50 mixture of deuterated acetonitrile and water. The two high intensity peaks showing up at the chemical shift values of 1.95 ppm and ~4 ppm are the solvent peaks.

5.5. Discussion

In this chapter, we have innovated a new metal-assisted bulk templating method to fabricate biodegradable particles made of off bile salts. This is the first time solid controlled release systems composed of bile salts have been fabricated. The reduction of the gold ions at the oil-water interface initiates the formation of the composite microparticles. Cholate has been used before as a reducing and capping reagent in the reduction of gold nanoparticles to produce hexagonal or triangular gold nanoparticles.[148] Gold nanoparticles self-assemble in the oil-water interface, serving as a template for the formation of cholate salt particles, which we hypothesize is governed by a nucleation and growth mechanism. First, there is the formation of the gold nanoparticles within the inner water phase of the emulsion, which serves as a nucleus for the self-assembly of the cholate shell around nanoparticles – i.e., the interaction between hexagonal gold core and the carboxylate group of cholate ions leads to the formation of the gold-cholate composite microstructures. We were also able to fabricate deoxycholate microparticles by using sodium deoxycholate instead of sodium cholate in the water phase. The presence of bile salts as the main elements in the structure of particles was confirmed via various chemical characterization techniques. We also demonstrated the capability of our method to load hydrophilic agents such as rhodamine within the structure of microparticles for the combination therapy purposes. The composite particles degrade via surface-erosion and release bile salts into the solutions in a near-linear fashion, which makes them suitable candidates as controlled release systems where the limited efficacy and side effects of the bile salts have limited their usage.

5.6. Conclusions

In this chapter, we report that the interaction of gold ions and bile salts, and reduction of the former, at an oil-water water interface, could be used to fabricate solid bile salt microparticles. Through this metal-assisted bulk templating technique, we were able to fabricate bile salt-based microparticles of various sizes and shapes. Formation of the metal-cholate hydrogels with fibrous supramolecular morphology has previously been reported and used for templating metal-sulfide nanoparticles.[149] However, there is no prior report of the fabrication of stable micro/nanoparticles that are composed primarily of bile salts in their structure. The results of this work will open avenues for bile salt particles to be used as controlled-release drugs for the treatment of different liver disorders and obesity, which we will evaluate *in vivo* in our future work. Finally, conjugating the particles with targeting ligands can also be used to guide them to other disease sites where drugs with lipid membrane disruptive properties are desired.

CHAPTER 6: Utilization of Bile Salt Particles for Localized Dissolution of Fat and Cancer Treatment

6.1. Publication Information

6.2. Abstract

Bile salts are currently being used or proposed as therapeutics for various types of disorders including localized fat, liver disorders, and cancer. However, their limited efficacy and unwanted side effects has limited their usage. Utilization of controlled released systems can be a solution to this problem. In this chapter, we show that the composite bile salt microparticles fabricated via the bulk-templating method in chapter 5 can be used as controlled released systems for fat lysis and cancer treatment. We show that these particles are capable of lysis adipocytes *in vitro* with a higher efficacy that the salts of the same concentration. We also showed that particles are capable of inducing apoptosis in colon cancer cells *in vitro*. Our data demonstrates that our composite microparticles can have the potential of being introduced as a new therapeutic formulation to increase the treatment efficacy and minimize the side effects for a range of disorders.

6.3. Introduction

As mentioned in the previous chapter, bile salts can be used as therapeutics for a range of disorders. However, the unwanted side effects and limited efficacy have limited their therapeutic potential.[126,128–133] The usage of our controlled release systems fabricated in the previous chapter can be a solution to the mentioned issue. The subcutaneous injection of bile salt solutions for fat lysis has been associated with inflammation and damage to the surrounding tissues, including muscles, skin, and nerves.[133,147] These side effects associated with Kybella, the commercially available form of deoxycholic acid, have limited its usage. Furthermore, each dose of Kybella often requires 20-50 injections to the target area, which may be undesirable for patients. Controlled release delivery systems have been used as a treatment approach to minimize the adverse effects of therapeutics.[150]

Another potential application of bile salts in the treatment of colorectal cancer. Previous work has demonstrated that deoxycholic acid and chenodeoxycholic acid are capable of inducing apoptosis in colorectal cancer cell lines.[151–153] However, these salts have been shown to either promote cell proliferation or have no apoptotic effects at concentrations below 100 μM.[152–154] Also, the potential apoptotic effect is time-dependent, and a minimum time for the contact of the cells and the salts is required to observe apoptosis, by which the salts might have gotten cleared via circulation.[152,153] Thus, in order to utilize the potential of the bile salts for destroying tumor lesions, we need to design a system that can maintain a sustained local concentration of the salts near the cancer cells *in vivo*, and controlled release systems can be a solution to this.

Our composite bile salt particles could serve as a controlled release alternative to the deoxycholic acid for solving the issues mentioned above. Here, we tested the capability of our

particle formulation to lyse fat cells by incubating them with primary subcutaneous human adipocytes or fat tissue in *in vitro*, and *ex vivo* settings. We showed that the composite microparticles are able to lyse the adipocytes and induce apoptosis in colon cancer cells in a time and concentration dependent manner. The bile salts were also able to lyse the adipose tissue after *ex vivo* incubation. All these results show the potential of these particles to replace bile salt soluble formulations to destroy fat tissue or tumor lesions, which would be further investigated in the ongoing *in vivo* work in our lab.

6.4. Results

6.4.1. *In vitro lysis of human subcutaneous adipocytes by bile salt composite microparticles*

In this section, we tested the lipolytic capability of our bile salt particle formulation by incubating them with primary subcutaneous human adipocytes *in vitro*. First, for a control, adipocytes were incubated with different concentrations of sodium cholate and sodium deoxycholate solutions in RPMI media. Consistent with previous studies,[155] our results demonstrated the lysing of adipocytes after incubation with bile salts in solution. As demonstrated in Figure. 6.1a, sodium deoxycholate was more potent in lysing the fat cells than sodium cholate. Specifically, sodium deoxycholate concentrations of higher than 0.05% were enough to kill fat cells within 1 hr. In contrast, a 1% or higher solution of sodium cholate was necessary to achieve lysing of 100% of cells. The difference between the cell viabilities was not significant for the 0.1, 0.05, and 0.01% sodium cholate concentration (Figure. 6.1a). Though the cell viability after incubation with 0.1% and 0.05% sodium cholate respectively decreased from 50%, and 57% to 30% after increasing the incubation time from 1 h to 3 h, the general response of the cells to the salt incubation was not heavily time-dependent (Fig. 6.1a).
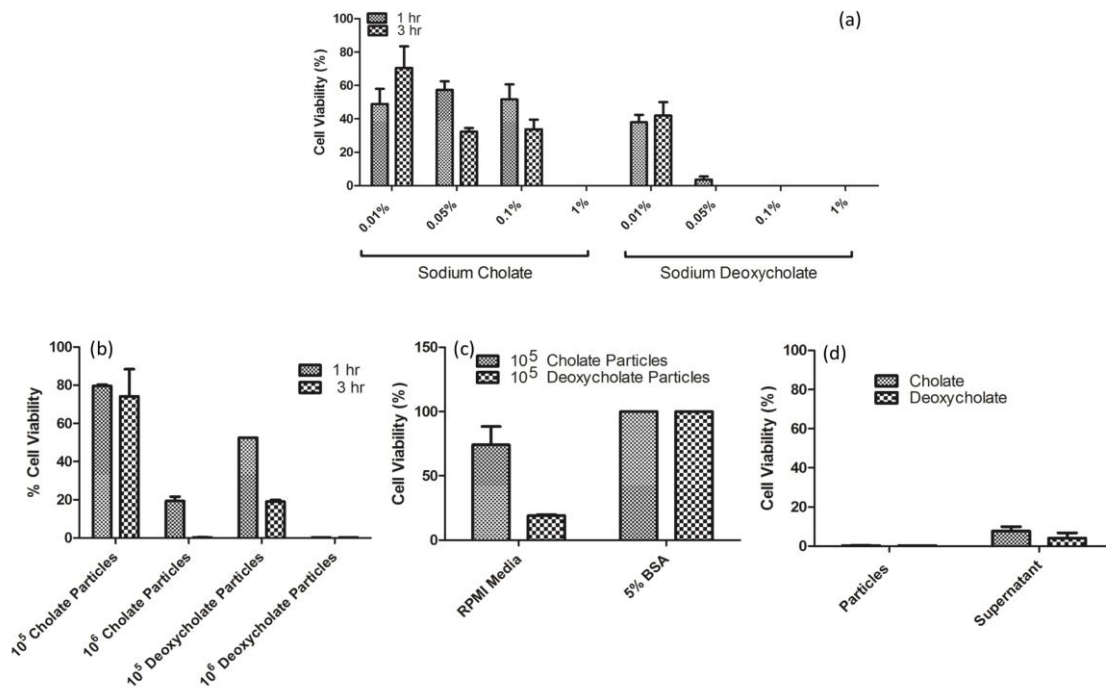
Figure 6.1. Cell viability of the primary subcutaneous adipocytes after being incubated with (a) different concentrations of the sodium deoxycholate and sodium cholate salts in RPMI media (b) different concentrations of cholate-based and deoxycholate-based composite microparticles for different time points. (c) The inhibitory effect of the BSA on the lysis effect of deoxycholate and cholate-based microparticles. (d) The cell viability after adding the supernatant of particles after preincubation in media (the degradation products of the particles) to the cells. Each condition has been replicated for three different wells.

When we incubated adipocytes with our composite particles, both the cholate and deoxycholate-based particles were able to lyse the cells successfully (Figure. 6.1b). Similar to the salt solutions, deoxycholate particles were more potent in killing the cells compared to the cholate particle. However, in contrast to the salt solutions, the lysis response of the adipocytes to the composite particles was profoundly time dependent. When 10^5 cholate-based particles were added to each well, which yields a maximum salt concentration of 0.004% if the particles were degraded completely, the particles were able to only kill about 20% of the cells independent of the incubation time. When the concentration of the particles was increased to 10^6 particles/well (maximum

90

effective concentration of 0.04%), 80% of the cells were killed after 1 h of incubation, and this number was increased to nearly 100% when the incubation time was increased to 3 hr. For the deoxycholate particles, even 10^5 particles (maximum effective concentration of 0.0035%) were enough to lyse 40% of the cells within 1 h of incubation and 80% of them after 3 hr. A deoxycholate particle concentration of 10^6/well (the maximum effective concentration of 0.035%), was enough to kill all the cells after a 1 h incubation. Previous studies have shown the inhibitory effect of bovine serum albumin, BSA, on bile salt-induced lysis of the adipocytes.[155] To confirm that our bile salt particles work with the same mechanism as the solution, we incubated 10^5 of both the cholate and the deoxycholate particles with each well of the cells for 3 h in media or media with 5% BSA. Though the particles were able to lyse the cells in media, the lysis effect was inhibited entirely in a 5% BSA solution (Figure 6.1c). This observed result confirms that our composite bile salt particles lyse fat cells with the same mechanism as the salt. Next, we sort to demonstrate that bile salt molecules released from degrading particles are responsible for the cell lysis in assays with particles. We preincubated the particles in media at 37 °C for 3 h and centrifuged the mixture to remove undegraded particles. Fat cells were then incubated with the supernatant containing the released salts, and the viability of the cells was measured as before. As demonstrated in Figure. 6.1d, the supernatant containing the released bile salts was able to successfully lyse 90-95% of the cells within 3 h, confirming that our composite microparticles can gradually degrade and release cholate/deoxycholate to lyse the fat cells. The results in this section show that the composite microparticles can be used as controlled release systems for local digestion of fat tissue for the treatment of obesity. In a preliminary analysis, we demonstrate particles injected into the of mice via the tail vein did not cause mortality in mice over the 24 h period evaluated. Future work will require a full evaluation of the biocompatibility and ability of our bile salt microparticles to reduce

fat tissues in vivo in obese animal models without the adverse effects reported for their corresponding salt solution.

6.4.2. *Ex vivo adipose tissue assays after incubation with bile salt composite microparticles*

To examine the capability of the cholate and deoxycholate-based particles to lyse the fat tissue, we incubated beef adipose tissue with either PBS, deoxycholate solution, or the composite particles at 37 ºC for different time-points. As represented in Figure 6.2a, even though incubation with PBS will have minimal effect on the tissue, incubating the samples with 1% sodium deoxycholate or different numbers of the particles will start lysing the fat and resulting in a milky solution. Incubation of the tissue with gold nanoparticles, and PLGA and polystyrene microparticles also show that the lysis effect is specific to the bile salt particles. When, the amount of the free fatty
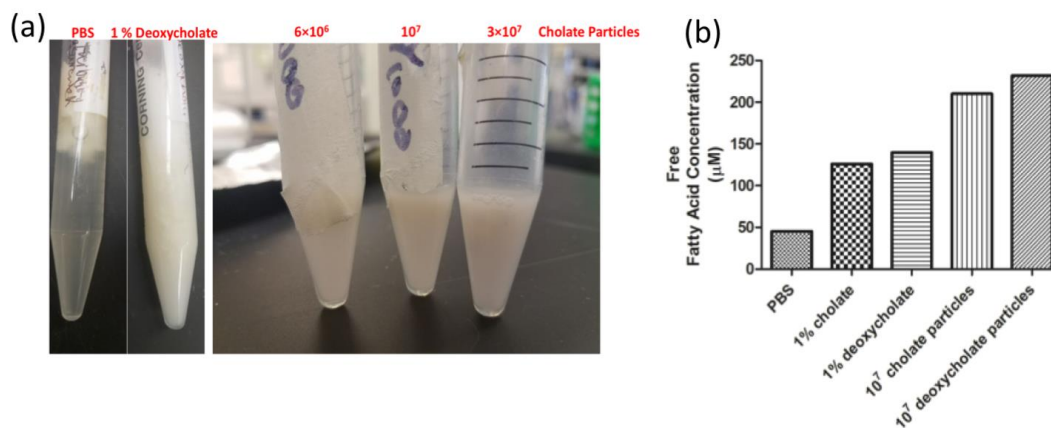
Figure 6.2. (a) The visual appearance of beef adipose tissue after being incubate with PBS, sodium deoxycholate, or composite cholate microparticles. (b) Released free fatty acid content of 0.5 gr beef adipose tissue after being incubated with 1 mL of PBS, 1% sodium cholate, 1% sodium deoxycholate, 10^7 cholate-based, and 10^7 deoxycholate-based composite particles in PBS.

acids in the incubation medium was measured there was a significant increase in the released fatty acids after incubating the particles with either of the cholate or deoxycholate salt solutions or the composite particles from 44 µM for PBS incubation to 100 µM or higher for either of the salt/particle incubations. Both of the deoxycholate salts and particles released more fatty acids compared to the cholate control of the same concentration (Figure 6.2b). Interestingly enough, the

fat tissue was not lysed when gold nanoparticles, polystyrene, or PLGA microparticles were incubated with it as a control, showing that the observed cell lysis is specific to bile salt particles (Figure 6.3). To summarize, our composite bile acid-based microparticles can successfully lyse the fat tissue and have the potential for localized dissolution of fat.
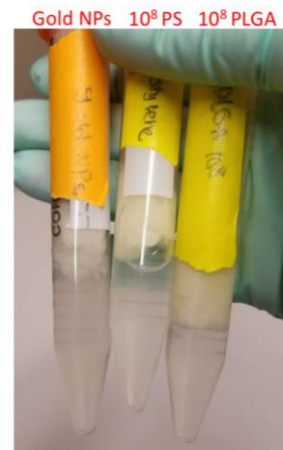
Figure 6.3. The appearance of fat tissue after being incubated with gold nanoparticles, 2 µm polystyrene (PS), and PLGA microparticles as control for 3 h.

6.4.3. *In vivo* lipolysis assays

In order to investigate the lipolytic capability of our composite particles, they were subcutaneously injected into the inguinal fat pads of the obese mice alongside the salt formulations. The weight of the individual animals, which had received different lipolytic formulations was tracked. The percentage of weight change compared to the injection day for each individual animal was then quantified. As shown in Figure 6.4, our preliminary results demonstrated that similar to the salts, particle formulations were able to decrease the average weight of animals over the period of one-week. This weight-loss was not observed in control animals that had only received PBS injection. In our ongoing work, we will be tracking the weight-loss in animals over an extended time course and with a more frequent dosing. The lipolysis in the fat pads and the inflammation in the adjacent tissues will also be investigated via histology for each individual animal.
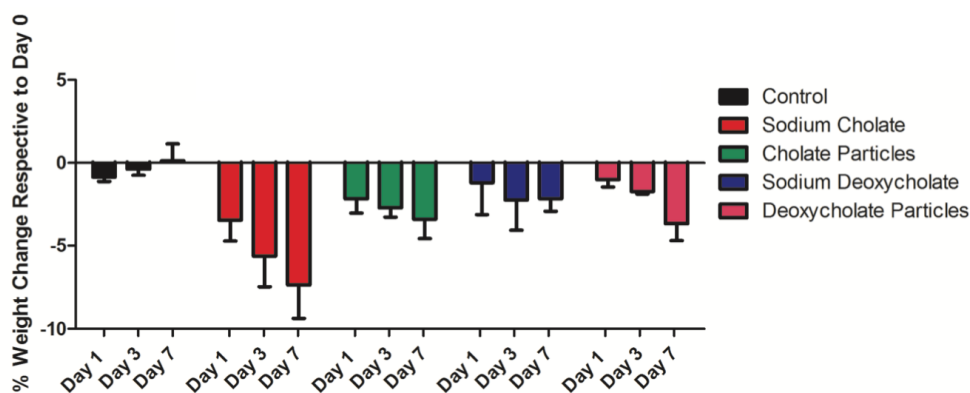
Figure 6.4. The change in the weight of animals over time after receiving 2.5 mg of sodium cholate, cholate composite particles, sodium deoxycholate, and deoxycholate composite particles in 100 µL PBS via subcutaneous injections into their inguinal fat pads. Control animals had only received PBS, and each condition was replicated at least for N=4.

6.4.4. *In vitro lysis of HCT-116 Colon Cancer Cells with Composite Microparticles*

As stated in the introduction, bile salts have been shown to induce apoptosis in cancer cell lines *in vitro*. To confirm that our microparticles can be used as controlled release systems to destroy tumors, we incubated our composite microparticles with cancer cells and tested their viability. As shown in Figure 6.5, above a threshold concentration, incubation with the composite
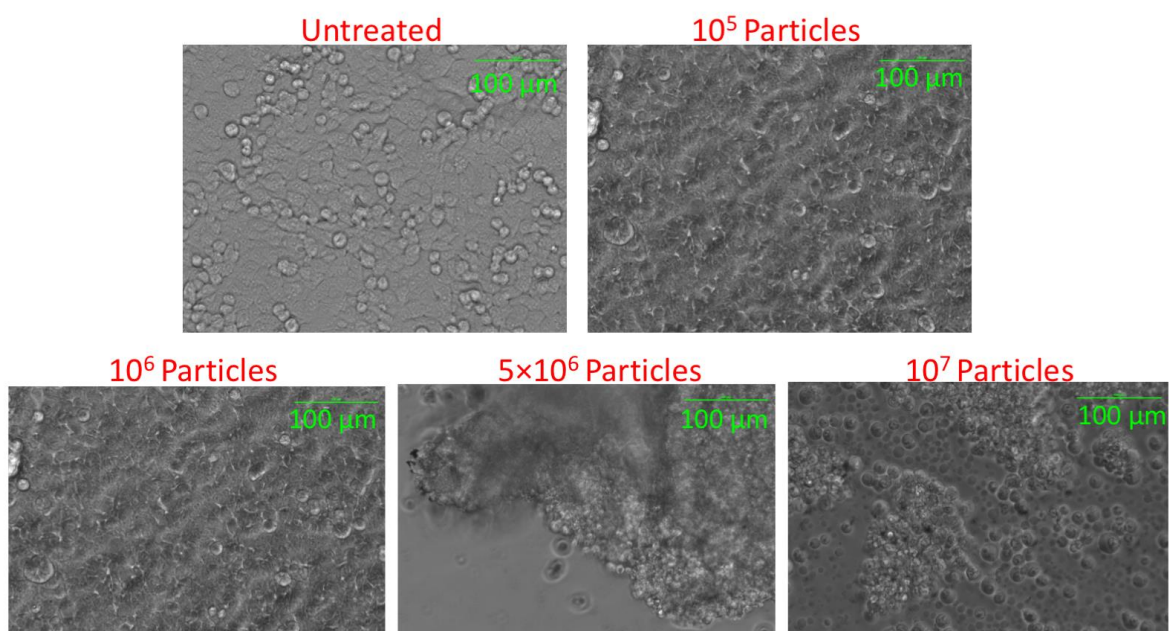
Figure 6.5. The brightfield image of the HCT-116 colon cancer cells after being incubated with various concentrations of cholate composite microparticles.

94

microparticles resulted in the detachment of the cell from the plate and their aggregation, which are all indicators of apoptosis. The same kind of results were confirmed once the viability of the cells after being incubated with the cholate composite microparticles was quantified. Incubation of the cells with 5×10^6 per well of a 24-well plates composite microparticles resulted in the death of nearly 80% of the cells in one hour (Figure 6.6a). The cell death was increased to nearly 100% when the concentration of the particles was 2-times increased to 10^7 particles/well (Figure 6.6a). Quantification of the viability of the cells after being incubated with the particles for different time-points confirmed that the apoptotic effect of the salts is time-dependent. While incubation of the cells with 5×10^6 per well for 1 h induced apoptosis in nearly 80% of the cells, this number was increased to around 95% when the incubation time was increased to 2 h (Figure 6.6b).
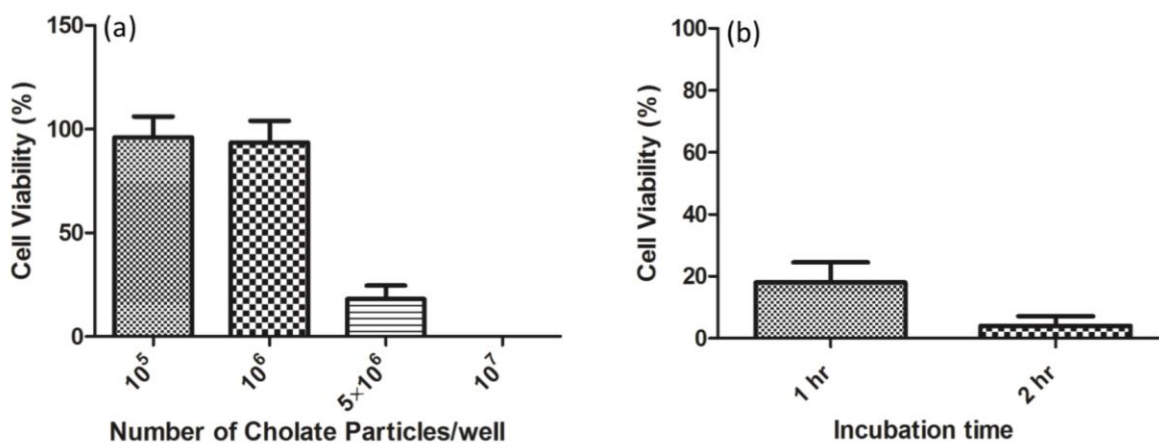
Figure 6.6. The viability of HCT-116 colon cancer cells after being incubated with (a) various concentrations of cholate-based composite microparticles for 1 h and (b) with 5×10^6 particles/well of a 24-well plate for various time points in media.

6.5. Discussion

Our results show that the composite bile salt microparticles fabricated via our bulk templating method will be able to lyse adipocytes and adipose tissue *in vitro* and induce apoptosis in cancer cells lines. These results confirm that our composite microparticles have the potential to be used

as controlled released systems where the therapeutic benefit of the bile acids/ salts has been proved, but their potential side effects and low efficacy has limited their utilization. In fact, our adipocyte lysis assays demonstrated that the composite microparticles are more efficient in inducing lipolysis than the salt solution with the same mass concentration, even if all the particles were degraded. This is potentially the result of the elevated local concentration near the cells when particles are used, compared to the well-mixed solution of salts. Inhibition of the lipolysis effect after using BSA in the system, the same as the observed effect with salts confirms that microparticles induce lipolysis with the same mechanism as the salts. The preincubation experiments also confirmed that the released cholate from particles is the inducer of lipolysis. The same lipolytic effect *in vitro* was also confirmed via *ex vivo* experimentation and inducing and incubation of the beef adipose tissue with composite microparticles. Our preliminary *in vivo* studies also demonstrated that particles were capable of reducing the weight of the obese mice over time. In our *in vitro* experiments, we also confirmed that our microparticles can induce apoptosis in cancer cell lines, the same as the salts. The lipolytic and cancer therapeutic potential of the particles will next be explored more in-depth within *in vivo* models.

6.6. Conclusions

Our results in the chapter have demonstrated that composite microparticles can be used as controlled release systems for local dissolution of fat or destroying the tumors. In the future experiments in our group, we will be testing our particle formulations *in vivo* to the obese or tumor-bearing mice models, to compare their lipolytic properties, and their apoptotic efficacy in cancer models with the salt formulations. We hypothesize that our particles will be able to maintain a sustained concentration of the bile salts in the injection site and induce a more efficient therapeutic benefit with less side effects compared to the salts. We will also attempt to conjugate the particles

with targeting ligands and test their performance as targeted drug delivery formulations. In the final stage, we will be loading our particles with anti-inflammatory or chemotherapy agents to benefit from combination therapy to reduce the potential side effects of the formulation.

CHAPTER 7: The Effect of Cosolvent on the Loading Efficiency and Release Profile of the Antibodies in the Emulsion Solvent Evaporation Technique

7.1. Publication Information

The data in this chapter is not yet published. This chapter has been composed as a manuscript, which will be submitted to Journal of Controlled Release in the coming weeks. The title will be "The cosolvent effect on the loading efficiency, release profile, and degradation kinetics of the antibodies in the emulsion solvent evaporation technique", with the author list: **Hanieh Safari**, Nicholas Kaczorowski, and Omolola Eniola-Adefeso.

7.2. Abstract

Antibodies are used as therapeutics for various disorders. However, the side effects limit their systemic administration and they need to be specifically delivered to the target site. Due to their hydrophilicity, the loading efficiency of antibodies via emulsion-based nanofabrication methods is normally very low. Thus, the fabrication technique, i.e., emulsion solvent evaporation, needs to be optimized to maximize the loading efficiency and prolong the release profile of the antibodies. In this work, we have investigated the effect of cosolvent on loading efficiency and release profile of anti-CD47, an antibody used for destroying the atherosclerotic plaque and cancer lesions, via emulsion solvent evaporation technique. Our results demonstrated that a minimum amount of a cosolvent with a minimal hydrophilicity can stabilize the antibody in the oil phase, and will significantly improve the loading efficiency and prolong the release profile of this

antibody. Amongst the cosolvents screened, ethyl acetate showed to be the optimum choice that could lead to a significant increase in the loading efficiency of the antibody in this technique.

7.3. Introduction

Due to their high selectivity and specificity, antibodies are widely used in the areas of diagnostics, therapeutics, and research.[156] Specifically, their wide variety of therapeutic applications makes them particularly useful for treating autoimmune, cardiovascular, and infectious diseases, cancer, poisoning, and asthma.[157] CD47 is a glycoprotein that binds to signal regulatory protein alpha (SIRPα) on the surface of myeloid cells and activates a signaling pathway that suppresses phagocytosis by macrophages.[158] Upregulation of CD47 on the surface of cancer stem cells and atherosclerotic plaques helps them bypass the immune system and is a significant contributor to the growth of the tumors and plaques.[158] Anti-CD47 therapy has been recently used to block the "do not eat" signal expressed on the surface of the cancer cells and atherosclerotic plaques, to allow macrophages and neutrophils to clear them and thus, subsequently destroy the tumor or the plaque.[158,159] However, the systemic administration of this antibody will impose the risk of blocking CD47 on healthy tissues and imposing unwanted side effects.[160] Indeed, studies in mice have shown that the systemic administration of CD47 will lead to a significant drop in the number of circulating neutrophils.[161] This can lead to serious adverse effects in humans, as neutrophils are the most abundant leukocytes in circulation and comprise about 50-70% of the blood leukocytes and are the first responders in case of an injury or inflammation.[85,162] Thus, in order to be able to use anti-CD47 mediated therapy in clinical applications without imposing undesired side effects, specific delivery to the target site is essential.

Targeted drug delivery has long been used as an alternative method for administering these drugs to achieve specific delivery and minimize the unwanted side effects.[17] Unlike bile salt particles that are primarily composed of the therapeutic, in most of the cases, the therapeutic needs to be loaded within a carrier matrix. Biodegradable polymers, specifically poly(lactic-co-glycolic acid), PLGA, in this case, have been proven to be an effective drug carrier as they allow for sustained drug release over days or even weeks and minimize off-target delivery of the drug.[163] Various methods have been previously used for the encapsulation of the hydrophilic entities such as anti-CD47 within biodegradable particles, i.e., spray-drying, double emulsion solvent evaporation technique, and coacervation.[164] Double emulsion solvent evaporation technique is the most commonly used method to make drug-loaded particles.[163] However, the diffusion of the loaded entity to the outer water phase will limit the encapsulation efficiency of drugs and speed up their drug release profile.[165] The steep release of the antibodies from particulate carriers fabricated via this technique limits their performance of the efficacy for clinical applications a maintained dosage is required for achieving the desired therapeutic benefit.[52] Additionally, due to the high cost of antibodies, their loading efficiency within polymeric particles must be maximized to minimize drug loss during the fabrication and, thus, the increase in the cost of the therapeutic formulation.[156,166] As a result, it is essential to optimize the fabrication procedure to increase the loading efficiency and prolong the circulation time of the particles fabricated via this technique.

The utilization of water-miscible cosolvents in the emulsion solvent evaporation technique has previously been used to improve the solubility of hydrophilic agents within the oil phase of the emulsions and to increase the droplet solidification and particle formation rate.[167] As a result, utilization of a cosolvent has been shown to improve the loading efficiency of the hydrophilic agents via the emulsion solvent evaporation technique.[167–170] Additionally, the utilization of

cosolvents have been shown to lead to a more uniform drug distribution within carriers, and thus a closer to linear release profile of the loaded cargo.[167] However, different cosolvents have not been investigated simultaneously to find out how the cosolvent properties will change the release profile and loading efficiency of the loaded therapeutic. Here in this chapter, we have investigated the loading efficiency of anti-CD47 within PLGA nanoparticles fabricated via a double emulsion solvent evaporation technique. Our results demonstrated that ethyl acetate is the optimum choice of the cosolvent, which leads to the highest loading efficiency and the most prolonged release profile. We also investigated the effect of the cosolvent ratio and antibody to polymer ratio. Our results show that increasing the cosolvent ratio and antibody to polymer ratio beyond a threshold will lower the loading efficiency of the antibody. The results of this study can be used to optimize the conditions for loading hydrophilic entities in the emulsion solvent evaporation technique, which can then be used in *in vivo* studies to increase the therapeutic efficacy of loaded drugs.

7.4. Results

7.4.1. Particle Fabrication

Particles were fabricated using various cosolvents, i.e., ethanol, methanol, ethyl acetate, and acetonitrile in the system. As represented in Figure 7.1, the presence of the cosolvent did not alter the surface morphology of particles, and the particles had a relatively smooth surface morphology for all the trials. The size of the particles measured from SEM images is summarized in Table 7.1. As Table 7.1 shows, the particles had a similar average diameter and size distribution in the presence of the various cosolvents. Thus, it can be concluded that the presence of various cosolvents did not change the physical properties of particles.
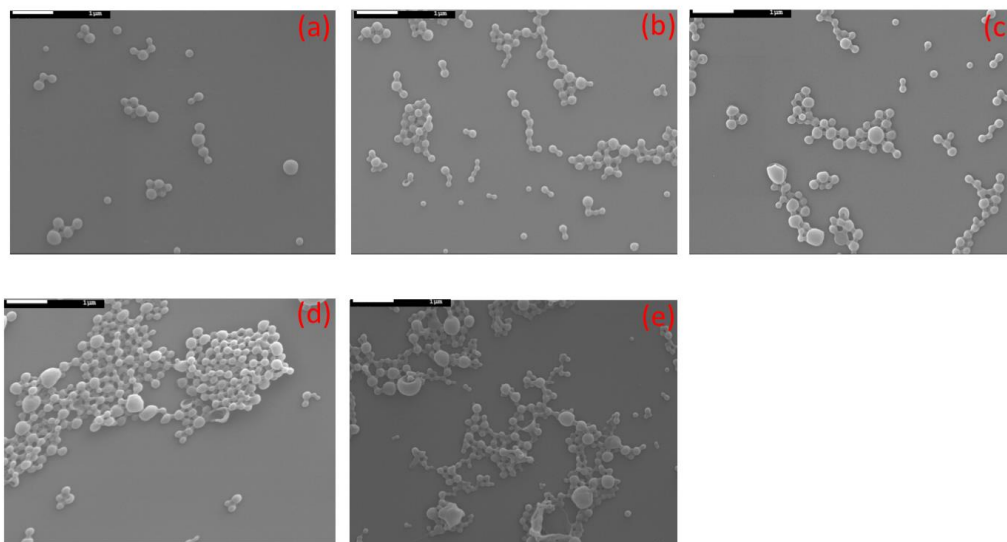
Figure 7.1. The SEM image of the anti-CD47-loaded nanoparticles fabricated in the presence of (a) No cosolvent, (b) Ethanol, (c) Methanol, (d) Acetonitrile, and (e) Ethyl Acetate as the cosolvent. The scale bars are all 1μm in size.

7.4.2. Effect of the cosolvent choice on loading efficiency and release profile of antibodies

In an attempt to increase the loading efficiency and prolong the release profile of the cargo, we utilized different cosolvents to stabilize anti-CD47 in the oil phase of the double emulsion solvent evaporation technique. When the loading efficiency of the antibody was quantified in the presence of various cosolvents, we demonstrated that a careful choice of cosolvent could lead to a significant increase in loading efficiency. As shown in Figure 7.2a, using cosolvents with the capability of forming hydrogen bonds such as ethanol and methanol will lower the antibody loading efficiency with respect to the trials with no cosolvent from about 60% to less than 20%. However, using cosolvents with minimal hydrophilicity such as acetonitrile and ethyl acetate improved the loading efficiency, with ethyl acetate leading to a nearly 100% loading efficiency (Figure 7.2a). These results are in line with the previous studies, which have demonstrated a decrease in the loading efficiency of highly water-soluble cargos by using alcohols as cosolvents, while more hydrophobic cosolvents were shown to improve the loading efficiency.[170] Interestingly enough, when the

102

Cosolvent Choice	Size (nm)
No cosolvent	220 ± 70
Ethanol	180 ± 40
Methanol	240 ± 70
Ethyl Acetate	200 ± 60
Acetonitrile	180 ± 50

Table 7.1. The average size of anti-CD47 loaded PLGA nanoparticle fabricated in presence of different cosolvents.

release profile of the antibody from the nanoparticles fabricated in the presence of different cosolvents was investigated, ethyl acetate resulted in the most prolonged release. The particles fabricated in the presence of ethanol demonstrated the fastest release (Figure 7.2b). While about 500 h was required for the release of 50% of the cargo when ethyl acetate was used as the cosolvent, this was decreased to about 100 h or less for other cosolvent systems, confirming a more sustained release via doping the oil phase solvent with ethyl acetate, which can lead to an increased loading efficiency of the particles.
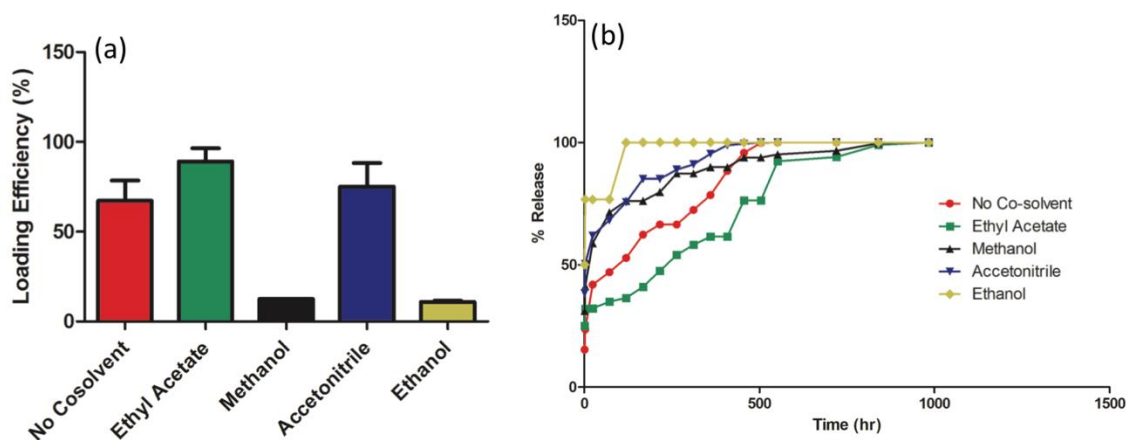
Figure 7.1. (a) Loading efficiency and (b) release profile of anti-CD47 from PLGA nanoparticles fabricated via double emulsion solvent evaporation technique in the presence of various cosolvents. 0.5 µg total antibody was used in the fabrication system per 50 mg of PLGA.

7.4.3. Effect of the theoretical antibody loading and cosolvent fraction on loading efficiency

After confirming that ethyl acetate is the optimum choice of cosolvent for loading anti-CD47 within biodegradable polymeric nanoparticles, we investigated the impact of the cosolvent fraction and the total amount of the loaded antibody on loading efficiency in the emulsion solvent evaporation technique. Our results demonstrated that for a fixed cosolvent choice and antibody loading, increasing the fraction of ethyl acetate in the oil phase above a threshold will significantly decrease the loading efficiency of the antibody (Figure 7.3). When the ratio of ethyl acetate in the oil phase was set at 25%, the loading efficiency decreased to around 30%, while this value was nearly 100% for lower cosolvent fractions. These results show that in order to achieve maximum loading, a minimum amount of cosolvent is required to stabilize the antibody in the oil phase, and a further increase in the cosolvent fraction will lead to a significant decrease in loading efficiency.
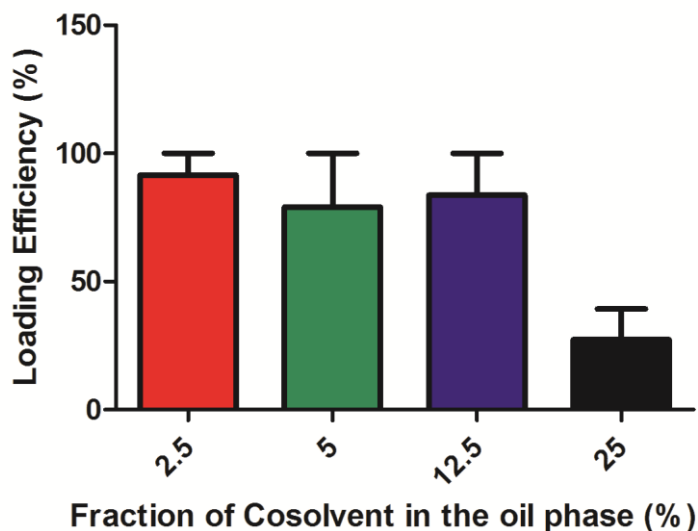
Figure 7.3. Anti-CD47 loading efficiency within PLGA nanoparticles fabricated via double emulsion solvent evaporation technique as a function of the fraction of ethyl acetate cosolvent in the oil phase.
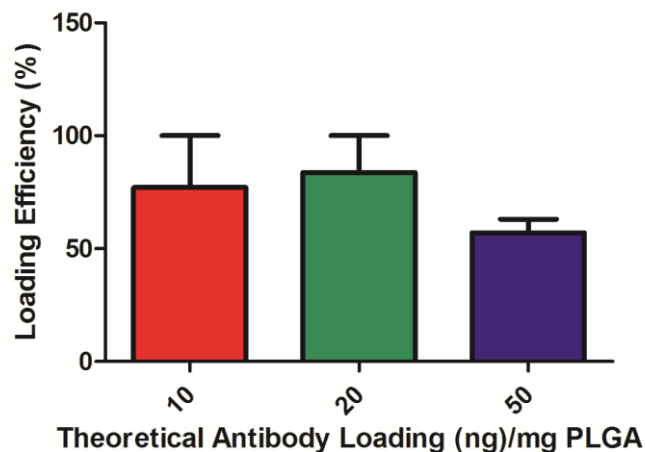
Figure 7.4. The loading efficiency of PLGA in anti-CD47-loaded PLGA nanoparticles fabricated via double emulsion solvent evaporation technique as a function of the total mass of the loaded antibody.

In a separate set of experiments, we investigated the effect of the total amount of the loaded antibody on its loading efficiency. As represented in Figure 7.4, increasing the total antibody loading will lower the loading efficiency, which is expected due to the higher concentration gradient of the antibody between the emulsion droplets and the outer water phase, leading to increased loss of the antibody to the outer water phase during the fabrication.

7.5. Discussion

In this chapter, we looked into how utilization of different cosolvents will affect the loading efficiency of antibodies within the PLGA nanoparticles fabricated via double emulsion solvent evaporation technique. Our results demonstrated that the utilization of a cosolvent to stabilize the antibody in the water phase would help to improve the antibody loading efficiency. While the surface morphology and average size of particles were not highly affected by choice of the cosolvent, the cosolvent selection is a significant contributor to the loading efficiency and the release profile of the hydrophilic cargos. Our results demonstrated that polar cosolvents with a minimum hydrophilicity like ethyl acetate and acetonitrile, are the optimal choice for acquiring

the maximum loading efficiency and the most prolonged release profile. There are three important factors that dictate the how the loading efficiency of the hydrophilic entities are affected by choice of the cosolvent, i.e., the stabilization of the antibody within the oil phase, the diffusion of the drug to the water phase via the cosolvent, and the solidification rate of the emulsion droplets.[170] While a minimum cosolvent polarity is required to stabilize the antibody in the oil phase, a further increase in the water miscibility of the cosolvent will result in a significant partitioning of the loaded cargo to the outer water phase, which would lead to a decreased loading efficiency. These results were confirmed with the experiments where the effect of the cosolvent fraction on the loading efficiency was investigated. For the optimum choice of the cosolvent, increasing the fraction of the cosolvent beyond a threshold lowered the loading efficiency, confirming that passing the minimum threshold required for stabilization of the antibody within the oil phase will enhance the diffusion of the antibody to the outer water phase and lower the loading efficiency.

After optimization of the choice of the cosolvent and its fraction, we investigated the effect of the total loaded cargo on the loading efficiency. As expected, increasing the total amount of the loaded antibody will lower the loading efficiency. This is the consequence of an increased concentration gradient between the emulsion droplets and the water phase as the concentration of the loaded antibody increases, which will lead to increased diffusion of the antibody out to the water phase, according to the Fick's diffusion law and thus lower efficiency. These results demonstrate that when the high dosages of the loaded antibody are required, the choice of the cosolvent used in the emulsion solvent evaporation technique becomes an important factor in preventing the loss of the antibody to the outer water phase. To summarize, the results of this chapter show that the careful tuning of the fabrication conditions in the emulsion solvent evaporation technique, including the cosolvent selection, can be used to optimize the loading and

release properties of hydrophilic entities within biodegradable nanoparticles.

7.6. Conclusions

The results of this chapter demonstrated that doping the oil phase of an emulsion solvent evaporation technique with a cosolvent can be used as a strategy to increase the loading efficiency and prolong release profile of the antibodies. We showed that the usage of a minimal amount of polar cosolvents with minimum hydrophilicity will significantly improve the loading efficiency and prolong the release profile of the anti-CD47. This technique can be used to optimize the formulation of antibody-loaded nanoparticles to maximize their therapeutic efficacy within *in vitro* and *in vivo* systems. In our future work, we will be developing a theoretical diffusion-based model to confirm our experimental results and help us predict the optimum choice for loading various antibodies within different polymer matrixes. We will be using our anti-CD47 loaded particles in the *in vivo* models to investigate the efficacy of various formulations in destroying the atherosclerotic plaque.

CHAPTER 8: Conclusions and Future Directions

8.1. Conclusions

Despite decades of research, very few drug delivery systems have translated to clinical use. One of the reasons for this is the lack of a thorough understanding of the interaction of particles with different parts of the human body, and how those interactions affect the efficacy of the carriers. Optimization of the physical design parameters of particles can be a strategy to improve the performance of the particles for different therapeutic applications, which subsequently speeds up the translation of the drug carriers to the clinic. Shape is one of the critical design parameters that have recently been shown to influence the performance of drug carriers. Different studies have provided evidence demonstrating that the alterations in the particle shape can improve their *in vivo* performance. However, a lot still needs to be understood regarding the impact of shape on the performance of the micro/nanoparticles in different disease models, and their interaction with various cells and organs within the body. One of the most important reasons for the limited understanding of the *in vivo* performance of non-spherical particles is the lack of a simple and scalable method for the production of the non-spherical particles in large quantities. In this thesis, I worked to develop novel emulsion-based methods to fabricate non-spherical biodegradable particles in large quantities, which were then used to investigate their interaction with various blood components and their therapeutic performance and in various disease models.

In Chapter 3, we investigated the impact of shape and aspect ratio on the phagocytosis of particles by different leukocyte populations in human and mice blood. Our results showed that in both humans and mice, neutrophils would preferentially get associated with elongated particles

108

both *in vitro* and *in vivo*, which is opposite of the trend observed for mononuclear phagocytes, i.e., monocytes, macrophages, and dendritic cells. These results open up an opportunity for selective targeting of neutrophils for the treatment of inflammatory conditions.

In Chapter 4, we developed a modified emulsion-based method for fabricating rod-shaped polymeric microparticles in large quantities. The conventional emulsion solvent evaporation technique was modified by introducing a surface-active molecule to lower the interfacial tension of the system and enable stretching of the emulsion droplets via shear. The previously developed method was changed to a two-step protocol, where the droplet formation and stretching steps were separated. After the initial formation of the droplets and evaporation of the solvent and when the droplets start translating into a gel form, a high-viscosity solution was introduced to the system to boost up the capillary number and enable stretching of the previously formed droplets. Via these changes, and the optimization of the oil-phase solvent and the surface-active molecule choices, I was able to fabricate PLGA rods with the major axis sizes as small as 3 µm, which is the size range of interest for vascular targeting applications, with the yield of 80% or higher. We also showed that these fabricated rods could be successfully loaded with dyes as a model therapeutic. We investigated the impact of the shape on the release profile of the particles, which showed that using elongated particles with a high surface area to volume ratio will speed up the release profile of the loaded cargo. We were also able to successfully conjugate the surface of the particles with targeting ligands and show that they would be able to bind to an inflamed vasculature both *in vitro* and *in vivo*. We confirmed that the particles were able to successfully navigate through the mouse bloodstream without causing any occlusion in smaller capillaries, which enables their usage as suitable candidates for vascular targeting applications.

In Chapter 5, we developed a new emulsion-based bulk templating method to fabricate microparticles composed of bile salts. Gold ion was used as the templating agent and its reduction at the oil-water interface enabled the formation of cholate/deoxycholate microparticles. We were able to control the size of particles by changing the concentration of the surfactant, sodium cholate, in the water phase. We could also show that these particles were able to be loaded with hydrophilic agents such as rhodamine for combination therapy applications and could degrade via surface erosion to release bile salts into the solution. The results of this chapter can open up a new avenue for developing new metal-based templating techniques to make new microparticulate formulations. It also introduces new controlled release systems made of bile salts to minimize the side effects when these molecules are used as therapeutics.

In Chapter 6, we explored the utilization of bile salts particles as therapeutic agents for fat dissolution and cancer treatment. We showed that our fabricated microparticles were able to successfully lyse adipocytes *in vitro* in a concentration and time-dependent manner. We also showed that the particles are more efficient than the salts in their cell-lytic properties, potentially due to the increased local concentration when using the particles. We also showed that similar to the salts, the lytic properties of the particles will be inhibited in the presence of albumin, which confirms they work with the same mechanism as the salts. Additionally, we demonstrated that particles would be able to induce apoptosis in colon cancer cells *in vitro*, which opens up a new opportunity for utilizing them for destroying tumor lesions.

In Chapter 7, we optimized the emulsion solvent evaporation technique to maximize the loading efficiency and prolong the release profile of the antibodies and hydrophilic agents within polymeric nanoparticles. We confirmed that the utilization of a minimum amount of a minimally

hydrophilic cosolvent to stabilize the antibody in the oil phase would increase the loading efficiency and prolong the release profile of the antibody.

In conclusion, we have demonstrated that the conventional emulsion-based methods can be modified to fabricate novel biodegradable particle formulations. These new formulations can be used as therapeutics in different disease models to enhance their treatment status.

8.2. Future Directions

The methods developed in this thesis can open up new opportunities for developing novel particle fabrication systems. The controlled released systems developed in this method can as well be tested and used as therapeutics in different disease models. Some of the potential areas of interest for future research are listed below.

(1) Modeling emulsions and droplet deformation and stretching to fully understand various factors contributing to the stretching of the emulsion droplets. These studies can expand our knowledge of droplet deformation and enable fabrication of elongated particles made of other polymers. These models can also help us fabricate smaller and more uniform rods and have accurate control over the size and aspect ratio of the polymeric particles.

(2) Investigating the potential of combining our two-step protocol with other fabrication methods such as electrohydrodynamic co-spinning in order to achieve more uniform and complex particle and multi-compartmental particles.

(3) Utilizing rod-shaped particles in acute inflammatory conditions where neutrophils are the major contributors to the severity of the disorder.

(4) Performing a mechanistic study on the reason behind the difference in response of different leukocyte populations to variations in the shape of polymeric particles. Imaging studies and theoretical simulations of cell mechanics can be helpful in this respect.

(5) Studying the theoretical mechanism behind the metal-assisted templating at the oil-water interface. This can help us understand the formation process of bile salt particles.

(6) Modification of the metal-assisted templating method to fabricate particles made of other bile salts or therapeutics salts and achieve control over the particle design parameters such as their degradation kinetics, their size, and their shape.

(7) Conjugation of the surface of bile salt particles with targeting ligands to be able to use them to specifically target different diseases.

(8) Loading bile salt particles with different anti-inflammatory and chemotherapy agents to enable their potential use for combination therapy application in various disease models and reduce their potential side effects.

(9) Using bile salt particles in different *in vivo* systems where their therapeutic value has been proved, such as liver diseases, obesity, and colon cancer, to minimize the side effects associated with the therapeutic formulation.

REFERENCES

1.   Safari, H., Lee, J. K. & Eniola-adefeso, O. Effects of shape, rigidity, size, and flow on targeting. Nanoparticles for Biomedical Applications (Elsevier Inc., 2020).

2.   Calzoni, E. et al. Biocompatible Polymer Nanoparticles for Drug Delivery Applications in Cancer and Neurodegenerative Disorder Therapies. *J. Funct. Biomater.* **10**, 4 (2019).

3.   Joshi, V. B., Geary, S. M. & Salem, A. K. Biodegradable Particles as Vaccine Delivery Systems : Size Matters. *AAPS J.* **15**, 13–16 (2013).

4.   Gumargalieva, K. Z., Horak, D., Zaikov, G. E. Biodegradable Polymeric Microparticles in Biomedical Applications Biodegradable Polymeric Micro particles in Biomedical Applications. *Int. J. Polym. Mater.* **42**, 83–117 (1998).

5.   Oliveira, M. B. & Mano, J. F. Polymer-Based Microparticles in Tissue Engineering and Regenerative Medicine. *Biotechnol. Prog.* **27**, 897–912 (2011).

6.   Kaul, S., Gulati, N., Verma, D., Mukherjee, S. & Nagaich, U. Role of Nanotechnology in Cosmeceuticals : *A Review of Recent Advances. J. Pharm.* (2018).

7.   Wang, L. & Liu, X. Sustained Release Technology and Its Application in Environmental Remediation : A Review. *Int. J. Environ. Res. Public Health* **16**, 2153 (2019).

8.   Han, J., Shi, J., Xie, Z., Xu, J. & Guo, B. Synthesis, Properties of Biodegradable Poly(Butylene Succinate- co -Butylene 2-Methylsuccinate) and Application for Sustainable Release. *Materials* **12**, 1507 (2019).

9.   Kozlowska, J., Prus, W. & Stachowiak, N. Microparticles based on natural and synthetic polymers for cosmetic applications. *Int. J. Biol. Macromol.* **129**, 952–956 (2019).

10.   Roy, A., Singh, S. K., Bajpai, J. & Bajpai, A. K. Controlled pesticide release from biodegradable polymers. *Cent. Eur. J. Chem.* **12**, 453–469 (2014).

11.   Kelley, W. J., Safari, H., Lopez-Cazares, G. & Eniola-Adefeso, O. Vascular-targeted nanocarriers: design considerations and strategies for successful treatment of atherosclerosis and other vascular diseases. *Wiley Interdiscip. Rev. Nanomedicine Nanobiotechnology* **8**, (2016).

12.   Singh, R. & Lillard Jr, J. W. Nanoparticle-based targeted drug delivery. *Exp. Mol. Pathol.* **86**, 215–223 (2009).

13.   Natarajan, J. V, Nugraha, C., Ng, X. W. & Venkatraman, S. Sustained-release from nanocarriers : a review. *J. Control. Release* **193**, 122–138 (2014).

14.   Park, J. et al. Intravascular innate immune cells reprogrammed via intravenous nanoparticles to promote functional recovery after spinal cord injury. *Proc. Natl. Acad. Sci.* **116**, 14947–14954 (2019).

15.   Saito, E. et al. Designing drug-free biodegradable nanoparticles to modulate inflammatory monocytes and neutrophils for ameliorating inflammation. *J. Control. Release* **300**, 185–196 (2019).

16.   Pridgen, E. M., Langer, R. & Farokhzad, O. C. Biodegradable , polymeric nanoparticle delivery systems for cancer therapy. *Nanomedicine* **2**, 669–680 (2007).

17.   Tiwari, G. et al. Drug delivery systems: An updated review. *Int. J. Pharm. Investig.* **2**, 2 (2012).

18.   Zdanowicz, M. & Chroboczek, J. Virus-like particles as drug delivery vectors. *ACTA Biochim. Pol.* **63**, 469–473 (2016).

19.   Chauhan, A. S. Dendrimers for Drug Delivery. *Molecules* **23**, 938 (2018).

20.   Papachristos, A., Pippa, N. & Demetzos, C. Antibody-drug conjugates : a mini-review . The synopsis of two approved medicines. *Drug Deliv.* **23**, 1662–1666 (2016).

21.   Park, K. Drug Delivery Research: The Invention Cycle. *Mol. Pharm.* **13**, 2143–2147 (2017).

22.   Charoenphol, P., Huang, R. B. & Eniola-adefeso, O. Potential role of size and hemodynamics in the efficacy of vascular-targeted spherical drug carriers. *Biomaterials* **31**, 1392–1402 (2010).

23.   Champion, J. A & Mitragotri, S. Role of target geometry in phagocytosis. *Proc. Natl. Acad. Sci. U. S. A.* **103**, 4930–4934 (2006).

24.   Champion, J. A., Walker, A. & Mitragotri, S. Role of Particle Size in Phagocytosis of Polymeric Microspheres. *Pharm. Res*. **25**, 1815–1821 (2008).

25.   Namdee, K., Sobczynski, D. J., Onyskiw, P. J. & Eniola-adefeso, O. Differential Impact of Plasma Proteins on the Adhesion Efficiency of Vascular-Targeted Carriers (VTCs) in Blood of Common Laboratory Animals. *Bioconjugate Chem.* **26**, 2419–2428 (2015).

26.   Schaffler, M. et al. Serum protein identification and quantification of the corona of 5 , 15 and 80 nm gold nanoparticles. *Nanotechnology* **24**, 265103 (2013).

27.   Klingberg, H., Loft, S., Oddershede, L. B. & Møller, P. The influence of flow, shear stress and adhesion molecule targeting on gold nanoparticle uptake in human endothelial cells. *Nanoscale* **7**, 11409–11419 (2015).

28.   Doshi, N. et al. Flow and Adhesion of Drug Carriers in Blood Vessels Depend on their Shape: A Study using Model Synthetic Microvascular Networks. *J. Control. Release* **146**, 196-200 (2010).

29.   Thompson, A. J., Mastria, E. M. & Eniola-Adefeso, O. The margination propensity of ellipsoidal micro/nanoparticles to the endothelium in human blood flow. *Biomaterials* **34**, 5863–5871 (2013).

30.   Fish, M. B., Thompson, A. J., Fromen, C. A. & Eniola-adefeso, O. Emergence and Utility of Nonspherical Particles in Biomedicine. *Ind. Eng. Chem. Res*. **54**, 4043–4059 (2015).

31.   Moghimi, S. M., Porter, C. J., Muir, L., Illum, L. & Davis, S. Non-phagocytic uptake of intravenously injected microspheres in rat spleen : Influence of particle size and hydrophilic coating. Biochem. *Biophys. Res. Commun.* **177**, 861–866 (1991).

32.   Bilzer, M., Roggel, F. & Gerbes, A. L. Role of Kupffer cells in host defense and liver disease. *Liver Int*. **26**, 1175–1186 (2006).

33.   Toth, C. A. & Thomas, P. Special Article Liver Endocytosis and Kupffer Cells. *Hepatology* **1**, 255–266 (1992).

34.   He, Q., Zhang, Z., Gao, F., Li, Y. & Shi, J. In vivo Biodistribution and Urinary Excretion of Mesoporous Silica Nanoparticles : Effects of Particle Size and PEGylation. *Small* **7**, 271–280 (2011).

35.   Mebius, R. E. & Kraal, G. Structure and Function of the Spleen. *Nat. Rev. Immunol.* **5**, 606–616 (2005).

36.   Fish, M. B., Thompson, A. J., Fromen, C. a. & Eniola-Adefeso, O. Emergence and Utility of Nonspherical Particles in Biomedicine. *Ind. Eng. Chem. Res.* **54**, 4043–4059 (2015).

37.   Choi, H. S. et al. Renal Clearance of Nanoparticles. *Nat. Biotechnol.* **25**, 1165–1170 (2007).

38.   Jones, S. W. et al. Nanoparticle clearance is governed by Th1 / Th2 immunity and strain background. *J. Clin. Invest.* **123**, (2013).

39.   Fromen, C. A. et al. Neutrophil − Particle Interactions in Blood Circulation Drive Particle Clearance and Alter Neutrophil Responses in Acute Inflammation. *ACS Nano* **11**, 10797–10807 (2017).

40.   Keshavan, S. et al. Nano-bio interactions : a neutrophil-centric view. *Cell Death Dis.* **10**, 1-11 (2019).

41.   Kelley, W. J., Fromen, C. A., Lopez-cazares, G. & Eniola-adefeso, O. PEGylation of model drug carriers enhances phagocytosis by primary human neutrophils. *Acta Biomater.* **79**, 283–293 (2018).

42.   Maiolo, D., Del Pino, P., Parak, W. J. & Baldelli Bombelli, F. Nanomedicine delivery : does protein corona route to the target or off road ? *Nanomedicine* **10**, 3231–3247 (2015).

43.   Tenzer, S. et al. Nanoparticle size is a critical physicochemical determinant of the human blood plasma corona: A comprehensive quantitative proteomic analysis. *ACS Nano* **5**, 7155–7167 (2011).

44.   Sobczynski, D. J. et al. Drug Carrier interaction with blood: a critical aspect for high-efficient vascular-targeted drug delivery systems. *Ther. Deliv.* **6**, 915–934 (2016).

45.   Sobczynski, D. J. et al. Plasma protein corona modulates the vascular wall interaction of drug carriers in a material and donor specific manner. *PLoS One* **9**, e107408 (2014).

46.   Crowl, L. M. & Fogelson, A. L. Computational model of whole blood exhibiting lateral platelet motion induced by red blood cells. *Int. j. numer. method. biomed. eng.* **26**, 471–487 (2010).

47.   Kumar, A. & Graham, M. D. Mechanism of Margination in Confined Flows of Blood and Other Multicomponent Suspensions. *Phys. Rev. Lett.* **109**, 108102 (2012).

48.   Müller, K., Fedosov, D. a & Gompper, G. Margination of micro- and nano-particles in blood flow and its effect on drug delivery. *Sci. Rep.* **4**, (2014).

49.   Cooley, M. et al. Influence of particle size and shape on their margination and wall-adhesion: Implications in drug delivery vehicle design across nano-to-micro scale. *Nanoscale* **10**, 15350–15364 (2018).

50.   Charoenphol, P. et al. Targeting therapeutics to the vascular wall in atherosclerosis-carrier size matters. *Atherosclerosis* **217**, 364–70 (2011).

51.   Fu, Y. & Kao, W. J. Drug Release Kinetics and Transport Mechanisms of Non-degradable and Degradable Polymeric Delivery Systems. *Expert Opin. Drug Deliv.* **7**, 429–444 (2011).

52.   Sethi, M. et al. Effect of drug release kinetics on nanoparticle therapeutic efficacy and toxicity. *Nanoscale* **6**, 2321–2327 (2014).

53.   Golomb, G., Fisher, P. & Rahamim, E. The relationship between drug release rate, particle size and swelling of silicone matrices. *J. Control. Release* **12**, 121–132 (1990).

54.   Berkland, C., King, M., Cox, A., Kim, K. & Pack, D. W. Precise control of PLG microsphere size provides enhanced control of drug release rate. *J. Control. Release* **82**, 137–147 (2002).

55.   Lin, X., Yang, H., Su, L., Yang, Z. & Tang, X. Effect of size on the in vitro / in vivo drug release and degradation of exenatide-loaded PLGA microspheres. *J. Drug Deliv. Sci. Technol.* **45**, 346–356 (2018).

56.   Chen, W., Palazzo, A., Hennink, W. E. & Kok, R. J. Effect of Particle Size on Drug Loading and Release Kinetics of Gefitinib-Loaded PLGA Microspheres. *Mol. Pharm.* **14**, 459–467 (2017).

57.   Fattahi, P., Borhan, A. & Abidian, M. R. Microencapsulation of Chemotherapeutics into Monodisperse and Tunable Biodegradable Polymers via Electrified Liquid Jets : Control of Size , Shape , and Drug Release. *Adv. Mater.* **25**, 4555–4560 (2013).

58.   Champion, J. A. & Mitragotri, S. Shape Induced Inhibition of Phagocytosis of Polymer Particles. *Pharm. Res.* **26**, 244–249 (2009).

59.   Sharma, G. et al. Polymer particle shape independently influences binding and internalization by macrophages. *J. Control. Release* **147**, 408–412 (2010).

60.   Yang, K. & Ma, Y. Computer simulation of the translocation of nanoparticles with different shapes across a lipid bilayer. *Nat. Nanotechnol*. **5**, 579 (2010).

61.   Geng, Y. A. N. et al. Shape effects of filaments versus spherical particles in flow and drug delivery. *Nat. Nanotechnol.* **2**, 249–255 (2007).

62.   Janát-amsbury, M. M., Ray, A., Peterson, C. M. & Ghandehari, H. Geometry and surface characteristics of gold nanoparticles influence their biodistribution and uptake by macrophages. *Eur. J. Pharm. Biopharm.* **77**, 417–423 (2011).

63.   Lundqvist, M. et al. Nanoparticle size and surface properties determine the protein corona with possible implications for biological impacts. *Proc. Natl. Acad. Sci.* **105**, 14265–14270 (2008).

64.   Walkey, C. D., Olsen, J. B., Guo, H., Emili, A. & Chan, W. C. Nanoparticle Size and Surface Chemistry Determine Serum Protein Adsorption and Macrophage Uptake. *J. Am. Chem. Soc.* **134**, 2139–2147 (2012).

65.   Deng, Z. J. et al. Differential plasma protein binding to metal oxide nanoparticles. *Nanotechnology* **20**, 455101 (2009).

66.   Ma, Z., Bai, J., Wang, Y. & Jiang, X. Impact of Shape and Pore Size of Mesoporous Silica Nanoparticles on Serum Protein Adsorption and RBCs Hemolysis. *ACS Appl. Mater. Interfaces* **6**, 2431–2438 (2014).

67.   García-álvarez, R., Hadjidemetriou, M., Sánchez-iglesias, A., Liz-marzán, L. M. & Kostarelos, K. In vivo formation of protein corona on gold nanoparticles. The effect of their size and shape. *Nanoscale* **10**, 1256–1264 (2018).

68.   Müller, K., Fedosov, D. a & Gompper, G. Margination of micro- and nano-particles in blood flow and its effect on drug delivery. *Sci. Rep*. **4**, 4871 (2014).

69.   Namdee, K. et al. In vivo evaluation of vascular-targeted spheroidal microparticles for imaging and drug delivery application in atherosclerosis. *Atherosclerosis* **237**, 279–286 (2014).

70.   Shum, H. C. et al. Droplet microfluidics for fabrication of non-spherical particles. *Macromol. Rapid Commun.* **31**, 108–118 (2010).

71. Wang, J. T., Wang, J. & Han, J. J. Fabrication of advanced particles and particle-based materials assisted by droplet-based microfluidics. *Small* **7**, 1728–1754 (2011).

72. Jarai, B. M., Kolewe, E. L., Stillman, Z. S., Raman, N. & Fromen, C. A. Polymeric Nanoparticles. *Nanoparticles for Biomedical Applications* (Elsevier Inc., 2020).

73. Govender, T., Stolnik, S., Garnett, M. C., Illum, L. & Davis, S. S. PLGA nanoparticles prepared by nanoprecipitation: Drug loading and release studies of a water soluble drug. *J. Control. Release* **57**, 171–185 (1999).

74. Patel, B., Patel, J. & Chakraborty, S. Review of Patents and Application of Spray Drying in Pharmaceutical, Food and Flavor Industry. *Recent Pat. Drug Deliv. Formul*. **8**, 63–78 (2014).

75. Deshmukh, R., Wagh, P. & Naik, J. Solvent evaporation and spray drying technique for micro- and nanospheres/particles preparation: A review. *Dry. Technol*. **34**, 1758–1772 (2016).

76. Li, M., Rouaud, O. & Poncelet, D. Microencapsulation by solvent evaporation: State of the art for process engineering approaches. *Int. J. Pharm*. **363**, 26–39 (2008).

77. Rosca, I. D., Watari, F. & Uo, M. Microparticle formation and its mechanism in single and double emulsion solvent evaporation. *J. Control. Release* **99**, 271–280 (2004).

78. Heslinga, M. J., Mastria, E. M. & Eniola-Adefeso, O. Fabrication of biodegradable spheroidal microparticles for drug delivery applications. *J. Control. Release* **138**, 235–242 (2009).

79. Safari, H., Adili, R., Holinstat, M. & Eniola-Adefeso, O. Modified two-step emulsion solvent evaporation technique for fabricating biodegradable rod-shaped particles in the submicron size range. *J. Colloid Interface Sci*. **518**, (2018).

80. Fish, M. B. et al. Exploring deformable particles in vascular-targeted drug delivery : Softer is only sometimes better. *Biomaterials* **124**, 169–179 (2017).

81. Kuo, R., Saito, E., Miller, S. D. & Shea, L. D. Peptide-Conjugated Nanoparticles Reduce Positive Co-stimulatory Expression and T Cell Activity to Induce Tolerance. *Mol. Ther*. **25**, (2017).

82. Miller, S. D., Karpus, W. J. & Davidson, T. S. Experimental Autoimmune Encephalomyelitis in the Mouse. *Current Protocols in Immunology* **88**,1–15 (2010).

83. Dale, D. C., Boxer, L. & Liles, W. C. The phagocytes : neutrophils and monocytes. *Blood* **112**, 935–945 (2008).

84. Wu, C., Hsieh, C., Huang, S., Lin, J. & Wang, T. In vivo Imaging Flow Cytometry of Human Leukocytes. *Opt. Life Sci*. BoW3A-2 (2017).

85. Aulakh, G. K. Neutrophils in the lung : B the first responders. *Cell Tissue Res*. **371**, 577–588 (2018).

86. Rao, A. N., Kazzaz, N. M. & Knight, J. S. Do neutrophil extracellular traps contribute to the heightened risk of thrombosis in inflammatory diseases? *World J. Cardiol*. **7**, 829–843 (2015).

87. Sônego, F., Alves-filho, J. C., Cunha, F. Q. & Alves-filho, C. Targeting neutrophils in sepsis Targeting neutrophils in sepsis. *Expert Rev. Clin. Immunol*. **10**, 1019-1028 (2014).

88. Jickling, G. C. et al. Targeting neutrophils in ischemic stroke : translational insights from experimental studies. *J. Cerebal Blood Flow Metab*. **35**, 888–901 (2015).

89. Beeh, K. M. & Beier, J. Handle with care : targeting neutrophils in chronic obstructive pulmonary disease and severe asthma ? *Clin. Exp. Allergy* **36**, 142–157 (2006).

90.   Getts, D. R. et al. Therapeutic Inflammatory Monocyte Modulation Using Immune-Modifying Microparticles. *Sci. Transl. Med.* **6**, 219ra7-219ra7 (2014).

91.   Leuschner, F. et al. Articles Therapeutic siRNA silencing in inflammatory monocytes in mice. *Nat. Biotechnol.* **29**, 1005 (2011).

92.   Kang, Y. S. et al. Novel C-C chemokine receptor 2 antagonists in metabolic disease : a review of recent developments. *Expert Opin. Investig. Drugs* **20**, 745-756 (2011).

93.   Holdren, J. Roche Exits RNAi Field , Cuts 4800 Jobs. *Science*, 1163-1163 (2010).

94.   Jeong, S. J. et al. Neurobiology of Disease Intravenous immune-modifying nanoparticles as a therapy for spinal cord injury in mice. *Neurobiol. Dis.* **108**, 73–82 (2017).

95.   Casey, L. M. et al. Cargo-less nanoparticles program innate immune cell responses to toll-like receptor activation. *Biomaterials* **218**, 119333 (2019).

96.   Handin, R. I., Lux, S. E. & Stossel, T. P. Structure function and functional disorders of the phagocyte system. in *Blood: Principle and Practice of Hematology* (Lippincott Williams & Wilkins, 2003).

97.   Anselmo, A. C. et al. Monocyte-mediated delivery of polymeric backpacks to inflamed tissues : a generalized strategy to deliver drugs to treat inflammation. *J. Control. Release* **199**, 29–36 (2015).

98.   Garcia, I. et al. Glycans as Biofunctional Ligands for Gold Nanorods: Stability and Targeting in Protein-Rich Media. *J. Am. Chem. Soc.* **137**, 3686–3692 (2015).

99.   Hu, C. J. et al. Erythrocyte membrane-camouflaged polymeric nanoparticles as a biomimetic delivery platform. *Proc. Natl. Acad. Sci.* **108**, 10980–10985 (2011).

100.   Bisso, P. W., et al. Nanomaterial Interactions with Human Neutrophils˜. *ACS Biomater. Sci. Eng.* **4**, 4255–4265 (2018).

101.   Richards, D. M. & Endres, R. G. How cells engulf : a review of theoretical approaches to phagocytosis. *Reports Prog. Phys.* **80**, 126601 (2017).

102.   Yoo, J. W, Chambers, E. & Mitragotri, S. Factors that Control the Circulation Time of Nanoparticles in Blood : Challenges , Solutions and Future Prospects. *Curr. Pharm. Des.* **16**, 2298–2307 (2010).

103.   Ross, G. D. & Vetvicka, V. CR3 (CD11b, CD18): a phagocyte and NK cell membrane receptor with multiple ligand specificities and functions. *Clin. Exp. Immunol.* **92**, 181–184 (1993).

104.   Kelley, W. J., Onyskiw, P. J., Fromen, C. A. & Eniola-Adefeso, O. Model Particulate Drug Carriers Modulate Leukocyte Adhesion in Human Blood Flows. *ACS Biomater. Sci. Eng.* **5**, 6530–6540 (2019).

105.   Huang, C. K. Protein Kinases in Neutrophils : A Review Protein Kinases in Neutrophils : A Review. Membr. *Biochem.* **8**, 61–79 (1989).

106.   Herant, M., Lee, C. Y, Dembo, M. & Heinrich, V. Protrusive Push versus Enveloping Embrace : Computational Model of Phagocytosis Predicts Key Regulatory Role of Cytoskeletal Membrane Anchors. *PLoS Comput. Biol.* **7**, e1001068 (2011).

107.   Heinrich, V. Controlled One-on-One Encounters between Immune Cells and Microbes Reveal Mechanisms of Phagocytosis. *Biophysj* **109**, 469–476 (2015).

108.   Barros-becker, F., Lam, P., Fisher, R. & Huttenlocher, A. Live imaging reveals distinct modes of neutrophil and macrophage migration within interstitial tissues. *J. Cell. Sci.* **130**, 3801–3808 (2017).

109. Champion, J. A., Katare, Y. K. & Mitragotri, S. Making polymeric micro- and nanoparticles of complex shapes. *Proc. Natl. Acad. Sci.* **104**, 11901–11904 (2007).

110. Williford, J. *et al.* Biomaterials Science Shape control in engineering of polymeric nanoparticles for therapeutic delivery. *Biomaterials Science* **3**, 894–907 (2015).

111. Rolland, J. P. *et al.* Direct Fabrication and Harvesting of Monodisperse , Shape-specific Nanobiomaterials. *J. Am. Chem. Soc.* **127**, 10096–10100 (2005).

112. Xu, S. *et al*. Generation of Monodisperse Particles by Using Microfluidics: Control over Size, Shape, and Composition. *Angew. Chemie* **44**, 724–728 (2005).

113. Dendukuri, D., Tsoi, K., Hatton, T. A. & Doyle, P. S. Controlled Synthesis of Nonspherical Microparticles Using Microfluidics. *Langmuir* **21**, 2113–2116 (2005).

114. Bhaskar, S., Hitt, J., Chang, S.-W. L. & Lahann, J. Multicompartmental Microcylinders. *Angew. Chemie Int. Ed*. **48**, 4589–4593 (2009).

115. Fan, Q. et al. Direct and controllable preparation of uniform PLGA particles with various shapes and surface morphologies. *Colloids Surfaces A Physicochem. Eng. Asp*. **500**, 177–185 (2016).

116. Heslinga, M. J., Willis, G. M., Sobczynski, D. J., Thompson, A. J. & Eniola-Adefeso, O. One-step fabrication of agent-loaded biodegradable microspheroids for drug delivery and imaging applications. *Colloids Surfaces B Biointerfaces* **116**, 55–62 (2014).

117. Li, R., Li, X., Liu, L., Zhou, Z. & Tang, H. High-Yield Fabrication of PLGA Non-Spherical Microarchitectures by Emulsion-Solvent Evaporation Method. *Macromolecular Rapid Communications*. **31**. 1981–1986 (2010).

118. Gupta, A. & Sbragaglia, M. Deformation and break-up of Viscoelastic Droplets Using Lattice Boltzmann Models. *Phys. Rev. E* **90**, 023305 (2014).

119. Desgouilles, S. *et al*. The Design of Nanoparticles Obtained by Solvent Evaporation: A Comprehensive Study. *Langmuir* **19**, 9504–9510 (2003).

120. Staff, R. H. *et al*. Particle formation in the emulsion-solvent evaporation process. *Small* **9**, 3514–3522 (2013).

121. Doshi, N. *et al*. Flow and adhesion of drug carriers in blood vessels depend on their shape : A study using model synthetic microvascular networks. *J. Control. Release* **146**, 196–200 (2010).

122. Larson, R. G. The Structure and Rheology of Complex Fluids. (*Oxford University Press*, 1999).

123. Boublík, T., Fried, V., & Hála, E. The vapor pressures of pure substances. (*Elsevier*, 1984).

124. Rossberg, M. *et al*. Chloromethanes. *Ullmann's Encyclopedia of Industrial Chemistry* (*John Wiley & Sons*, 2000).

125. Prager, J. C. *Environmental contaminant reference databook*. (*Van Nostrand Reinhold*, 1995).

126. Fini, A., Fazio, G., Fernaandez-Hervaas, M. J., Holgado, M. A. & Rabasco, A. M. Fractal Analysis of Sodium Cholate Particles. *J. Pharm. Sci.* **85**, 971–975 (1996).

127. Carulli, N. et al. Effect of bile salt pool composition on hepatic and biliary functions. *Aliment Pharmacol Ther* **14**, 14–18 (2000).

128. Klouwer, F. C., Berendse, K., Ferdinandusse, S., Wanders, R. J. & Engelen, M. Zellweger spectrum disorders : clinical overview and management approach. *Orphanet J. Rare Dis.* **10**, 151 (2015).

129.   Hirschfield, G. M. et al. The British Society of Gastroenterology / UK- PBC primary biliary cholangitis treatment and management guidelines. *Gut* **67**, 1568–1594 (2018).

130.   Mikov, M., Fawcett, J.P., Kuhajda, K. & Kevresan, S. Pharmacology of Bile Acids and their Derivatives: Absorption Promoters and Therapeutic Agents. *Eur. J. Drug Metab. Pharmacokinet.* **31**, 237–251 (2006).

131.   Lansford, C., Mehta, S. & Kern, F. The treatment of retained stones in the common bile duct with sodium cholate infusion. *Gut* **15,** 48–51 (1974).

132.   Quintero, P., Pizarro, M., Solís, N., Arab, J. P., Padilla, O., Riquelme, A. & Arrese, M. Bile acid supplementation improves established liver steatosis in obese mice independently of glucagon-like peptide-1 secretion. *J. Physiol. Biochem.* **70**, 667–674 (2014).

133.   Gabbi, C. et al. Effects of bile duct ligation and cholic acid treatment on fatty liver in two rat models of non-alcoholic fatty liver disease. *Dig. Liver Dis*. **44**, 1018–1026 (2012).

134.   Yagima Odo, M. E., Cuce, L. C., Odo, L. M. & Natrielli, A. Action of Sodium Deoxycholate on Subcutaneous Human Tissue: Local and Systemic Effects. *Dermatologic Surg.* **33**, 178–189 (2007).

135.   Moretz, D. New Drug Evaluation: Cholbam (cholic acid) capsule, oral. (2012).

136.   Sykes, J. M,. Allak, A. & Klink, B. Future Applications of Deoxycholic Acid in Body Contouring. *J. Drugs Dermatology* **16**, 43–46 (2017).

137.   Luque-Michel, E. *et al*. A simple approach to obtain hybrid Au-loaded polymeric nanoparticles with a tunable metal load. *Nanoscale* **8**, 6495–6506 (2016).

138.   Turkevich, J., Stevenson, P. C. & Hillier, J. A Study of the Nucleation and Growth Process in the Synthesis of Colloidal Gold. *Trans. Faraday Soc*. **11**, 55–75 (1951).

139.   Macierzanka, A. et al. Adsorption of bile salts to particles allows penetration of intestinal mucus. *Soft Matter* **7**, 8077–8084 (2011).

140.   Fromen, C. A., Dunn, S. S. & Desimone, J. M. Biomedical Nanopreprations with Controlled Geometry. *Handbook of Nanobiomedical Research.* 349-400 (2014).

141.   Decuzzi, P. et al. Size and shape effects in the biodistribution of intravasculary injected particles. *J. Control. Release* **141**, 320–327 (2010).

142.   Klose, D., Siepmann, F., Elkharraz, K., Krenzlin, S. & Siepmann, J. How porosity and size affect the drug release mechanisms from PLGA-based microparticles. *International Journal of Pharmaceutics* **314**, 198–206 (2006).

143.   Jeong, S. W., Wood, A. L. & Lee, T. R. Effects of pure and dyed PCE on physical and interfacial properties of remedial solutions ⅌. *J. Hazard. Mater*. **95**, 125–135 (2002).

144.   von Burrkersroda, F., Schedl, L. & Gopferich, A. Why degradable polymers undergo surface erosion or bulk erosion. *Biomaterials* **23**, 4221–4231 (2002).

145.   Dawson, P. A. & Karpen, S. J. Intestinal transport and metabolism of bile acids. *J. Lipid Res*. **56**, 1085–1099 (2015).

146.   Rotunda, A. M. Injectable Treatments for Adipose Tissue : Terminology , Mechanism , and Tissue Interaction. *Off. J. Am. Soc. Laser Med. Surg*. **41**, 714–720 (2009).

147.   Nasrollahi, P. *et al*. Sustained release of sodium deoxycholate from PLGA – PEG – PLGA thermosensitive polymer. *Artif. Cells, Nanomedicine, Biotechnol*. **46**, S1170–S1177 (2018).

148.	Chandirasekar, S., Dharanivasan, G., Kasthuri, J., Kathiravan, K. & Rajendiran, N. Facile Synthesis of Bile Salt Encapsulated Gold Nanoparticles and Its Use in Colorimetric Detection of DNA. *J. Phys. Chem.* **115**, 15266–15273 (2011).

149.	Qiao, Y., Wang, Y., Yang, Z., Lin, Y. & Huang, J. Self-Templating of Metal-Driven Supramolecular Self-Assembly: A General Approach toward 1D Inorganic Nanotubes. *Chem. Mater.* **23**, 1182–1187 (2011).

150.	Panyam, J. & Labhasetwar, V. Biodegradable nanoparticles for drug and gene delivery to cells and tissue. *Adv. Drug Deliv. Rev.* **55**, 329–347 (2003).

151.	Schlottmann, K., Wachs, F., Krieg, C., Kullmann, F. & Rogler, G. Characterization of Bile Salt-induced Apoptosis in Colon Cancer Cell Lines. *Cancer Res.* **60**, 4270–4276 (2000).

152.	Ignacio, J. et al. Deoxycholic and chenodeoxycholic bile acids induce apoptosis via oxidative stress in human colon adenocarcinoma cells. Apoptosis 16, 1054–1067 (2011).

153.	Barrasa, J. I., Olmo, N., Lizarbe, M. A. & Turnay, J. Toxicology in Vitro Bile acids in the colon , from healthy to cytotoxic molecules. *Toxicol. Vitr.* **16**, 1054 (2011).

154.	Milovic, V., Teller, I. C., Faust, D., Caspary, W. F. & Stein, J. Effects of deoxycholate on human colon cancer cells: apoptosis or proliferation. *Eur. J. Clin. Invest.* **32**, 29–34 (2002).

155.	Thuangtong, R., Bentow, J. J., Knopp, K., Mahmood, N. A., David, N. E. & Kolodney, M. S. Tissue-Selective Effects of Injected Deoxycholate. *Dermatologic Surg.* **36**, 899–908 (2010).

156.	Carter, P. J. Potent antibody therapeutics by design. *Nat. Rev. Immunol.* **6**, 343 (2006).

157.	Berger, M., Shankar, V. & Vafai, A. Therapeutic Applications of Monoclonal Antibodies. *Am. J. Med. Sci.* **324**, 14–30 (2002).

158.	Folkes, A. S. *et al.* Targeting CD47 as a cancer therapeutic strategy- the cutaneous T ell lymphoma experience. *Curr Opin Oncol* **30**, 332–337 (2018).

159.	Ryan, J. J. CD47-Blocking Antibodies and Atherosclerosis. *JACC. Basic to Transl. Sci.* **1**, 413–415 (2016).

160.	Soto-pantoja, D. R. *et al.* Therapeutic opportunities for targeting the ubiquitous cell surface receptor CD47 Therapeutic opportunities for targeting the ubiquitous cell surface receptor CD47. *Expert Opin. Ther. Targets* **17**, 89-103 (2013).

161.	Majeti, R. *et al.* CD47 Is an Adverse Prognostic Factor and Therapeutic Antibody Target on Human Acute Myeloid Leukemia Stem Cells. *Cell* **138**, 286–299 (2009).

162.	Wu, C., Hsieh, C., Huang, S., Lin, J. & Wang, T. In vivo Imaging Flow Cytometry of Human Leukocytes. *Opt. Life Sci.* BoW3A-2 (2017).

163.	Makadia, H. K. & Siegel, S. J. Poly Lactic-co-Glycolic Acid (PLGA) as Biodegradable Controlled Drug Delivery Carrier. *Polymers* **3**, 1377-1397 (2011).

164.	Jain, R. A. The manufacturing techniques of various drug loaded biodegradable poly(lactide- co-glycolide) (PLGA) devices. *Biomaterials* **21**, 2475-2490 (2000).

165.	Iqbal, M., Zafar, N., Fessi, H. & Elaissari, A. Double emulsion solvent evaporation techniques used for drug encapsulation. *International Journal of Pharmaceutics* **496**, 173-190 (2015).

166.	Aragon, J. *et al.* The effect of variable release kinetics on Paclitaxel efficacy from a drug eluting stent in a porcine model. *Interv. Cardiol. Eur. Soc. Cardiol.* **1**, 228–235 (2005).

167.	Al-maaieh, A. & Flanagan, D. R. Salt and cosolvent effects on ionic drug loading into microspheres using an O / W method. *J. Control. Release* **70**, 169–181 (2001).

168.	Ali, M., Walboomers, X. F., Jansen, J. A. & Yang, F. Influence of formulation parameters on encapsulation of doxycycline in PLGA microspheres prepared by double emulsion technique for the treatment of periodontitis. *J. Drug Deliv. Sci. Technol*. **52**, 263–271 (2019).

169.	Shenderove, A., Burke, T. G. & Schwendeman, S. P. Stabilization of 10-Hydroxycamptothecin in Poly(lactide-co-glycolide) Microsphere Delivery Vehicles. *Pharm. Res.* **14**, 1406-1414 (1997).

170.	Lai, M. & Tsiang, R. C. Microencapsulation of acetaminophen into poly(L-lactide) by three different emulsion solvent- evaporation methods. *J. Microencapsul.* **22**, 261-274, (2005).